University of Naples Federico II

Department of Chemical, Materials and Production Engineering

PhD Thesis in

Industrial Products and Process Engineering

XXXVI cycle

Clinical-data driven design of nanoparticles

Enza Cece

Supervisor:

Prof. Enza Torino

Coordinator:

Prof. Andrea D'Anna

2020-2023

Table of contents

Abstract

Personalized medicine aims to identify treatments tailored for individual patients or groups of patients based on their unique features, including factors such as genetics, environmental influences, disease biomarkers and phenotype. This approach stands in contrast to the traditional "one-size" fits all strategy, which does not take in consideration the heterogeneity of the disease among different patients and does not consider the pathophysiological degree of the targeted disease. This leads to a poor clinical outcome, thus pushing personalized medicine into the clinical practice. In this regard, omics-based medicine (in terms of genomics, transcriptomics, proteomics, metabolomics, radiomics), next-generation sequencing, conventional tests (tests on body fluids, immunohistochemistry, flow cytometry, histopathology, and biopsy) and clinical imaging (Magnetic Resonance Imaging, Computed Tomography, Positron Emission Tomography, Ultrasound Imaging) are used to provide data about the pathophysiological state of the patient. Attempts in collecting and categorizing these data can be found in the creation of databases, like *Cancer Imaging Archive*, *Cancer Genome*, *Cancer Proteome Atlas* or *cBioPortal* for cancer genomics.

In this scenario, Drug Delivery Systems (DDSs) and nanomedicine are establishing as a tool to contribute to the acceleration and translation of personalized medicine. DDSs can, actually, be designed and engineered with diverse physico-chemical properties, enabling precise diagnosis, targeted therapy at the tissue, cellular or molecular level and facilitating the monitoring of the treatment.

The optimal design of a DDS relies upon a comprehensive analysis that considers the intended application (*i.e.*, imaging, therapeutic, theranostics), addresses the targeted pathology and considers the active agents to be encapsulated. Furthermore, it considers factors such as biodegradability, biocompatibility, on- and off-target release kinetics and scalability production of the same. This approach enables the selection of materials and production processes best suited and tailored for the requirements of the DDS of interest. Even though a huge plethora of DDSs architecture is nowadays available, rational guiding principles to engineer their design features, through a disease and patient informed approach, are still missing.

Thus, the adjustment of the physicochemical properties of the DDS, generally, relies on the evaluation of their *in vitro* and/or *in vivo* response for a specific clinical task of interest. This is a trial-and-error approach that results to be time consuming and, since it does not consider the whole framework shaped by the biological barriers encountered by injected DDSs, it drastically hinders their clinical translation. In average, a survey analysis of literature[1] has found that less than 1% of the injected dose is capable of reaching the target site of interest. Indeed, biological barriers, encountered by DDSs intravenously injected, span across multiple scales and move from blood circulation to blood vessels' margination and extravasation, diffusion in the Extracellular Matrix and uptake by the targeted cells. Each one of these barriers poses obstacles to the delivery and biodistribution of DDSs at the target site. Transport conditions faced by DDSs are posed by the biological barriers and are extremely different depending on the degree of the disease and on the patient.

Therefore, there is the necessity to transition towards the personalized design of the DDS and establish models and principles for an *a-priori* determination of the physico-chemical properties, best suited for the pathological condition of interest.

As examples, Karageorgis et al.[2] found that the accumulation of lipidic nanocapsules depends on the structural and permeability parameters of tumor microvasculature. Similarly, Sykes et al.[3] histologically characterized tumors of different sizes in mice (ranging from low to high tumor volume due to disease progression), considering factors such as increased vascular density, cell density, and extracellular matrix content. They correlated these parameters with the tumor's capacity to accumulate PEGylated gold nanoparticles of various sizes. These examples demonstrate that it is possible to predict *a-priori* the accumulation of a DDS based on tumor characteristics and, consequently, adjust the properties of the DDS accordingly. However, the reported examples are focused on one type of tumor and one type of DDS.

The paradigm shift of personalized nanomedicine needs to progress in two directions: a thorough characterization of the biological barriers and correspondent nano-bio interactions, as well as the development of tools through which a matching between the synthetic and biological identity of DDSs. This approach is expected to give the possibility to determine the optimal design of the DDS, so that it can achieve the desired *in vivo* behaviour and, consequently, the desired clinical outcome.

While the need to characterize biological barriers is evident, it becomes equally apparent that a standardized and uniform methodology for achieving this goal is lacking. Clinical parameters are being extracted through a wide range of techniques, resulting in non-uniformity. On the other hand, clinical imaging is emerging as a pivotal tool for tumor characterization. Nonetheless, the acquisition of high-quality, artifact-free clinical images remains a formidable challenge, especially when dealing with early cancer lesions. In such cases, image reconstruction remains a crucial and critical step.

To match the *synthetic* and *biological identity* of DDSs is necessary to have a rational workflow that systematically incorporates each clinical tumour parameter into the design of the DDS. To translate this approach in a clinical and practical context, gathering preliminary data about nanoparticles from *in vitro* studies and *in vivo* studies, *in vitro* ECM penetration studies, open-source datasets, literature studies is the first step to perform. In a manner similar to the collection of clinical data on tumors, information about nanoparticles has been systematically gathered and organized within various databases. As examples, *caNanoLab is a data sharing portal designed to facilitate information sharing across the international biomedical nanotechnology research community to expedite and validate the use of nanotechnology in biomedicine; nano (a Nature Portfolio Solution) retrieves detailed information on properties, applications, toxicity and preparation methods of thousands of nanomaterials and devices; PubVINAS is a friendly online nanomodeling tool based on big data curation of nano-biological activities and nanostructure annotations; Nanoparticle Information Library (NIL) helps occupational health professionals, industrial users, worker groups, and researchers organize and share information on nanomaterials, including their health and safety-associated properties; compendium for Biomaterial Transcriptomics (cBiT) collects transcriptional profiles of cells after biomaterial*

exposure (knee and dental implants) and, finally, Nanomaterial-Biological Interactions (NBI) knowledgebase gives information on the toxicity on zebrafish of nanomaterials.

These databases collectively serve to facilitate research, collaboration, and informed decision-making in the field of nanotechnology and nano-bio interactions. However, they are associated with some challenges that make it difficult to access the information stored within them. These datasets are characterized by a high volume of non-organized data and the complexity and heterogeneity of the data collection methods, making it difficult to compare the data among them.

What is currently lacking is the integration of data from clinical tumor characterization and nanomedicine, as well as the establishment of meaningful relationships between these datasets. In this context, Machine Learning (ML) and Artificial Intelligence (AI) are increasingly establishing as powerful tools to find hidden relationships in complex datasets characterized by big data. ML/AI tools have already found their application also in nanomedicine; in particular, they have been used to adjust the production process parameters to achieve desired physicochemical properties of the nanoparticles or of the microparticles. On the other hand, they have been used for the prediction of nanoparticles' cytotoxicity, the cell uptake efficiency, depending on the material, size, charge and concentration of the nanoparticles, the prediction of the composition of the protein corona and, consequently, the cellular recognition mediated by it. Moreover, ML/AI has been also used to define Quantitative Structure Activity Relationships (QSARs), revealing non-evident links between structural properties of nanoparticles and their biological activity in vitro. As example, Mirkin et al. [4] correlated through a XGBoost Model (a ML algorithm) the *in vitro* immune response of macrophages with the structural properties of spherical nucleic acids (SNAs), by analysing a library of 1000 SNAs derived from the combination of 11 different design parameters. They selected the design parameters able to impact the most on the levels of immune activity. However, each ML/AI model has been implemented using single experimental datasets, analyzing individual DDS architectures and specific tumor scenarios, which limits its ability to capture the complexity of all the different architectures available and tumor types under treatment.

As there is a need to fine-tune the properties of DDSs to achieve a specific synthetic identity matching with the desired biological identity, microfluidics stands out as a reliable tool for production. It offers precise control over the final architecture and functionality of DDSs at the molecular level, resulting in narrow size distributions and very low batch-to-batch variability.

Aim of the work

Clinical translation of nanoparticles faces significant challenges due to the low percentage, often less than 1% of the injected dose, that effectively reaches the tumor target site[1]. Throughout their journey to the target site, nanoparticles encounter various barriers that hinder their delivery. The design of the DDSs, including their material composition, size, shape, stiffness, surface charge and surface decoration, which in this context is referred as *synthetic identity*, plays a crucial role in determining how they interact with and overcome these barriers. On the other hand, it's important to consider that the pathophysiological condition of the disease and the specific characteristics of the patient can alter the anatomical, mechanical, and fluido-dynamic properties of these barriers. Consequently, these changes can modify how nanomaterials interact with these barriers, leading to a diverse *biological identity* of the nanoparticles within the *in vivo* tumor microenvironment and resulting in different *nano-bio interactions*. The objective of my PhD thesis is to advance the field of personalized nanomedicine, by introducing and validating innovative tools and methodologies, aimed at providing rational guiding principles for engineering nanoparticles, utilizing a patient and disease informed approach to address specific pathologies. This includes the exploration and validation of microfluidic techniques for fine-tuning of the synthetic identity of nanoparticles. Additionally, it involves the development of algorithms for clinical image reconstruction, a critical step for extracting relevant clinical parameters, and the evaluation of tools for the generation of *in vitro* and *in vivo* data, alongside literature-based synthetic data, aimed at matching the synthetic and biological identity of nanoparticles. Furthermore, this thesis aims to pioneer machine learning and artificial intelligence as transformative tools for the *a-priori* selection of the most suitable properties of the nano-vector, tailored on the tumor under consideration.

Chapter 1 contributes to the thesis's aim by providing a thorough characterization of techniques for assessing biological barriers, nano-bio interactions, and the extraction of clinical parameters. This aims to highlight the clinical differentiation between various tumor types and emphasizes the necessity to guide nanoparticle design based on the clinical and pathological parameters of the patient and the disease.

Chapter 2 further contributes to the thesis's aim by validating microfluidics as a tool for fine-tuning the features of microparticles and nanoparticles. This is essential when personalizing the design of drug delivery systems (DDSs) based on the specific requirements driven by the disease and the patient.

In Chapter 3, insights into the challenges posed by image reconstruction are provided. This step is fundamental for the clinical characterization of tumors, and the chapter contributes to the thesis by presenting algorithms that improve the capture of early lung cancer lesions for personalized treatments.

Chapter 4 advances the thesis's objective by providing new tools for in vitro characterization of the diffusion of a library of nanoparticles in ECM-mimicking hydrogels. This offers the possibility to understand how different physico-chemical properties of DDSs can contribute to their biodistribution within the tumor ECM, depending on the stage of the pathology characterized by different degrees of ECM stiffness and porosity.

Finally, Chapter 5 supports the thesis's aim by showcasing the potential of ML/AI in finding relationships in nanoparticles' related datasets. However, the lack of available data for defining connections between the design

features of nanoparticles and clinical tumor parameters has led to the generation of synthetic data, highlighting the need for standardization and categorization of data from literature studies and available databases, both for tumor and nanoparticle characterization.

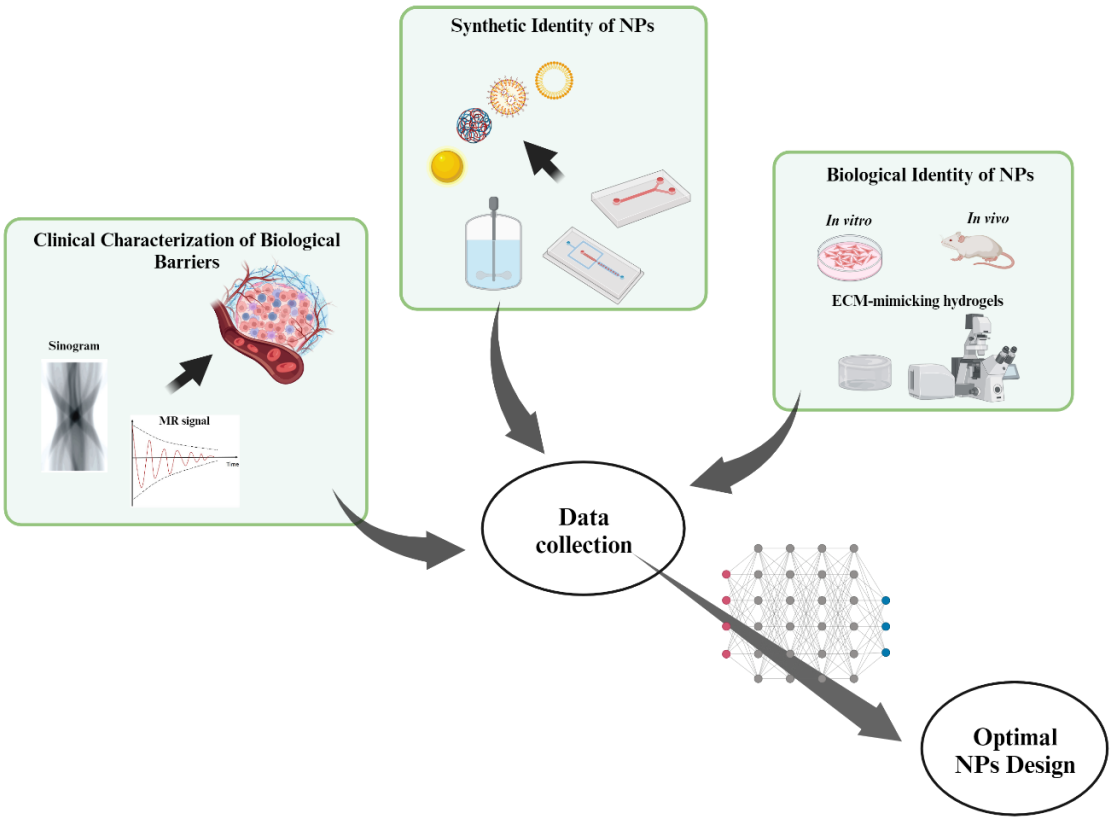

Chapter 1 – *Personalized nanomedicine: the impact of optimal and patient – driven design of nanoparticles on the delivery to targeted tumour tissue*

1. Background

1.1 Overview of the barriers and transport phenomena involved in nanoparticles' delivery to targeted tumour tissue

Barriers to drug delivery and, more specifically, to the delivery of DDSs and NPs span across multiples scales, impairing their efficient biodistribution. Once inside the blood, depending on their size, first of all, nanoparticles can be cleared by the kidneys, when they have a diameter lower than 10 nm, or activate the complement system, when NPs are larger than 200 nm. Moreover, when blood proteins absorb on their surface, forming the so-called *protein corona*, the recognition and immediate removal from the blood by the mononuclear phagocytic system may be triggered [5-7]. The collision frequency between nanoparticles and blood proteins can be approximated in the order of $10^6 s^{-1}$.[7] Thus, nanoparticles in the blood stream experience millions of collision within the first microseconds from their entry and each of this collision is a possibility for blood proteins to form a protein corona. This happens, particularly, when blood proteins have a certain affinity for the surface of nanoparticles[7].

Subsequently, nanoparticles need to undergo lateral drift, *i.e.* margination, towards the vessel walls and interact with endothelial cells in order to be able to extravasate inside the tumor tissue, through the fenestrations of the vessels, which can be compromised in presence of a tumor. For nanoparticles in the range $1 - 100\, nm$, margination mainly relies on diffusion; on the other hand, for particles approaching to the micrometer dimension, convection plays an important role in the lateral drift and larger nanoparticles will have greater margination than the smaller ones.[7] Extravasation of nanoparticles across the vessel walls can be described by the *Staverman–Kedem–Katchalsky approximation*:

$$J = PA(C_v - C_i) + L_p A(1-\sigma)\{(p_v - p_i) - \sigma(\pi_v - \pi_i)\}C_v \quad \text{(Eq. 1)}$$

with:

$$P = \frac{\gamma H}{L}\mathcal{D}_0. \quad \text{(Eq. 2)}$$

In Eq.1, P and A represent the permeability and surface area of the vessel wall, L_p is its hydraulic conductivity, σ is the osmotic reflection coefficient, $(p_v - p_i)$, $(\pi_v - \pi_i)$ and $(C_v - C_i)$ are the hydrostatic pressure, osmotic pressure and concentration differences across the vessel wall respectively. Permeability is approximated as in Eq.2; here, γ represents the surface area of the vessels occupied by pores, L is the thickness of the vessel wall,

H is a hindrance factor depending on the ratio between nanoparticle size and pore size, $\mathcal{D}_0$ is the diffusivity of the particle in a free solution. The second term on the right side of *Eq. 1* represents the convective contribute to the flux J of nanoparticles.

Once inside the tumor microenvironment, however, nanoparticles face changes in mechanical and fluido-dynamic properties of the targeted tissue, which extremely influence transport phenomena. In solid tumors, actually, vasculature is abnormal, disordered, and characterized by the presence of leakier and more permeable blood vessels and the absence of a functional lymphatic drainage system (i.e. Enhanced Permeability and Retention Effect, EPR). As a result, excessive loss from the vascular system to the interstitial one occurs and an elevated interstitial fluid pressure (IFP) arises within the tumor. IFP equals the microvascular one, making diffusion the main mechanism of transvascular and interstitial mass transport. At the tumor periphery, IFP drops causing a steep pressure gradient that may determine an intravasation of materials back into systemic circulation. Convection flow is, thus, drastically reduced and, furthermore, diffusion has to occur in a tortuous, much denser and stiffer extracellular matrix (ECM). Consequently, the diffusion transport which, by itself, is already much slower than convection is drastically impaired[8-10].

Nanoparticles diffusion coefficient within ECM can be approximated as:[7]

$$\mathcal{D} = \frac{k_B T}{6\pi\eta R_{NP}}(1-\varphi)^2 exp\left\{-\sqrt{\varepsilon_{int}} \times \frac{R_{NP}}{R_f}\right\}. \quad \text{(Eq. 3)}$$

In Eq. 3, η is the viscosity of the interstitial fluid, φ is the cell density, ε_{int} is the volume fraction of the ECM fibers, R_f is the fiber radius and R_{NP} is the nanoparticle radius.

As it is possible to observe, *Eq. 3* is constituted by three factors: the first one is the Stokes-Einstein diffusivity of particles in free medium, the second one adjusts the diffusion coefficient to reflect the hindrance posed by the cells and the third one to consider the steric hindrance between nanoparticles and the porosity and radius of ECM fibers.

The final barrier encountered by nanoparticles is represented by their interaction with tumor cells; nanoparticles are typically internalized by endocytosis. Endocytosis relies on an energetic process that consists in the adhesion and wrapping of the membrane around the nanoparticles, thus overcoming the membrane bending energy[7].

In *Figure 1*, the sequential biological barriers described earlier are schematically illustrated, with a focus on the primary clinical parameters that can be derived from each of these barriers and the nano-bio interactions that take place at each stage.

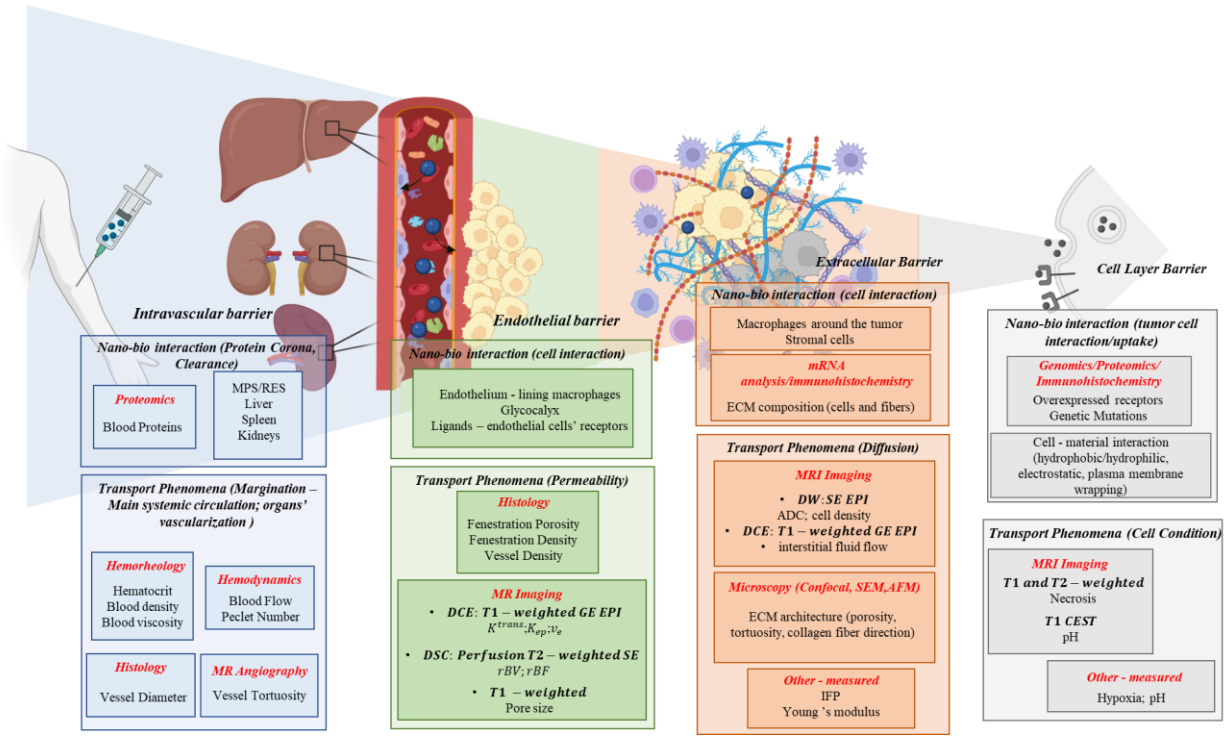

Figure 1 *– characterization of biological barriers and nano-bio interactions*

Clinical imaging, as it is possible to observe in *Figure 1*, is emerging as a disruptive and powerful tool for assessing relevant tumor characteristics, enabling the capture, through a non-invasive approach, of structural, anatomical, physiological, molecular, and biological features of a tumor [11]. Various imaging techniques can serve this purpose, including dynamic contrast-enhanced MRI (DCE-MRI), dynamic contrast-enhanced ultrasound (DCE-US), dynamic susceptibility contrast-enhanced MRI (DSC-MRI), perfusion CT (PCT), diffusion-weighted imaging (DWI), magnetic resonance spectroscopy (MRS) and spectroscopic imaging (MRSI), arterial spin-labelling (ASL), blood oxygenation level-dependent MR imaging (BOLD-MRI), elastography, positron emission tomography (PET), or single-photon emission computed tomography (SPECT) imaging.

2. Short Aim of the chapter

In this chapter, our first aim is to provide a clinical and quantitative characterization of the biological barriers discussed earlier. We will focus on two tumor case studies (*i.e.*, brain and breast tumors), to enlighten the different transport phenomena conditions and, consequently, nano-bio interactions in relation to the pathophysiological state of the tumor and of the patient.

Secondly, we propose a block connection between the patient-derived tumor information and nanoparticle design properties. This will emphasize the mutual influence between these parameters and offer a rational workflow for adjusting the nanoparticles' features based on their *in vitro* and *in vivo* biological behaviour.

3. Results

3.1 The case study of brain and breast tumours: clinical characterization and differentiation between the tumours

Based on the schematization of the biological barriers reported in *Figure1*, a collection of clinical parameters available in literature was performed for two case studies of brain and breast tumors, with the aim to understand the clinical differentiation between different types of cancers. In *Table 1*, it is possible to observe the value of Vessel Diameter (VD), depending on the grading of brain tumor, varying between grade II, grade III and grade IV glioma, and breast tumor, varying between Invasive Ductal Carcinoma (IDC), Ductal Carcinoma in Situ (DCIS) and Invasive Lobular Carcinoma (ILC).

Tumor	*Grade*	*Parameter*	*Value*	*Standard Deviation*	*Unit of Measure*	*Technique*
Brain	Low Grade Glioma (grade II)	VD	5,1	1,08	µm	Histology
Brain	grade III	VD	7,93	1,34	µm	Histology
Brain	grade IV	VD	9,83	1,43	µm	Histology
Tumor	*Grade*	*Parameter*	*Value*	*Standard Deviation*	*Unit of Measure*	*Technique*
Breast	IDC	VD	0,044	0,018	cm	Doppler Ultrasonography
Breast	DCIS	VD	0,038	0,017	cm	Doppler Ultrasonography
Breast	ILC	VD	0,043	0,008	cm	Doppler Ultrasonography

Table 1 *- intravascular barrier parameters: brain and breast tumors*[12, 13]

From *Table 1*, it becomes evident that VD increases with the higher grading of brain tumors. In contrast, there is no such variation observed for breast cancer. Moreover, the VD diameter is smaller in brain with respect to breast cancer, highlighting possibly a potentially lower margination capacity of the same DDS in a brain or breast tumor case scenario.

In *Table 2* and *Table 3*, parameters related to the varying degrees of tumor ECM components' expression are presented for brain and breast tumors, respectively.

# of cases	Tumor	Basement membrane of blood vessels				Technique
		Type I collagen	Type IV collagen	Fibronectin	Laminin	
4	Normal Brain Tissue	N	N	Y	Y	Immunohistochemistry
8	Anaplastic Astrocytoma	N	N	Y	Y	
4	Low-grade glioma	N	Y (low)	Y	Y	
13	Glioblastoma	N	Y	Y	Y	

# of cases	Tumor	ECM Tumor cells				Technique
		Type I collagen	Type IV collagen	Fibronectin	Laminin	
4	Normal Brain Tissue	N	N	N	N	Immunohistochemistry
8	Anaplastic Astrocytoma	N	N	Y	N	
4	Low-grade glioma	N	Y	Y (low)	N	
13	Glioblastoma	N	Y	Y	Y	

Molecule	Tumor Grade				Technique
	Normal Brain Tissue	Astrocytoma grade I	Astrocytoma grade II	Astrocytoma grade III	Glioblastoma	
Integrin α3, integrin β3	↑	↑	↑	/	/	mRNA analysis (QRT-PCR)
Fibronectin	/	↑	↑	↑	↑	
Laminin α4	↑	↑	↑	↑	↑	
Tenascin R	↑	↑	↑	↑	↑	
Tenascin C	↑	↑	↑	↑	↑	
Syndecan	/	/	↑	↑	/	
Brevican, Neurocan, Versican	↑	↑	↑	↑	↑	
Cadherin 12	↑	↑	↑	↑	↑	
CD168	↑	↑	↑	↑	↑	
# for mRNA analysis ; # for protein analysis	18 ; 36	14 ; 12	14 ; 12	14 ; -	16 ; 12	

Table 2 *– extracellular barrier parameters: brain tumours*[14-16]

As evident from *Table 2*, certain types of collagens, such as type IV collagen, are expressed by brain tumor cells, but not by normal brain tissue. Conversely, it can be shown that the expression of certain other ECM

components, such as tenascin C and tenascin R, increases with the rising pathological degree, while others, like fibronectin, decrease with the degree.

	Laminin α5			
Tumor Type	**Vascular**	**Epithelial Basement Membrane**	**Tumor Cells**	**Technique**
Normal	+++	+++	Not Applicabe	
Normal	+++	+++	Not Applicabe	
Normal	+++	++	Not Applicabe	
DCIS (grade II)	+++	++	+	
Infiltrating DC (grade II)	+++	+	+	
Infiltrating DC (grade II)	+	+	+ -	
Infiltrating DC (grade II)	+++	++	++	
Infiltrating DC (grade II)	+++	++	+	
Infiltrating DC (grade II)	+++	++	+ -	
Infiltrating DC (grade II)	++	+	++	Immunohistochemistry
Infiltrating LC (grade II)	+++	++	++	
Infiltrating LC (grade II)	+++	+ -	+	
Mixed infiltrating LC/DC (grade II)	+++	+	+	
Infiltrating DC (grade III)	+++	++	+++	
Infiltrating DC (grade III)	+++	++	+ -	
Infiltrating DC (grade III)	++	+	+++	
Infiltrating DC (grade III)	+++	+	+++	
Infiltrating DC (grade III)	+++	+	+++	
Mixed infiltrating LC/DC (grade III)	+++	++	++	

Tumor Type	**# of cases**	**Leptin % positive**	**Adiponectin % positive**	**Technique**
DCIS Comedo	16	94,1	29	
DCIS Cribiform	4	100	75	
DCIS Papillary	11	100	11,1	Immunohistochemistry
DCIS Solid	10	100	44,4	
Invasive Ductal Carcinoma	154	34	53,4	
Invasive Lobular Carcinoma	1	0	100	

Table 3 *- extracellular matrix barrier parameters: breast tumors*[17, 18]

Similar consideration can be made from *Table 3*, related to breast cancers.

Table 4 and *Table 5*, similarly, collect rates of expression of different tumor cell receptors, showing the possibility of diverse targeting strategies depending on the tumor that is under consideration.

Tables 2, 3, 4, and 5 illustrate the potential to adjust the targeting strategy employed for DDSs. This adjustment aims to strike a balance between on-target and off-target release, either by favouring targeting elements predominantly expressed by tumors as opposed to normal cells or by tailoring the approach to different disease degree levels.

Grade	# of samples	Parameter	negative %	positive % (+)	positive % (++)	positive % (+++)	Technique
glioblastoma (grade IV)	52	Epidermal Growth Factor Receptor (EGFR)	28,8	34,6	26,9	9,7	
anaplastic astrocytoma (grade III)	47	Epidermal Growth Factor Receptor (EGFR)	27,7	12,8	38,3	21,3	Immunohistochemistr
oligodendroglioma and astrocytoma	15	Epidermal Growth Factor Receptor (EGFR)	86,7	13,3	0	0	y
astrocytic low grade glioma	9	Epidermal Growth Factor Receptor (EGFR)	66,7	33,3	0	0	

Grade	# of cases	Parameter	VEGF Positive overexpression %	Vascular volume (% total tumor volume)	Technique
glioblastoma (grade IV)	15	VEGF	86,70%	23,9	
anaplastic astrocytoma (grade III)	10	VEGF	40%	7,6	
astrocytoma (grade II)	6	VEGF	16,70%	6,2	Immunohistochemist
pilocytic astrocytoma (grade I)	5	VEGF	0%	14,3	ry
oligodendroglioma (grade II)	5	VEGF	80%	6,9	

Grade	# of cases	Parameter	positive%	Technique
glioblastoma (grade IV)	23	LRP mma	87,50%	
anaplastic astrocytoma (grade III)	13	LRP mma	61,50%	Real-time PCR
low-grade astrocytoma	9	LRP mma	44,40%	
normal brain	13	LRP mma	23,20%	

Grade	Parameter	#	-	+	++	+++	Technique
HGG	TLR2	32	8	13	8	3	Immunohistochemistr
LGG	TLR2	42	3	12	7	20	y

Grade	Parameter	# of cases	positive%	Technique
grade II	Leptin	32	30	
glioma grade III	Leptin	17	60	
glioma grade IV	Leptin	15	80	Immunohistochemistry
grade II	ObR receptor	32	45	
glioma grade III	ObR receptor	17	70	
glioma grade IV	ObR receptor	15	75	

Grade	Parameter	#	% -	%+	%++	% +++	Technique
Control	p75NTR (BDNF receptor)	13	/	100	0	0	Immunohistochemistr
low-grade glioma	p75NTR (BDNF receptor)	32	/	94,4	5,56	0	y
high-grade glioma	p75NTR (BDNF receptor)	20	/	28,57	42,86	28,57	

Grade	Parameter	#	% positive	Technique
low-grade glioma	Estrogen Receptor	20	4	Immunohistochemistry
high-grade glioma	Estrogen Receptor	20	0	

Grade	Parameter	#	% positive	Technique
diffuse astrocytoma	somatostatin receptor (sst1)	8	0	
anaplastic astrocytoma	somatostatin receptor (sst1)	10	20	
glioblastoma	somatostatin receptor (sst1)	32	66	
diffuse astrocytoma	somatostatin receptor (sst2A)	8	0	
anaplastic astrocytoma	somatostatin receptor (sst2A)	10	10	
glioblastoma	somatostatin receptor (sst2A)	32	44	
diffuse astrocytoma	somatostatin receptor (sst3)	8	38	
anaplastic astrocytoma	somatostatin receptor (sst3)	10	40	Immunohistochemistry
glioblastoma	somatostatin receptor (sst3)	32	84	
diffuse astrocytoma	somatostatin receptor (sst4)	8	88	
anaplastic astrocytoma	somatostatin receptor (sst4)	10	80	
glioblastoma	somatostatin receptor (sst4)	32	72	
diffuse astrocytoma	somatostatin receptor (sst5)	8	25	
anaplastic astrocytoma	somatostatin receptor (sst5)	10	30	
glioblastoma	somatostatin receptor (sst5)	32	25	

Table 4 *- cell layer barrier parameters: brain tumours*

Breast Cancer Type	Parameter	TOT Number	% Positive Overexpression TOT	Technique
Normal Breast	Rate of overexpression of HER2	>700	0%	Immunohistochemistry
hyperplastic (PDWA)	Rate of overexpression of HER2	30	0%	
dysplastic (ADH)	Rate of overexpression of HER2	15	0%	
DCIS	Rate of overexpression of HER2	59	56%	
IDC + DCIS	Rate of overexpression of HER2	237	22%	
IDC	Rate of overexpression of HER2	412	11%	

Tumor Type	# of cases	Leptin Receptor % positive	Adiponectin Receptor % positive	Technique
DCIS Comedo	16	70,6	31,3	Immunohistochemistry
DCIS Cribiform	4	100	33,3	
DCIS Papillary	11	55,6	0	
DCIS Solid	10	88,9	40	
Invasive Ductal Carcinoma	154	29,1	61,1	

Tumor Type	# of cases	Transferrin Receptor % positive	Median intensity	Technique
Atypical Ductal Hyperplasia	9	5	1	Immunohistochemistry
DCIS	22	85	2	
Atypical Lobular Hyperplasia	21	0	0	
Lobular Carcinoma in Situ	13	90	2	
TOTAL carcinomas in situ	65	50	1	
IDC	17	50	2	
ILC	13	80	2	
Medullary carcinoma	8	100	3	
TOTAL invasive carcinomas	38	80	2	

Tumor Type	# of cases	CD151 receptor low	CD151 high	Technique
Invasive Breast Carcinoma (grade I or II)	51	42 (82%)	9 (18%)	Immunohistochemistry
Invasive Breast Carcinoma (grade III)	73	44 (60%)	29 (40%)	

Table 5 *- cell layer barrier parameters: breast tumours*

As a final note, clinical parameters related to perfusion across vessel walls are reported for both brain and breast tumors and are presented in *Table 6*. These parameters include $ktrans$ (representing the volume transfer constant per unit time for the contrast medium transfer from the vessel into the extracellular extravascular space, reflecting intratumoral microvascular permeability), Ve (indicating the volume fraction of contrast medium that leaks into the extracellular extravascular space), $Microvessel\ Density$ (MVD, a standardized histopathological measure under specific microscopic conditions), $relative\ cerebral\ blood\ volume$ ($rcbv$), $relative\ breast\ blood\ volume$ ($rbbv$), and $relative\ breast\ blood\ flow$ ($rbbf$). The differentiation between transport conditions posed by the two tumor types, will probably determine different margination and extravasation in the tumor ECM.

Tumor	Grade	Parameter	Value	Standard Deviation	Unit of Measure	Technique
Brain	Low Grade Glioma (grade II)	MVD	14,75	4,94	/	
Brain	grade III	MVD	26,84	9,17	/	Histology
Brain	grade IV	MVD	22,79	3,51	/	
Brain	Low Grade Glioma (grade II)	Ktrans	0,026	0,019	min-1	
Brain	grade III	Ktrans	0,096	0,063	min-1	DCE
Brain	grade IV	Ktrans	0,135	0,068	min-1	
Brain	Low Grade Glioma (grade II)	Ve	0,121	0,13	per unit volume of tissue	
Brain	grade III	Ve	0,483	0,225	per unit volume of tissue	DCE
Brain	grade IV	Ve	0,525	0,18	per unit volume of tissue	
Brain	ependymoma (grade II)	corected rcbv	2,18	/	/	
Brain	Low-grade glioma (grade II)	corected rcbv	1,56	/	/	
Brain	Oligodendroglioma (grade II)	corected rcbv	0,72-1,46	/	/	
Brain	astrocytoma (grade II)	corected rcbv	0,44 - 3,35	/	/	
Brain	central neutrocytoma (grade II)	corected rcbv	2,33	/	/	PWI
Brain	mixed glioma (grade II)	corected rcbv	0,62	/	/	
Brain	anaplastic astrocytoma (grade III)	corected rcbv	0,74 - 5,63	/	/	
Brain	anaplastic oligedendroglioma (grade III)	corected rcbv	2,25-2,63	/	/	
Brain	glioblastoma (grade IV)	corected rcbv	1,65 - 11,03	/	/	
Breast	Benign Lesion	Ktrans	0,28	0,193	min-1	
Breast	Malignant Lesion	Ktrans	0,783	0,209	min-1	
Breast	Mammary Ductal Dysplasia	Ktrans	0,313	0,238	min-1	DCE
Breast	Ductal Carcinoma in Situ	Ktrans	0,713	0,169	min-1	
Breast	Invasive Ductal Carcinoma	Ktrans	0,803	0,224	min-1	
Breast	Benign Lesion	Kep	0,483	0,259	min-1	
Breast	Malignant Lesion	Kep	1,304	0,335	min-1	
Breast	Mammary Ductal Dysplasia	Kep	0,449	0,296	min-1	DCE
Breast	Ductal Carcinoma in Situ	Kep	1,282	0,375	min-1	
Breast	Invasive Ductal Carcinoma	Kep	1,338	0,326	min-1	
Breast	Benign Lesion	Ve	0,633	0,293	/	
Breast	Malignant Lesion	Ve	0,62	0,16	/	
Breast	Mammary Ductal Dysplasia	Ve	0,729	0,318	/	DCE
Breast	Ductal Carcinoma in Situ	Ve	0,601	0,172	/	
Breast	Invasive Ductal Carcinoma	Ve	0,617	0,159	/	
Breast	Benign	rbbv	2,5	0,76	/	
Breast	Malignant	rbbv	6,07	3,54	/	
Breast	grade I	rbbv	3,02	0,73	/	PWI
Breast	grade II	rbbv	4,73	0,99	/	
Breast	grade III	rbbv	9,47	3,91	/	
Breast	Benign	rbbvcorr	1,79	0,57	/	
Breast	Malignant	rbbvcorr	3,96	1,96	/	
Breast	grade I	rbbvcorr	2,02	0,59	/	PWI
Breast	grade II	rbbvcorr	3,43	0,8	/	
Breast	grade III	rbbvcorr	5,54	2,33	/	
Breast	Benign	rbbf	1,53	0,8	/	
Breast	Malignant	rbbf	3,61	2,52	/	
Breast	grade I	rbbf	1,51	0,37	/	PWI
Breast	grade II	rbbf	4,73	0,99	/	
Breast	grade III	rbbf	4,69	2,84	/	

Table 6 *- endothelial cell layer barrier: brain and breast tumours*

3.2 Schematic connection between patient – derived tumour information and nanoparticle design: a new proposed modelling to tune nanoparticle design based on clinical data

In this paragraph, we propose a workflow (*Figure 2*) for adjusting and personalizing the design of DDSs. The first step is to extract relevant clinical tumor parameters, including aspects of the pathophysiological tumor microenvironment, the tumor profiling, the histology and biopsy characterization, the structural properties of the tumor microenvironment and the tumor fluid-mechanical properties. We aim to explore how each of these clinical parameters can guide the design of nanoparticles and inform the selection of an appropriate production process. Once the optimal design of DDSs has been obtained, we seek for a proper characterization of the produced DDS to eventually adjust its production and we aim to understand its behaviour *in vitro* and *in vivo*, so that its properties are modified accordingly. The next step is the evaluation of the progression or regression of the disease, in order to be able to re-adapt the design of the DDSs based on the new pathological conditions.

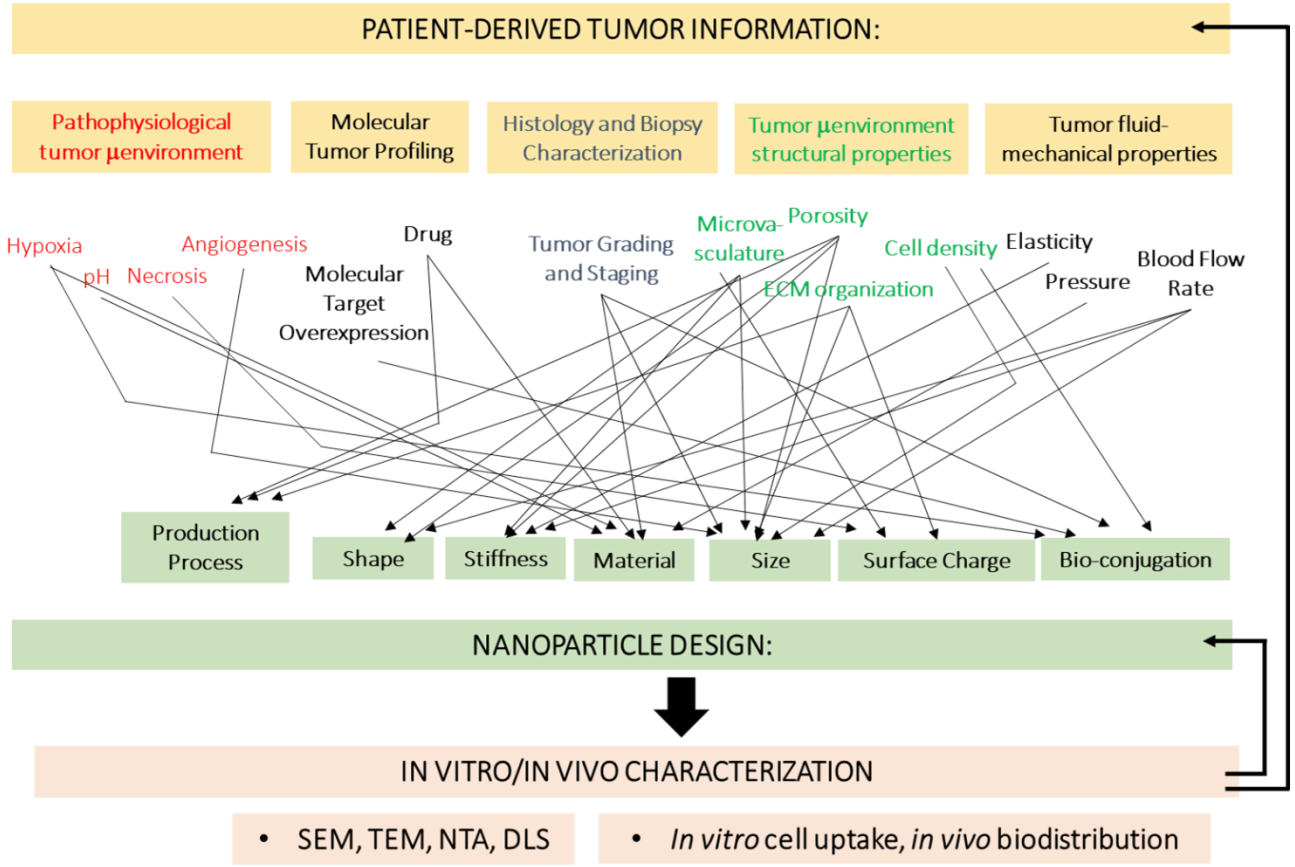

Figure 2 *- proposed schematic block-connection between patient-derived tumor information and nanoparticle design and workflow to adjust design parameters*

Chapter 2 - *the role and impact of microfluidics in the optimal design of nanoparticles for solid tumours: fine-tuning of nanoparticles properties as a tool to discover nano-bio interactions and accelerate personalized nanomedicine*

1. Overview of microfluidic reactors for nanoparticles production and droplet generation

This chapter includes parts from a paper under preparation: **Cece et al., "*Synthetic identity vs biological identity: the role of microfluidics in optimal design of nanoparticles for solid tumors"***

1.2 Microfluidic reactors and Nanoparticles Manufacturing

A pioneering application of microfluidics to the nanomedicine field goes back in 2004 with the work of *Jahn et al*., who triggered the spontaneous self-assembly of liposomes through two-dimensional flow focusing approach (2D HFF) in a cross-junction device. Here, a central inlet stream, containing phospholipids dissolved in isopropyl alcohol (IPA), was horizontally sheeted among two buffer streams, leading to an increase in IPA polarity and, consequently, to a decrease in phospholipids solubility; this triggered the micellization of phospholipids in liposome architectures[19]. Since then, this controlled increase in solvent polarity, due to microfluidic rapid mixing, has been exploited for the formation of different lipid-based nano-architectures, where the complexation among different lipids like cationic lipids, neutral lipids and cholesterol paved the way for the nucleic acid encapsulation [20, 21].

In this regard, *Kauffman et al.*, through microfluidics, developed a large library of lipid nanoparticles, each one with finely-tuned properties and evaluated how the lipid formulation impacts on the RNA delivery. Indeed, by increasing the ionizable lipid to mRNA ratio, the mRNA encapsulation efficiency increased due to a stronger complexation among the positively charged lipid and the negatively charged mRNA; however, if too strong, it could also hinder the de-complexation of the mRNA from the lipid structure once inside the cells, diminishing their *in vivo* efficiency [22].

To further delineate the lipid formulation impact on the final carrier properties, Kotoucek et al. and Weaver et al. took advantage of the fine-tunability offered by microfluidics to study the effect of saturated and unsaturated lipids on the nanoparticle distributions. They reported that saturated lipids, with lower content of cholesterol and consequently higher fluidity in the liposomal lipid bilayer, lead to lower sized nanoparticles with higher encapsulation efficiencies; on the other hand, unsaturated lipids, determined a higher dimension of nanoparticles with a reduced colloid stability [23, 24].

Besides the advantages offered by the lipid-based carriers, concerns are related to their stability in an *in vivo* environment [25]. So, to confer them stealth properties, *Ran et al.* incorporated PEG-lipids in the precursor lipid

mixture and observed a reduction in the lipid nanoparticles due to a stabilization of the intermediate lipid bilayer fragments or hydrophobic inverted micelles. Actually, with respect to un-PEGylated lipid nanoparticles, they showed a down-regulated phagocytosis when PEG-lipids were involved in the microfluidic process [26].

The acquired knowledge of lipid self-assembly in microfluidics, allowed to extend microfluidic processes to many diverse materials and thermodynamic of nanoparticle formation. In this perspective, *Karnik et al.* in 2008 synthesized PLGA-PEG nanoparticles (NPs) by means of self-assembly of the amphiphilic block-copolymers during nanoprecipitation, through a 2D HFF, in a cross-junction microfluidic reactor; acetonitrile-polymer stream was squeezed between two aqueous streams, so that mixing of acetonitrile and water occurs and determines the formation of polymeric micelles. *Karnik et al.*, for the first time, related the formation of polymeric micelles in microfluidic a three-stage process, i.e. nucleation, growth and aggregation, to the mixing time (τ_{mix}) of solvent and its effect on final dimension of the NPs [27].

Between the years 2009 and 2010, it has, then, been reported the role of fluid interface in the Y-junction microfluidic devices for the production, through nanoprecipitation, of poorly soluble drug nanoparticles. The authors obtained drug nanoparticles by injecting, in one channel of the device, the solvent drug solution and, in the other channel, the non-solvent solution for the drug; at the interface between solvent and non-solvent phases, the mixing occurs, eliciting the achievement of the drug supersaturation condition, followed by nucleation, growth and aggregation phases as previously described [28-30].

In 2012, *Capretto et al.* reported a nanoprecipitation process with increased complexity due the competition that arises between the above-mentioned nanoprecipitations. Indeed, in a 3 inlets Y-shaped device, they induced the co-precipitation of a block copolymer, Pluronic F127, and a highly hydrophobic model drug, $\beta - carotene$. They demonstrated the existence of competitive reactions, leading to the formation of two different architectures of nanoparticles, polymeric micelles that incorporate and stabilize nuclei of precipitated $\beta - carotene$ or empty ones. The final outcome depends on the characteristic mixing time of the system, highlighting the role of microfluidics in controlling the nanoparticle architecture [31].

Despite these first achievements, over years, passive mixing processes in T-junctions or Y-junctions and flow focusing/co-flow regimes in capillary-based microfluidics, have been scarcely exploited for nanoprecipitation of fully polymeric nanoparticles, with 2D HFF approach being the most used one. Indeed, a study from *de Solorzano et al.*, showed how the τ_{mix} decreased by moving from a Y-junction to a T-junction and, finally, to an X-junction and proving that, increasing τ_{mix}, determines an increase in nanoparticle size and polydispersity index [32].

The considerations emerging from the presented studies, reveal how microfluidics, both in terms of geometries and flow conditions, can be tuned to directly manage the thermodynamics of self-assembly and nanoprecipitation processes with a direct impact on the final nanoparticle architecture. In this context, an important role is played by the materials characteristics (such as hydrophilicity/hydrophobicity and MW).

Morikawa et al. and Roces et al. investigated, in this sense, the effect of different ratio of PLA:PGA on the size, encapsulation efficiency and active agent release profile from PLGA nanoparticles., Actually, it's

possible to increase the hydrophilicity or the hydrophobicity of the polymer, by increasing PGA or PLA content, respectively. The authors showed that higher hydrophilicity leads to lower nanoparticle dimension, while higher hydrophobicity determines a boosting in the encapsulation efficiency of active agents, since the more hydrophobic polymer, thanks to microfluidic rapid mixing conditions, is induced to rapidly aggregate and entrap more active agent molecules. However, in any case, the release profile showed a very significant initial burst, which is disadvantageous for *in vivo* applications [33, 34]. Furthermore, PLGA triggers recognition by Reticuloendothelial System (RES), significantly reducing nanoparticle *in vivo* circulation time. So, similarly to lipid-based nano-architectures, incorporation of PEG in the precursor polymer solution leads to the attribution of stealth properties to PLGA nanoparticles. *Morikawa et al* and *Abstiens et al*, actually, highlighted how PEG acts as a stabilizer of the nuclei formed during the microfluidic nanoprecipitation process, thus leading to lower nanoparticle dimension, higher encapsulation efficiencies of active agents and to a more sustained release profile [33, 35]. Moreover, nanoparticles with a relatively high PEG coverage have been shown to have the lowest uptake *in vitro* from macrophages and, consequently, the longest circulation time *in vivo* [36].

The fine control of τ_{mix}, flow interfaces, solvent extraction and consequently of the nanoprecipitation mechanism offered by 2D HFF in microfluidics, allowed to match it to more complex and delicate processes such as chemical reactions, in particular crosslinking of water-soluble polymers and ionotropic gelation. This allows to extend microfluidics towards the use of natural polymers, like hyaluronic acid, chitosan or alginate, which, with respect to synthetic polymers, show enormous advantages, providing chemical groups for the functionalization and conjugation of the nanoparticle surface, stealth properties and receptors overexpressed by cancer cells, in addition to biocompatibility and biodegradability [37, 38]. Indeed, the 2D HFF was used by *Russo et al.* to produce crosslinked Hyaluronic Acid Nanoparticles encapsulating Gd-DTPA, an MRI contrast agent widely used in clinical practice. They showed that, through the implemented microfluidic approach, it's firstly possible to match the nanoprecipitation of HA with the crosslinking reaction kinetics, achieving uniform particle population with tunable size, but most importantly to accurately tune the cross-linking degree of final nanoparticles. They found that in a specific range of crosslinking, it is possible to reach a complex equilibrium between the elastic stretches of polymer chains, water osmotic pressure and hydration degree of gadolinium, in this way boosting the relaxometric properties of the contrast agent through the Hydrodenticity effect [39]. Few years later, Smeraldo et al. presented a process of nanoparticle formation through ionotropic gelation and cross-linking of chitosan (CS) with tripolyphosphate polyanion (TPP), followed by complex coacervation between CS and HA. By fixing microfluidic process parameters (i.e. high and low flow rate regime), they showed how microfluidics allows to finely tune nanoparticle morphology that, based on different CS:HA ratio, moves from co-precipitate nanostructure to core-shell one. Finally, by preliminary encapsulation of Gd-DTPA in CS-HA nanoparticles, they observed similarly a hydrogel mediated boosting of Gd-DTPA relaxometric properties through Hydrodenticity [40].

A further possibility to process natural polymers was reported by *Dashtimoghadam et al.* in 2013, who exploited the microfluidic controllable self-assembly of hydrophobic modified chitosan to finely tune the

compactness of the polymeric structure. The authors showed how such a feature can be altered by the degree of hydrophobic modification and by the flow rate ratio; actually, microfluidic rapid mixing induces fast and strong intramolecular interactions among hydrophobic groups of the chemically modified chitosan, triggering the formation of a very compact and dense core [41].

Technical issues in microfluidic devices may, however, arise when the processed polymer or lipid solution interacts with the channel walls, causing clogging problems. In these situations, 3D HFF is helpful, since the processed material stream is sheeted both horizontally and vertically. This avoids interactions between the polymers or lipids and the walls of the microfluidic reactor; in particular PLGA and PLGA-PEG have been found to interact with hydrophobic channel walls, like the ones fabricated in PDMS; thus, impeding the exploration of wider ranges of polymer MW or concentration [42, 43]. *DeVoe et al.* also, showed that the 3D HFF allows to produce highly monodisperse liposomes with a production rate up to 4 times higher with respect to conventional 2D HFF approach, due to the complete radially symmetric mixing of the fluid inputs [44].

Despite the fine control offered, passive micromixers, like Y and cross-junctions, rely on the diffusion phenomenon at the interface of the two flowing liquids, making the τ_{mix} relatively high. Therefore, long mixing channels or optimized flow rates that thin the diffusion mixing path were used to achieve efficient rapid mixing. To further reduce τ_{mix}, then, transition from a laminar to a chaotic advection regimen, with the introduction of transversal components of the flow that exponentially increase interfacial mixing area, can be achieved in different ways: by moving from a linear mixing channel to channels with different shapes, like simple curves (i.e. serpentine micromixers) or perpendicular turns (i.e. Baffle micromixers); by splitting and recombination of the flow through the addition of obstacles (i.e. Tesla micromixers); by grooved patterns in the mixing channel (i.e. Staggered Herringbone Micromixers - SHM) [45]. SHM allows, in particular, to move to τ_{mix} of few ms [32, 46, 47]. Moreover, SHMs yield the significant advantage of being used with total flow-rates in the range of $mL/_{min}$ [48, 49], rather than in the range of $\mu L/_{min}$ (typical of 2D HFF), and, consequently, offering the possibility of achieving higher production rates. However, SHMs are, still, associated to clogging problems of the device and need parallelization scale-up processing, in order to achieve clinically relevant doses of nanoparticles [50].

From the studies here collected and reported in Table 1, it can be concluded that nanoprecipitation of fully polymeric nanoparticles is mainly obtained with a 2D HFF in cross-junction devices, while the self-assembly of polymeric micelles or liposomes through 2D HFF is implemented by means of cross-junctions and three-inlets Y-junctions. For the development of lipid nanoparticles, for siRNA and mRNA delivery, there is, instead, the widespread use of SHMs, which allows to obtain limit size systems by accelerating the transition from a disk-shaped lipid bilayer to a self-assembled spherical structure through rapid mixing, approaching to dimension of 20 or 30 nm, while keeping encapsulation efficiency of siRNA up to more than 95% [46, 51].

Driven by a biological need, hybrid nanoparticles made of both lipid and polymer material emerged as capable of overcoming the limitation of single bulk material. Indeed, they exploited the biomimetic properties of the lipid shell, for the interaction and uptake from cells, and the rigidity, biocompatibility and biodegradability of

the polymeric core, to give high encapsulation efficiencies, tunable release profiles and superior serum stability.

Alongside the complexity of the hybrid nanostructures produced, also the sophistication of the microfluidic reactors printed has increased. Actually, as can be observed in Table 1, different microfluidic devices were exploited to produce lipid-polymer hybrid nanoparticles.

In 2010 *Hong et* al, firstly, used a 2D HFF in a cross-junction device to produce cross-linked hydrogel nanoparticles covered by a lipid shell; here cross-linking of the hydrogel was obtained off-chip through UV light [52]. *Valencia et al*., in the same year, used a cross-junction followed by a Tesla micromixer to produce PLGA nanoparticles covered by a lipid shell. Moreover, they showed how to finely control PLGA:lipid ratio, identifying the optimal rapid mixing conditions for the formation of a homogenous distribution of hybrid nanoparticles. A lipid-polymer ratio of 1:1, actually, triggers similar rapid mixing timescales for formation of the polymeric core and for the self-assembly of lipid shell, thus determining two final heterogeneous populations, one of hybrid core-shell nanoparticles and one of liposomes. A lipid-polymer ratio of 1:10, allows, instead, the production of a unique and homogeneous hybrid nanoparticle population with prolonged serum stability, thanks to the uniform and complete lipidic coverage of the nanoparticle surface. The authors, also, emphasized how decreasing PLGA-lipid ratio determines a decrease in nanoparticle size, thus showing that PLGA concentration controls the final nanoparticle dimension and lipid concentration, by complete or incomplete coverage, controls the final nanoparticle stability [53].

In the wake of one-stage microfluidic reactors, *Roffo et al*. firstly proposed in 2022 a coupled Hydrodynamic Flow Focusing (cHFF) to produce lipid-polymer hybrid nanoparticles, in a one-step strategy, through a Y-junction microfluidic reactor. The authors showed how, by microfluidic rapid mixing conditions, there is the possibility to control the mutual diffusion of species at the interface, carefully tuning the timescales of the solvent exchange and, thus, inducing simultaneously the precipitation of the chitosan core and the self-assembly of the lipid bilayer shell around the precipitated polymer nuclei [54].

Then, another possibility to produce lipid-polymer hybrid nanoparticles is represented by two different reactors connected in series, where the first one is exploited for the production of the polymer core through a 2D HFF approach via nanoprecipitation, while the second reactor is a micromixer that enhances the covering with the lipid shell, via self-assembly. The potentiality of having two reactors connected in series lies in the fact that, by changing the order of injection of lipid and polymer precursor inside the microfluidic device, is possible to significantly impact on the final nanoparticle outcome. In fact, Sun et al. have injected PLGA solution in the first stage and lipid-PEG solution in the second stage or viceversa, obtaining nanoparticles composed of polymer core covered by a lipid monolayer or bilayer shell. By using the same chemicals and the same microfluidic chip in two different material configurations, they modulated the amount of interfacial water between polymeric core and lipid shell, therefore the rigidity of the NPs and as consequence the cell–particle interaction. Therefore, they demonstrated how the microfluidic may have an important implication in the NPs design [55].

1.2 Droplet Generation: Artificial Cell Production

Droplet generation in microfluidics has been mainly used to produce microparticles or to provide droplets as templates or microreactors to produce nanoparticles. Droplet-based microfluidics is, recently, emerging as a powerful tool to develop artificial cells, moving to a new way to conceive drug delivery systems as biomimetic ones. Artificial cells are systems composed of natural (i.e. biomolecules) and synthetic chemical components, which try to imitate and recapitulate cellular functions and cellular compartmental organization. Potentially, artificial cells, in the form of giant vesicles, polymerosomes, dendrimerosomes or coacervates, can be a tool to investigate phenomena connected to cell membranes, to investigate the mechanisms of action of various cellular structural components (i.e. cytoskeleton biophysics), to study the effect of macromolecular crowding, to analyse cell-cell interactions and communications. Moreover, the use of artificial cells as smart drug and gene delivery vehicles, encapsulating biological machinery, is emerging as a really interesting future perspective in the drug delivery field [56, 57]. Giant liposomes are widely used as artificial cells, since their size approaches the one of eukaryotic cells. *Elani et al* and *Yandrapalli et al.* efficiently encapsulated cells, plasmids, smaller liposomes and microspheres in giant vesicles [58, 59]. *Elani et al*¸ in particular, showed a symbiotic relationship among the host vesicle and the encapsulated cells. These developed systems could be helpful in cell therapy, with the cell encapsulation in microcapsules allowing to deliver in situ secreted proteins to treat pathological conditions, in chemo-enzymatic hybrid cascades, in the study of confinement on biological systems, and in cell-based sensors. *Deng et al.* produced monodisperse coacervate droplets encapsulated within uniform unilamellar liposomes; complex coacervates were composed of disordered proteins and RNA, demonstrating, for the developed artificial cells, storage and release of DNA from the coacervates together with localized transcription [60]. *Ugrinic et al. (2018)* developed proteinosomes based on bovine serum albumin and glucose oxidase conjugated to PNIPAAm chains. The biological activity of proteinosomes can be tailored to encapsulate enzymes and activate multi-step enzyme cascade [61].

The following *Table 7, Table 8* and *Table* 9 report all the studies that have been above described.

PRODUCTION MECHANISM	CHIP GEOMETRY	FLOW REGIME	PROCESSED MATERIALS	ARCHITECTURE	APPLICATION	REFERENCE
NANOPRECIPITATION	Cross-junction	2D HFF	PLGA	Full Polymeric Nanoparticles	Leukaemia	(Leung and Shen, 2018)
			HA		Cancer Delivery/Theranostic	(di Polidoro et al., 2021)
			PLGA, Eudragit	Co-precipitated nanoparticles/ Core-shell nanoparticles	Cancer Delivery	(Zoqlam et al., 2021)
			HA-SH; PEG-VS		Cancer Delivery/Theranostics	(Tammaro et al., 2020)
	Flow Focusing® atomizer		HA	Full Polymeric Nanoparticles	Feasibility Study	(Bicudo and Santana, 2012)
			PLGA		DNA delivery	(Martin-Banderas et al., 2013)
	Foldable Origami chip		PLGA		Cancer Delivery/Theranostic	(Sun et al., 2013)
	Staggered Herringbone Micromixers	Chaotic Advection	PLGA	Full Polymeric Nanoparticles	Feasibility study	(Roces et al., 2020)
			PLGA		Cancer Delivery	(Morikawa et al., 2018)
			PLGA, Chitosan, PEG	Co-precipitated nanoparticles/ Core-shell nanoparticles	Drug Encapsulation	(Essa et al., 2020)
	(HPIMM)	Mixing by diffusion mass transfer	PMMA	Full Polymeric Nanoparticles	Feasibility study	(Bally et al., 2012)
	Impact-jet micromixer		PMMA		Drug Encapsulation	(Anton et al., 2012)
	Co-axial assembly	Co-flow & Flow-focusing	PCL/PLA		Feasibility study	(Othman et al., 2015)
SELF-ASSEMBLY	Cross-junction	2D HFF	Phospholipids	Liposomes	Feasibility Study	(Jahn et al., 2004)
			DMPC, DSPE-PEG2000, DSPE-PEG2000-Folate, Cholesterol, DCP		Cancer Delivery	(Ran et al., 2016)
			DMPC, DSPE-PEG2000, DSPE-PEG2000-Folate, DSPE-PEG2000-Mal, DSPE-PEG2000-TAT, Cholesterol			(Ran et al., 2018)
			Hydrophobically modified chitosan	Polymeric Micelles	Drug Encapsulation	(Dashtimoghadam et al., 2013)
			Hydrophobically modified chitosan			(Majedi et al., 2013)
			P2VP-PEO		Feasibility Study	(Thiele et al., 2010)
			PLGA-PEG-COOH; PLA-Pt(IV)		Cancer Delivery	(Kolishetti et al., 2010)
			PLGA-PEG		Feasibility Study	(Karnik et al., 2008)
			PEG-PLGA			(Baby et al., 2017)

Table 7 *– summary of microfluidic devices for nanoparticles production by nanoprecipitation and self-assembly*

PRODUCTION MECHANISM	CHIP GEOMETRY	FLOW REGIME	PROCESSED MATERIALS	ARCHITECTURE	APPLICATION	REFERENCE
SELF - ASSEMBLY	Cross-junction & 3-inlets Y-junction	2D HFF	DMPC, DCP	Liposomes	Feasibility study	Jahn et al., ACS NANO (2010)
			HSPC, mPEG-DSPE, cholesterol			(Zizzari et al., 2017)
	3 inlets Y-junction		DOTAP, DOPE, DOPC, DSPE-PEG 2000, DSPE-PEG(2000)-FolA	Lipid nanoparticles	RNA delivery	(Krzyszton et al., 2017)
			Pluronic F-127	Polymeric Micelles	Osteogenic Differentiation	(Capretto et al., 2013)
			PMOXA-b-PDMS-b-PMOXA		Cancer Delivery	(Liu et al., 2015)
			Pluronic F-127		Leukaemia	(Capretto et al., 2012)
	T-junction	Rapid Mixing	Cationic Lipids: CLinDMA, Cholesterol, PEG-DMG	Lipid nanoparticles	RNA delivery	(Abrams et al., 2010)
	Staggered Herringbone Micromixers	Chaotic Advection	DSPC, DMAP-BLP, PEG-DSG			(Chen et al., 2016)
			C12-200, DSPC, Cholesterol, C14-PEG 2000)			(Kauffman et al., 2015)
			DLinK-DMA, DSPC, PEG-lipid			(Belliveau et al., 2012)
			LP01 lipid, cholesterol, PEG2k-DMG			(Finn et al., 2018)
			PLA-PEG, PLGA	Polymeric Micelles	Feasibility Study	(Abstiens and Goepferich, 2019)
	Baffle mixer		POPC, DOPC, PEG-DMG, Cholesterol	Lipid nanoparticles	RNA delivery	(Kimura et al., 2018)
	Chaotic micromixer	Chaotic mixing	POPC	Liposomes	Feasibility study	(Maeki et al., 2017)
	Two-phase gas–liquid microfluidic reactor		P(MCL-co-CL)-b-PEO	Polymeric Micelles	Cancer Delivery	(Cao et al., 2019)
	Three-tier microchannels	Parallel Flow Focusing	mPEG–PLGA		Feasibility Study	(Kang et al., 2013)
	3D HFF	3D HFF	PLGA-PEG			(Rhee et al., 2011)
			PLGA-PEG		PK and biodistribution	(Lim et al., 2014)
			PLGA, PLGA-PEG			(Valencia et al., 2013)
	Multicapillary Array		DPPC, cholesterol, DSPE-PEG 2000	Liposomes	Feasibility study	(Hood et al., 2014a)

Table 8 *– summary of microfluidic devices for nanoparticles production by nanoprecipitation and self-assembly (continued)*

PRODUCTION MECHANISM	CHIP GEOMETRY	FLOW REGIME	PROCESSED MATERIALS	ARCHITECTURE	APPLICATION	REFERENCE
HYBRID	3-inlets Y-junction	2D HFF	SPC, cholesterol, chitosan	Lipid-polymer Hybrid core-shell nanoparticles	Cancer Delivery/Theranostic	(Roffo et al., 2022)
	Cross-junction		Phospholipids, Cholesterol, PNIPA		Feasibility Study	(Hong et al., 2010)
	Microvortex Platform	3D HFF	PLGA, lectin, DSPE-PEG			(Kim et al., 2012)
			PLGA, SHPC, DSPC, DMPC, MHPC, DSPE-PEG2000, rhodamine-DMPE, ApoA-I		Atherosclerosis	(Sanchez-Gaytan et al., 2015)
	Two-stage microfluidic chip	2D HFF/ Rapid Mixing	PLGA, DPPC, DSPE-PEG, cholesterol		Cancer Delivery	(Feng et al., 2015)
			Polymer mixture (PLGA, CPP, POE), DPPC, DSPE-PEG, cholesterol			(Zhu et al., 2020)
			DPPC, DSPE-PEG2000, TopFluor-PE, NBD-SPEPLGA			(Sun et al., 2015)
			PLGA; mPEG5K-PLGA55K; peptide; DPPC; DSPE-PEG		Peptide Delivery	(Han et al., 2021)
	Cross-junction / Serpentine Micromixer		PEI-800, Cationic Lipids		RNA Delivery	(Huang et al., 2017)
	Two-stage microfluidic chip	2D HFF/Rapid Mixing	N -palmitoyl chitosan, Eudragit	Multi-polymer Hybrid core-shell nanoparticles	Cancer Delivery	(Hasani-Sadrabadi et al., 2016)
	3 inlets Y-junction/Spiral Micromixer		PLGA, PEG-b-PDPA			(Feng et al., 2017)

Table 8 *– summary of microfluidic devices for hybrid nanoparticles production*

PRODUCTION MECHANISM	CHIP GEOMETRY	FLOW REGIME	PROCESSED MATERIALS	ARCHITECTURE	APPLICATION	REFERENCE
DROPLET GENERATION	Double cross-junction/Serpentine	Double emulsion W/O/W	Plasmid DNA, calcein, Single Unilamellar Vesicles, POPC, DOPS, DiD/DiIC18 (3)/Liss Rhod PE	Giant Unilamellar Vescicle	Artificial Cell	(Yandrapalli et al., 2021)
	Cross-junction/Serpentine	Single emulsion	Cells (bacterium, eukaryotic cell line), POPC	Biological Cells-containing Vescicle	Artificial Cell	(Elani et al., 2018)
	Co-axial assembly	Double emulsion W/O/W	Polycations, Polyanions, egg PC	Coacervate Organelles-containing liposomes	Artificial Cell	(Deng and Huck, 2017)
	Cross-junction	Single emulsion	BSA-NH2/PNIPAAm, GOx-NH2/PNIPAAm	Proteinosomes/Polymerosomes	Artificial Cell	(Ugrinic et al., 2018)

Table 9 *– summary of microfluidic devices for droplet generation*

List of Abbreviations (*Table 7,8,9***)**: PLGA, poly(lactic-co-glycolic acid) ; HA, Hyaluronic Acid; HA-SH, thiolated Hyaluronic Acid; PEG-VS, Polyethylene glycol-vinyl sulfone; PEG, Polyethylene glycol; PMMA, Poly(methyl methacrylate); PCL, Polycaprolactone; PLA, poly(lactic acid); DMPC, 1,2-dimyristoyl-sn-glycero-3-phosphocholine; DSPE-PEG200, 1,2-distearoyl-sn-glycero-3-phosphoethanolamine-N-[methoxy(polyethylene glycol)-2000]; DSPE-PEG2000-Folate, 1,2-distearoyl-sn-glycero-3-phosphoethanolamine-N-[folate(polyethylene glycol)-2000]; DCP, dihexadecyl phosphate; DSPE-PEG2000-Mal, 1,2-distearoyl-sn-glycero-3-phosphoethanolamine-N-[maleimide(polyethylene glycol)-2000]; P2VP-PEO, Poly-2-vinylpyridine-b-poly(ethylene oxide); PLGA-PEG, poly(lactideco-glycolide)-b-poly(ethylene glycol); HSPC, hydrogenated soy phosphatidylcholine; mPEG2000-DSPE, N-(carbonyl-methoxypolyethylene glycol 2000)-1,2-distearoyl-snglycero-3-phosphoethanolamine; DOTAP, 1,2-dioleoyl-3-trimethylammoniumpropane; PMOXA-b-PDMS-b-PMOXA , poly(2-methyl-2-oxazoline)-block-poly(dimethylsiloxane)-block-poly(2-methyl-2-oxazoline); CLinDMA, (2-[62]-N,N-dimethyl-3-[(9Z,12Z)-octadeca-9,12-dien-1-yloxy]propan-1-amine]; PEG-DMG, methoxylene glycol 2000 ether; POPC, 1-Palmitoyl-2-oleoyl-sn-glycero-3-phosphocholine; P(MCL-co-CL)-b-PEO, poly(methyl caprolactone-co-caprolactone)-block-poly(ethylene oxides); SPC, L-α-Phosphatidylcholine; PNIPA, Poly(N-isopropylacrylamide); SHPC, 1-Stearoyl-2-hydroxy-sn-glycero-3-phosphocholine; PEI-800, polyethylenimine-800; PEG-b-PDPA, poly(ethyleneglycol)-poly(2-(diisopropylamino)ethyl methacrylate); DOPS, 1,2-dioleoyl-sn-glycero-3-phospho-L-serine; Liss Rhod DOPE, 1,2-dioleoyl-sn-glycero-3-phosphoethanolamine-N-(lissamine rhodamine B sulfonyl); DiIC18 (3)), Dioctadecyl-3,3,3′,3 tetramethylindotricarbocyanine perchlorate; DiD, DiIC18 (5); egg PC, l-α- phosphatidylcholine; BSA-NH2/PNIPAAm, cationized bovine serum albumin/PNIPAAm; Ox-NH2/PNIPAAm, glucose oxidase/PNIPAAm.

2. Aim of the work

In this chapter, we introduce microfluidics as a disruptive and powerful tool to finely and precisely tune the design properties of the delivery vectors, moving from simple to complex architectures as required.
We illustrate this through two case studies of cross-linked Hyaluronic Acid Nanoparticles (cHANPs) and PLGA microparticles production. By controlling microfluidics production process parameters, we demonstrate the ability to generate extremely homogenous batch of micro/nano particles with well-defined and controlled properties. Looking ahead, this opens the opportunity to investigate the role that each single design feature of the delivery vector in consideration has in determining the final fate in an *in vivo* biological environment.

3. Materials and Methods

3.1 Materials

3.1.1 PLGA microparticles

Poly (D, L-lactide-co-glycolide) (50:50) (PLGA) (Resomer RG 504H) was purchased from Boehringer Ingelheim (Germany), Poly (vinyl alcohol) (PVA) (Mowiol 40-88) was purchased from Merck Life Science S.r.l., Ethyl Acetate was purchased from Sigma Aldrich, Milli-Q Plus water was used for synthesis and characterization and Sulforhodamine was purchased from Sigma Aldrich.
PLGA is a FDA approved polymer for a wide range of therapeutic applications in drug delivery, tissue engineering, medical and surgical devices thanks to its biocompatibility, biodegradability, non-toxicity and sustained-release properties[63]; the structure of the one used in this study is reported in *Figure 3*. Ethyl acetate was chosen as alternative to chlorinated solvents (*i.e.,* dichloromethane and chloroform), since the use of these last ones determines issues for the environment and the human health [64].

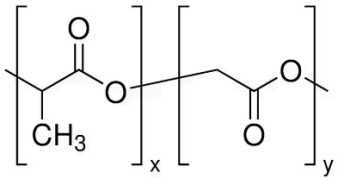

Figure 3 *– Resomer RG 504H structure*

PVA, whose chemical structure is reported in *Figure 4*, was chosen as surfactant in the continuous phase for the stabilization of the dispersed phase (*i.e.,* constituted by ethyl acetate and PLGA), as previously reported by other authors in the batch production of PLGA microparticles[65].

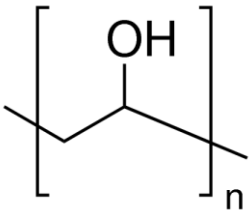

Figure 4 *– PVA (Mowiol 40-88) structure*

3.1.2 cHANPs

Sodium Hyaluronate HA (Mw=50000 Da) was purchased from Creative PEGWorks, DVS (contains $<$ 650 ppm hydroquinone as inhibitor; purity 97%; density 1,117 g/ml at 25°C (lit.)) was purchased from Merck KGaA (Germany), Gd-DTPA ($MW = 547{,}43\ {}^{g}/_{mol}$) was purchased from Merck KGaA (Germany), Sodium Hydroxide NaOH (ACS reagent, ≥97,0%, Mw=40,00), ATTO633 was purchased from ATTO-TEC GmbH, Milli-Q Plus water was used for synthesis and characterization.

Hyaluronic Acid (HA), also known as hyaluronan, is a naturally occurring linear polysaccharide, belonging to the glycosaminoglycan family, composed of repeating disaccharide units of D-glucuronic acid and N-Acetyl-D-glucosamine linked by β-1-3 and β-1-4 glycosidic bonds (*Figure 5*).

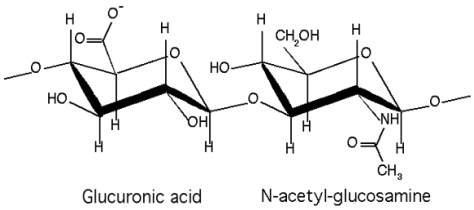

Figure 5 *– HA chemical structure*

Hyaluronic acid is one of the main constituents of the Extracellular matrix (ECM) of human connective tissues and it comes in different molecular weight. HA is involved in maintaining tissue viscoelasticity and in interactions with cell surface receptors, such as CD44, and other ECM molecules, promoting cell adhesion, migration, proliferation and tissue repair. It shows a strong hydrophilic character that allows it to absorb and bind to very large amount of water, up to 1000 times its solid volume. Due to its biocompatibility, biodegradability, non-toxicity, non-immunogenicity and ease of chemical modification and formation process, HA has become a carrier of great interest.

However, when it is used without any kind of modification, it suffers from poor residence time in vivo, caused by its rapid enzymatic degradation; hyaluronidase is the enzyme responsible for HA cleavage. Thus, it is necessary to introduce some modification that help to cross-link HA polymer network in order to improve its biomechanical and biological properties.

Several chemical modification and crosslinking of HA have been achieved, by exploiting, mainly, three different groups on the polymer backbone: carboxyl groups (-COOH), hydroxyl groups (-OH) and N-acetyl groups (–$NHCOCH_3$). Carboxyl groups modification is achieved by activating such groups, for example by means of carbodiimides, and making them to condensate with amino groups forming amine bonds with adjacent polymer chains. The modification of –$NHCOCH_3$ groups include, among others, deacetylation and amidation, and allow to make such groups react with an acid. Finally, chemical modification of –OH groups can be divided into four different groups: ether formation, ester formation, hemiacetal formation and oxidation[66]. In the context involving the oxidation modification of –OH groups, it's located the cross-linking reaction with Divinyl Sulfone (DVS) exploited in this work. Divinyl sulfone is a sulfone compound having two S-vinyl substituents; its molecular formula is $(CH_2 = CH)_2SO_2$; its chemical structure is reported in *Figure 6* and its molecular weight (MW) is 118,15 $^{g}/_{mol}$.

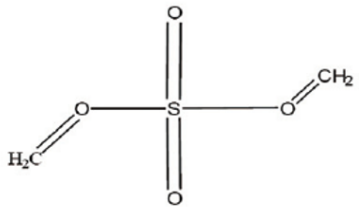

Figure 6 *– DVS molecular structure*

It acts as a cross-linking agent for HA, involving an Oxa-Michael addition mechanism occurring in an alkaline medium. The first step of the reaction is the deprotonation of hydroxyl at alkaline medium. Each deprotonated –OH ion will then react with the electron-deficient double bond in one vinyl sulfone group of DVS; reaction scheme is reported in *Figure 7*.

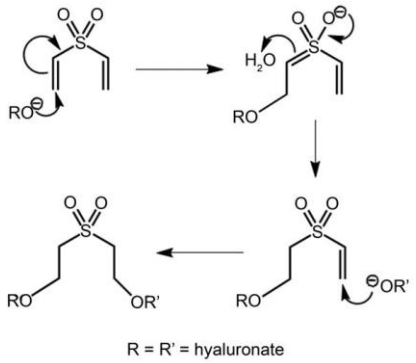

Figure 7 *- Oxa-Michael addition mechanism*

The pH of the solution has to be carefully controlled in order to tune the crosslinking degree of HA and DVS; the optimal pH range has been found between 11.79 and 12.63. HA crosslinked with DVS has the very important advantage of retaining biocompatibility and physical properties of unmodified HA. Moreover, HA-DVS degradation products have been proved to not induce toxicity and, so, they are FDA approved.

More specifically, hyaluronic acid hydrogels have been proved to be useful in designing nanostructures for enhanced MRI. So, hydrogels are able to increase the relaxivity of the contrast agent (*i.e.* metal chelate) without any chemical modification and to achieve brighter contrast with a lower amount of metal chelate, thus reducing the administered dose. These effects are explained by *Hydrodenticity*: HA hydrogels encapsulating a Gd-based contrast agent show relaxivity boosting of the contrast agent up to 12 times. This is related to the formation of water domains or clusters around the contrast agent within the polymer matrix, due to the complex equilibrium established among osmotic pressure, polymer elastodynamic forces and contrast agent hydration degree. Water is in abnormal aggregation state around contrast agent, and this influences its relaxivity.

3.2 Methods

3.2.1 Droplet Generation in Microfluidics: droplets as template for microparticles production

Droplet-based microfluidics is exploited for the production of droplets with a controlled size and at high frequency. The produced droplets can be used as templates for the synthesis of microcapsules, microparticles and microfibers or as microreactors for lab-on-chip applications [67, 68].

When using passive microfluidic devices to originate droplets, two immiscible phases come in contact; the dispersed phase is introduced into the continuous one and this, consequently, generates an immiscible and unstable interface between the two phases which induces the formation of droplet in five different regimes: squeezing, dripping, jetting, tip-streaming and tip-multi-breaking (*Figure 8*).

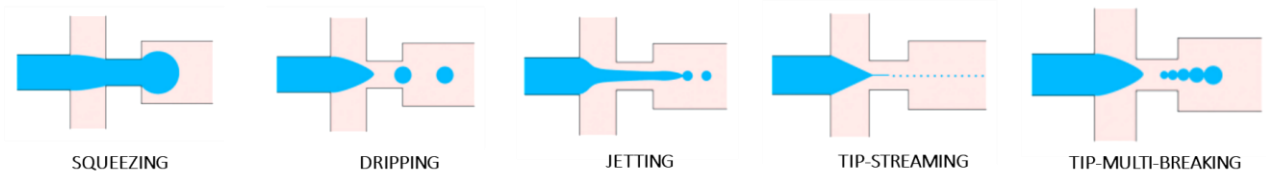

Figure 8 *– different regimes for droplet generation in passive devices (modified from)* [68]

Formation of droplet by squeezing regime is mainly due to the effect of channel confinement, while the other four regimes rely on capillary instabilities[68].

3.2.2 Nanoprecipitation and Microfluidic Advantages

Nanomedicine is the application of nanotechnology to medicine, involving the use of engineered nanomaterials for therapy and diagnosis of major diseases, such as cancer. Nanoparticles are particles with dimension in the

range of about few to hundreds of nanometres. Methods for producing organic NPs are typically divided in two different categories: *top-down* and *bottom-up* approaches. In the first case, the starting point is represented by macroscopic material reduced to nanometre size with different techniques, among which the most reliable is represented by mechanical milling. Such approaches have not found widespread use in pharmaceutical field, due to particles agglomeration and contamination issues.

In the second case, the bottom-up approach, the starting point is represented by molecular matter dispersed in a liquid or gas phase which is converted, through a condensation process, into NPs. Bottom-up approaches can be further classified into emulsion-based and nanoprecipitation process. Nanoprecipitation-based process to produce NPs seems to be a very promising and powerful method. *Elaissari et al.* proposed two different mechanisms in order to explain the formation of NPs by means of nanoprecipitation. *Solvent phase* consists of a solution of the film-forming substance (i.e. polymer) in a solvent or in a mixture of solvents; the *non-solvent phase* consists of a non-solvent or a mixture of non-solvents for the film-forming substance. The nanoprecipitation method is based on the creation of a supersaturated solution and comprises three different stages: nucleation, growth and aggregation. Precipitation occurs at the onset of supersaturation, which means that the polymer concentration, following a system perturbation, increases overcoming the saturation limit (i.e. polymer solubility). In this way a critical concentration is reached, and the precipitation process is triggered. As represented in *Figure 9*, the first step of nanoprecipitation is represented by *nucleation phase*, in which nuclei, formed by condensation of monomers, begin to spontaneously precipitate. Nucleation phase proceeds until nuclei reach a critical size associated to a state of energetic stability against dissolution and polymer concentration falls again below the critical nucleation threshold. At this point, a *growth phase* begins; here formed nuclei start to capture remaining dissolved solute. Growth phase proceeds, on the other hand, until the concentration of the still dissolved polymers falls to the equilibrium concentration (i.e. bulk solubility). Finally, in the *aggregation phase* grown nuclei may aggregate among them, affecting the size of the final produced NPs.

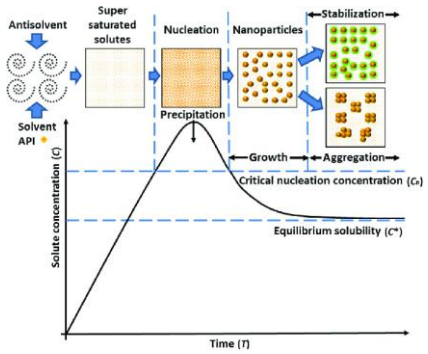

Figure 9 – *Nanoprecipitation principle*

Second explanation for nanoprecipitation is based on the Gibbs-Marangoni effect, according to which NPs are formed due to differences in surface tension: the aqueous phase, possessing a surface tension higher with respect to the organic phase solvent, pulls more strongly on the surrounding liquid and, so, the solvent flows from regions of lower surface tension and the polymer tends to aggregate on the oil surface, forming

nanocapsules. According to this explanation, nucleation and growth phase are not involved in the nanoprecipitation process.

In order to obtain NPs with a narrow size distribution, so characterized by a low polydispersity index, at least two conditions need to be satisfied: nucleation needs to occur in a short period compared to the growth phase; a homogenous environment, in terms of temperature and polymer concentration, is required in the first two phases. For these reasons, an extraordinary control over process parameters is essential in order to produce materials with desired and required features. In this context, microfluidics has emerged as a very powerful tool in order to produce NPs with highly reproducible properties and improved formulation.

Microfluidics deals with miniaturized system that process and manipulate small amounts of fluids ($10^{-9}\ to\ 10^{-18}$), by means of channels with dimensions ranging from tens to hundreds of micrometres. Microfluidic technologies rely on the concept of "shrinking" traditional bench chemical systems down to the size of few centimetres squared. Small channel dimensions allow to have a large surface-to-volume ratio, which enables a rapid and uniform heat and mass transfer, significantly improving NPs size distribution and avoiding the formation of undesirable by-products. However, a microfluidic device is not simply a miniaturised version of its macroscale counterpart. Actually, flow conditions are completely modified in microfluidic systems with respect to the macroscale and Reynolds number is evaluated in order to understand the way in which such changes occur. Reynolds number (Re) is defined as the ratio of inertial to viscous forces, as it follows:

$$Re = \frac{\rho u L}{\mu} = \frac{uL}{\nu}$$

Here, ρ is the fluid density, u is the mean fluid velocity, L is the characteristic length of the system, μ is the fluid dynamic viscosity and ν is the fluid kinematic viscosity. Microfluidic systems are characterized by $Re < 100$ and, thus, the flow is regarded as laminar, which means that fluids flow in parallel layers with no cross currents perpendicular to the main flow direction. At low Re viscous effects dominate over inertial ones and, therefore, mass transfer by advection can occur only in the direction of the fluid and mixing between streams occurs mainly by molecular diffusion, which is a relatively slow process. Actually, when dealing with a diffusion dominated process, the time t which is required for a species to diffuse scales quadratically with the distance x covered through the diffusion coefficient $\mathcal{D}$; one-dimensional diffusion process can be modelled as it follows:

$$x^2 = 2\mathcal{D} \times t$$

A reduction in diffusion distance to cover has the effect to drastically reduce the time for complete mixing relying only on diffusion. In this way, fast and efficient mixing of the solvent with non-solvent phase is carried out within microfluidic devices. An efficient solution to reduce mixing path is represented by Hydrodynamic

Flow Focusing (HFF). In hydrodynamic focusing, a central sample solution, supplied from the central inlet, flows within the sheath of outer fluids, supplied from the side inlets. In this way, the inner sample flow is constrained laterally to achieve a smaller stream and a thin lamination width; more specifically, the solvent stream is squeezed between two non-solvent streams, determining at the interface a rapid and mutual exchange of solvent by diffusion. The extent of the width decrease of the focused stream depends on the volumetric flow rate ratio (FR^2), defined as the ratio of the central inlet flow rate over the side inlets flow rate. The greater the flow rate difference, the greater the degree of width reduction. Decreasing the stream width means that the diffusion path length is reduced, which results in faster mixing. The width of the focused stream (w_f) is computed by Capretto et al., applying the conservation mass principle; the volume of sample liquid that passes through the inlet channel (Q_2) has to match the volume of the focused stream (Q_f):

$$Q_2 = w_2 v_2 h = w_f v_f h = Q_f$$

Here, w_2 is the width of the central inlet channel and v_2 is the average velocity of the flow in the central inlet channel; v_f is the average velocity of the focused stream. Finally, h is the height of the channels. This leads to:

$$w_f = \frac{Q_2}{v_f h}$$

Mixing time directly influences final NPs size and NPs size distribution, so two different time scales have to be considered: the mixing timescale (τ_{mix}) and the aggregation timescale (τ_{agg}). Mixing timescale is defined as it follows:

$$\tau_{mix} = \frac{{w_f}^2}{4\mathcal{D}}$$

Aggregation timescale is the characteristic timescale for chains to nucleate and grow found in the range between $10 - 100\ ms$, depending on the molecular weight of the polymer chains. Two different conditions may occur:

- $\tau_{mix} > \tau_{agg}$ yielding to assembly of nanoparticles before the solvent exchange is completed, determining a heterogeneous environment affecting size distribution;
- $\tau_{mix} < \tau_{agg}$ yielding to particles self-assembly when solvent exchange is completed, determining a homogeneous environment which results in nanoparticles characterized by lower polydispersity.

3.2.3 Microfluidic platform and scale-up of cHANPs production process

A hydrodynamic flow focusing approach has been used in order to produce cHANPs, while a droplet generation approach has been used for PLGA microparticles production. The microfluidic set-up is composed as it follows:

- A quartz microfluidic device "Droplet Junction Chip, 190 μm etch depth" is purchased from Dolomite Centre Ltd. The device comprises both an X-junction and a T-junction, but the first one has been exploited in this work to produce cHANPs and PLGA microparticles. X-junction is made up by three inlet channels and a single outlet channel used to mix and induce the reaction of the reagents. Chip and its geometry are reported in the following *Figure 10*:

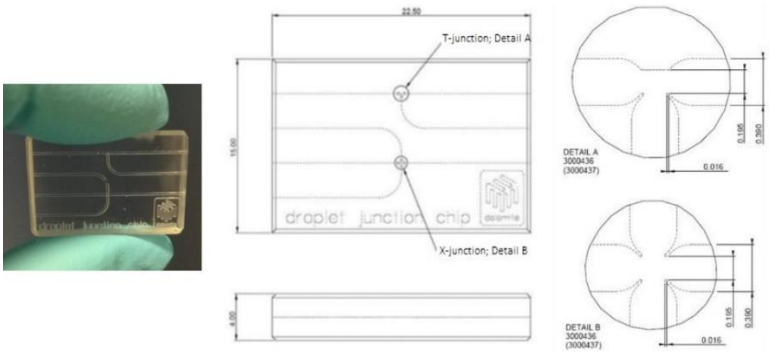

Figure 10 *– a) Droplet Dolomite chip; b) chip geometry*

- The device is connected to glass syringes, purchased from Microsyringes ILS Innovative Labor System. Syringes are connected to the device with FEP tubing ($1/16'' \times 0.25mm$) by means of ETFE valves, which allow to quickly start or stop flow streams. Tubes are connected to the device through a H-interface and PTFE linear connectors.
- Low Pressure Syringe Pump NEMESYS 290N (CETONI) is used to control each syringe.
- NeMESYS PC user interface allows to select channels flow rates and syringe volumes. Flow Rate Ratio (FR^2) is defined as it follows:

$$FR^2 = \frac{middle\ channel\ flow\ rate}{side\ channel\ flow\ rate}$$

- Flow-focusing is observed using an Optical Fluorescent Microscope (Olympus IX71) with a 4 or 10 x scanning objective.

A second set of experiments is conducted on Telos® System, to scale-up cHANPs production process. The Telos® System (*Figure 11*) is a breakthrough product for parallel microfluidic processes, including emulsion generation, micro-particle production, high throughput mixing, microreactions and Hydrodynamic Flow Focusing. Recently, for example, PLGA microparticles in the range between $10 - 40\ \mu m$ have been produced

using Telos® with an HFF approach. This modular, scalable, and highly flexible system removes the low throughput limitation of individual microfluidic chips. The Telos® System can be run with up to ten modules in parallel, each supplying a chip from common fluid inputs. Each module has independent valving and holds a microfluidic chip typically with 7 junctions, enabling a total of 70 parallel junctions to be run at once.

Figure 11 *- Ten module Telos® system*

Fluid flow stream is driven inside Telos® system by means of Mitos P-Pumps equipped with flow-sensors or by means of Mitos P-Pump Remote Chambers, whit the last ones enabling the managing of higher amounts of fluids. All Mitos P-Pumps provide pulseless liquid flow with a precise pressure driven pumping mechanism. All the system is powered by a pneumatic supply. Tubes connecting pumps to Telos® system have a diameter of $1.6 \times 0.25\ mm$. The configuration used in this work is reported in the following *Figure 12*:

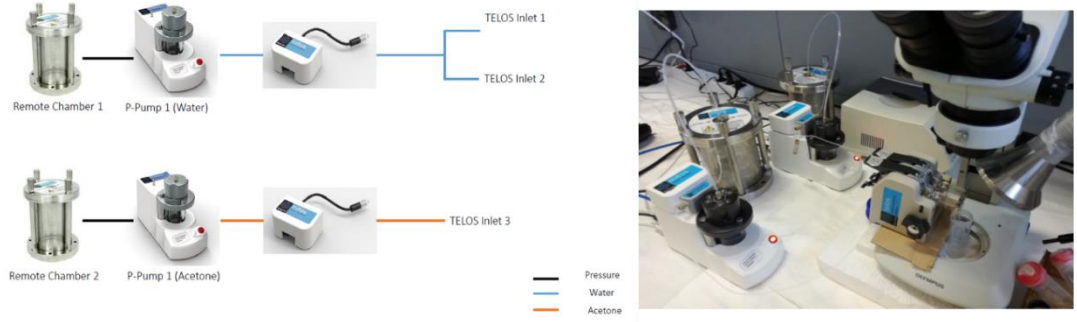

Figure 12 *- Telos® configuration*

A Telos®2 Reagent Chip (*Figure 13 a*) with size channel of $100\mu m$ is used in this work. Solvent solution is fed in inlets 1 and 2 (red and blue in *Figure 13 b*), while non-solvent solution is fed in inlet 3 (yellow in *Figure 13 b*). Inlet 1 and inlet 2 meet forming the central channel of the X-junction characterizing Telos® chip. Inlet 3 instead is split in the two side channels constituting the X-junction. In this work, two Mitos P-pumps and two Remote Chambers have been used:

- Solvent solution is placed inside one P-pump and then, a bifurcation is present to split and feed the flow in inlets 1 and 2.
- Non-solvent solution is placed inside the other P-pump and fed the inlet 3.
- Remote chambers are used to pump water and acetone for chip washing purposes.

Mitos P-pumps are connected to a computer and controlled by means of the "Flow Control Center Software", which allows to impose pressure or flow-rate; the last case is possible when the pump is equipped with a flow sensor (Mitos Sensor Interface from Dolomite). The sensor reads the fluid flow rate, and the pump pressure is automatically adjusted to meet the target flow-rate. In this work the water (solvent) pump is equipped with a flow sensor. The acetone (non-solvent) pump, instead, is not equipped with a flow sensor, but the pressure is imposed to achieve the desired flow rate based on calibrations. Such calibrations are done simply pumping water and acetone inside the chip, without any other components.

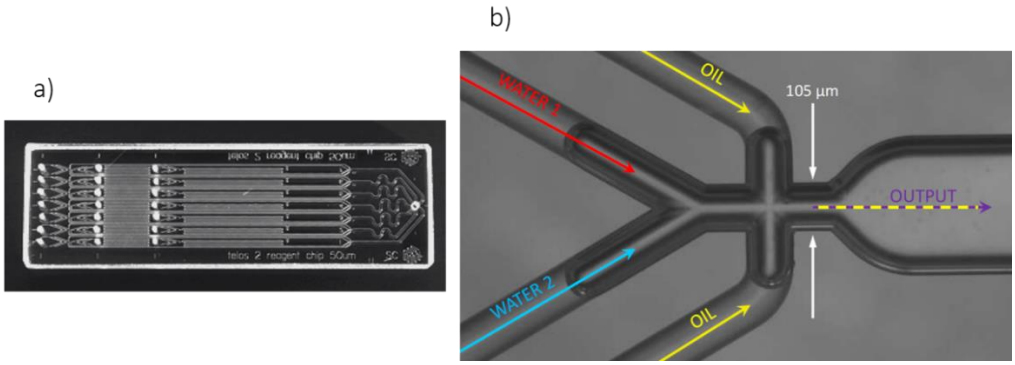

Figure 13 *- a) Telos®2 Reagent Chip; b) Junction geometry and flow path*

3.3 Microparticles and Nanoparticles Production

3.3.1 PLGA microparticles production protocol

Dispersed phase is loaded into a 5 mL glass syringe, which flows in the central channel. Dispersed phase is constituted by ethyl acetate, PLGA (5% w/V) and, preliminarily, sulforhodamine. When sulforhodamine is encapsulated in the microparticles, a co-solvation of ethyl acetate and water is performed to increase the active agent solubility in ethyl acetate. In particular sulforhodamine is injected at a concentration of 0,125 $^{mg}/_{mL}$, with water at 1,5% V/V of the final dispersed phase solution. Continuous phase is loaded in two 10 mL syringes, flowing in the side channels. Continuous phase is constituted by water and PVA (2% w/V). The collection is performed in a vial containing 2 mL water and PVA (2% w/V). The experiment is ended after 60 minutes and the sample is maintained in stirring overnight on the wheel at 30 RPM.

3.3.2 cHANPs production protocol

Solvent solution is loaded into a 2.5 mL glass syringe, which flows in the central channel. Solvent solution consists of water, HA, Gd-DTPA encapsulated together with ATTO488 or ATTO633, obtaining Multimodal

Imaging cHANPs, or encapsulated together with Irinotecan, producing Theranostic cHANPs. To prepare 5 mL of solvent solution to be loaded, the following steps are performed.
Specifically, to produce cHANPs encapsulating Gd-DTPA and ATTO488 or ATTO633, addition to the solvent solution of:

- 1 mL of Gd-DTPA (0.1% $^{w}/_{V}$) from a stock solution at 0.5% $^{w}/_{V}$.
- 500 μL of HA (0.05 % $^{w}/_{V}$) from a stock solution at 0.5% $^{w}/_{V}$.
- 50 μL of NaOH (1% $^{V}/_{V}$) from a stock solution at 1M to obtain a pH in the range $12 - 12.2$.
- 50 μL of ATTO488 or ATTO633 from a stock solution at 1 $^{mg}/_{mL}$.
- 3,4 mL of Water.

To produce cHANPs encapsulating Gd-DTPA and Irinotecan, addition to the solvent solution of:

- 1 mL of Gd-DTPA (0.1% $^{w}/_{V}$) from a stock solution at 0.5% $^{w}/_{V}$.
- 500 μL of HA (0.05 % $^{w}/_{V}$) from a stock solution at 0.5% $^{w}/_{V}$.
- 50 μL of NaOH (1% $^{V}/_{V}$) from a stock solution at 1M to obtain a pH in the range $12 - 12.2$.
- 50 μL of Irinotecan from a stock solution at 1 $^{mg}/_{mL}$.
- 3,4 mL of Water.

Solvent solution is maintained in magnetic stirring at 230 RPM for 15 minutes.
Non-solvent solution, on the other hand, is loaded into two 10 mL glass syringes, which feed the two lateral channels. It is composed by acetone and DVS:

- 1 mL of DVS at 4 M concentration.
- 24 mL of acetone.

Non-solvent solution is maintained in magnetic stirring at 230 RPM for 15 minutes.
To perform the experiment:

- Microfluidic device is mounted on the support for Optical Microscope and connected to syringes.
- NeMESYS platform and user interface are launched.
- Syringe volumes and flow rates are selected.
- The collection is performed in a Petri-dish containing 20 mL of non-solvent acetone.
- Before starting the experiment and at the end of the experiment washing of the chip alternating acetone and water are performed.

After the experiment has ended, the sample is maintained in stirring overnight on the wheel at 30 RPM.

3.4 Microparticles and nanoparticles characterization

3.4.1 Dynamic Light Scattering (DLS)

Dynamic Light Scattering (DLS) is an analytical technique used to measure particles size distribution of formulations in the range of approximately 1 nm to 1 μm. Particles in solution are continuously subjected to Brownian motion, determined by the bombardment of surrounding solvent molecules. Depending on their size, they will move faster or slower: large particles diffuse slowly resulting in similar position at different time points; small particles move faster and do not adopt a specific position in time. Particles movement is not only dependent on their size, but also on solvent viscosity and temperature. DLS measurement is based on monitoring the Brownian motion of particles in a specific range of time; in this way information on the size of particles can be obtained. The size of a particle is calculated from the translational diffusion coefficient $\mathcal{D}$ using the Stokes-Einstein equation:

$$R_H = \frac{kT}{6\pi\eta\mathcal{D}}$$

where k is the Boltzmann's constant, T is the absolute temperature, η the solution viscosity and R_H is defined as hydrodynamic radius.

The radius that is measured in DLS, actually, is a value that refers to how a particle diffuse within a fluid and, so, it's the radius of a sphere that moves with the same translational diffusion coefficient as the particles.

DLS machinery (*Figure 14*) is constituted by a laser that illuminates the sample contained in a cuvette. Fluctuations, so random changes, of the scattered light intensity are detected at a known scattering angle by a fast proton detector.

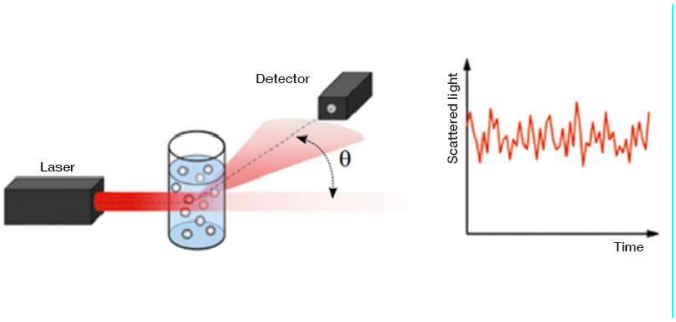

Figure 14 *- DLS machinery*

A digital auto-correlator then correlates intensity fluctuations of scattered light with respect to time ($ns - \mu s$) to determine how rapidly the intensity fluctuates, which is related to the diffusion behaviour of

macromolecules. Actually, smaller particles that move at higher speeds show faster fluctuations with respect to larger particles.

Laser light intensity is carefully adjusted by means of an attenuator. For example, for samples that do not scatter much light, due to small particles or to a very low concentration of the sample, the amount of scattered light being detected has to be increased. So, the attenuator will automatically allow more light to pass through the sample and viceversa. Beyond attenuator, another very important parameter that has to be considered to appreciate the quality of the measurement is the count rate or photon count rate. Count rate is simply the number of photons detected which needs to be above a minimum value in order to have enough signal for the analysis. The two parameters that we can directly measure through DLS analysis are the Z-average and the Polydispersity Index. Z-average gives the mean size determined as an intensity weighted average of the light fluctuations; while the Polydispersity Index (PDI) is measured as it follows:

$$PDI = \frac{\sigma^2}{2R_H}$$

Where σ is the standard deviation of a hypothetical Gaussian distribution centred on the Z - average. Particles are measured at 25 °C, using a Zetasizer Nano ZS (Model ZEN3600, Malvern Instruments Ltd., UK). The wavelength of the laser is $\lambda = 630\ nm$ and scattering angle used is $\theta = 173°$. The cuvettes used are the 12mm square glass cuvettes for 90° sizing (PCS8501), containing $1\ mL$ of sample. The average size on three repeated measurements is always considered.

3.4.2 Scanning Electron Microscope (SEM)

Scanning electron microscopy (SEM) is a microscopy technique that is based on the use of a beam of highly accelerated electrons focused on the surface of a material, thus creating the image. It is very different from techniques of optical microscopy, where the source is the visible light. SEM allows to have detailed and high-quality images with a spatial resolution of $1\ nm$.

Once primary electrons, coming from the beam source, have been scattered on the surface of the sample, they interact with the material atoms at different depths and, as a consequence, various types of signals are produced: secondary electrons, backscattered electrons and X-rays. Secondary electrons signals are managed to derive information about sample surface, morphology, size and topography; while backscattered electrons and X-ray come from deeper regions inside the sample and so they allow to have information about its composition. SEM instrumentation is constituted by different components.

- Sample holder where the stub, on top of which is fixed the sample to analyse, is contained. When using SEM, the samples have to be electrically conductive to avoid overcharging problems which

may introduce extreme brightness and poor images. Thus, non-conductive samples, like polymers, have to be sputter coated with a thin layer of metal (i.e. gold or platinum) which readily reflects electrons and provides a conductive surface for electrons.

- Electron gun provides the electron beam, constituting the emission source that can be of two different types: a thermionic or a field emitter. In the first case, a filament made up of tungsten and lanthanum hexaboride is heated up using electrical current, until the work function of the filament is overcome and electrons can escape from it. In the second case, the heating process is avoided because there is the use of a sharply pointed tungsten wire with a high electric field applied near its tip. In this way, a sufficient electrical potential gradient is generated so that electrons are emitted from the filament. The velocity at which electrons move into the column is determined by the beam energy. A voltage between $1 - 30\ kV$, called the accelerating voltage, is applied to the gun and increases beam energy. The higher is the accelerating voltage, the faster the electrons travel down the column and the higher the penetrating power.
- Column consists of condensed lenses, scanning coils, stigmator coils, objective lenses and apertures that focus the electron beam onto the surface of the specimen. The electron beam is held within a vacuum inside the column and travels along the column towards the sample.
- Detector is able to collect secondary electrons, backscattered electrons and X-rays coming from the interaction between electron beam and sample. The signals are gathered by such detectors and then are manipulated by the computer to form the required image.
- Computer and display to view the images.

The sputter coater used is a 208HR High Resolution Sputter Coater (Cressington) and a gold layer of $7\ nm$ is deposited above the sample. The SEM used to characterize NPs morphology is a Carl Zeiss Ultraplus Field Emission Scanning Electron Microscopy. The accelerating voltage stays in the range between $10 - 20\ kV$, with in-lens detector, collecting mostly secondary electrons.

3.4.3 Confocal Microscopy

In confocal microscopy a beam of incoming light (excitation beam) is focused through the microscope objective on a small spot inside the specimen. Differently from conventional fluorescence microscopy, in which also large unfocused background parts are detected, a small pinhole aperture is used. In this way, only the light emitting from the desired focal spot passes through the pinhole. Any light outside the focal plane is blocked by the screen. A sensitive light detector, such as a photomultiplier tube, on the other side of the pinhole is used to detect the confocal light. To create an image of the specimen, the focal spot is rapidly and serially scanned in the x-y plane. As the scanning proceeds, signal from the detector is fed to a computer that collects and reconstructs the image pixel by pixel. Since the sample is not actually sectioned, a series of confocal planes can be stacked together to obtain tomographic images. Fluorescence microscopy is generally much more

sensitive than light microscopy. Fluorophores that specifically target and identify subcellular structures such as the cytoplasm, sarcoplasmic reticulum, nuclei and mitochondria are available. The excitation light in fluorescence microscopy is provided by a laser at a wavelength that will also excite a specific fluorophore.

3.4.4 Minispec and ICP-MS

The Minispec is a benchtop Nuclear Magnetic Resonance (NMR) analyser for detection of hydrogen (^{1}H), fluorine (^{19}F), and other abundant NMR-active nuclei. Minispec uses a permanent magnetic field and radio frequency (RF) energy to look at NMR sensitive nuclei. In response, RF signals are generated by the sensitive nuclei and the signals are detected by the Minispec. The amplitude and duration of these signals are related to the properties of the sample. T_1 relaxation times, in this work, are measured on a Bruker Minispec (mq60) with a frequency of 60 MHz and a magnetic field of 1,41T. Acquisitions are performed at 37° and T_1 relaxation times are determined using standard inversion-recovery pulse sequence. Inversion recovery pulse sequences are a type of MRI sequence used to selectively null the signal for certain tissues (e.g. fat or fluid). Basically, an inversion recovery (IR) pulse sequence is a spin echo pulse sequence preceded by a 180° RF pulse.

- Sample preparation: 300 μL of NPs (ethanol or water solution) are loaded into glass Minispec tubes. The tubes are placed in a heated bath for 10 minutes to bring the sample at 37°; the measurement is started and T_1 relaxation times are computed.

Inductively Coupled Plasma Mass Spectroscopy (ICP-MS) is an instrument suited for trace metal analysis; it's very sensitive and allows to determine metallic substance concentrations even at very low amounts, such as parts per billion (ppb). Liquid samples are first nebulised in the sample introduction system, creating a fine aerosol that is subsequently transferred to the argon plasma. The high-temperature plasma atomises and ionises the sample, generating ions which are then extracted through the interface region and into a set of electrostatic lenses called the ion optics. The ion optics focuses and guides the ion beam into the quadrupole mass analyser. The mass analyser separates ions according to their mass-charge ratio (m/z) and these ions are measured at the detector. Upon exiting the mass spectrometer, ions strike the detector. The impact of the ions releases a cascade of electrons, which are amplified until they become a measurable pulse. The software compares the intensities of the measured pulses to those from standards, which make up the calibration curve, to determine the concentration of the element. Induced Coupled Plasma (ICP-MS) -NexION 350 by Perkin Elmer is used in this work.

- Sample preparation: first of all, a series of standards at known concentration of the metal to detect are prepared, including a "blank" which contains no measurable amounts of the element of interest. In this

way a calibration curve can be prepared. On the basis of the calibration curve, the instrument is capable of determining metal concentration inside the sample. At this point, $200\ \mu L$ of water NPs solution are diluted in $50\ mL$ of water ($dilution\ factor = 250$); the measurement is started and the concentration of Gd-DTPA inside nanoparticles can be determined. Such concentration values determined by ICP-MS analysis are used in order to determine NPs Gd-DTPA encapsulation efficiency and, when compared with the ones by Minispec analysis, to determine relaxivity boosting due to the entrapment of contrast agent inside the HA hydrogel.

3.4.5 Spectrofluorimetry

Fluorescence spectrometry or Spectrofluorimetry is a technique employed to detect and analyse fluorescence in a sample. A beam of light, usually ultraviolet light, hits the sample and excites the electron in some specific molecules (i.e. fluorophores) which move from their ground state (low energy state) to higher energy excited state. In the ground state, the fluorophore is in a stable configuration and it doesn't fluoresce. When light from an external source hits a fluorophore molecule, the molecule can absorb energy and, if the energy is sufficient, the molecule reaches the excited state. Since the fluorophore is unstable at high-energy configurations, it eventually comes back to the ground state and the excess energy is emitted as light. When the electrons fall back to their ground state they emit photons and, so, fluorescence. The emitted light is of lower energy, and thus longer wavelength, than the absorbed light. Emission of light returns the fluorophore to its ground state. An excitation and emission wavelength have to be properly chosen depending on the element analysed. Fluorescence intensity is directly correlated to the concentration of a specific element inside the sample.
EnSpire Multimode Plate Reader PerkinElmer was used to quantify ATTO 633 and Sulforhodamine.

4 Results

4.1 PLGA microparticles optimization by microfluidics

A feasibility study, reported in *Figure 15*, was conducted in order to evaluate the flow regimes that guarantee a stable production of PLGA microparticles. Side flow rate was changed in the range $2 - 80\ \mu L/min$, while middle flow rate was changed in the range $1 - 10\ \mu L/min$. Some flow regimes conditions determined a jetting regime or an unstable droplet generation, which was not leading to a proper droplet production. Microscope observations were made by collecting the sample at the outlet tube, before the start of the precipitation phase and are reported for each of the production process parameters investigated.

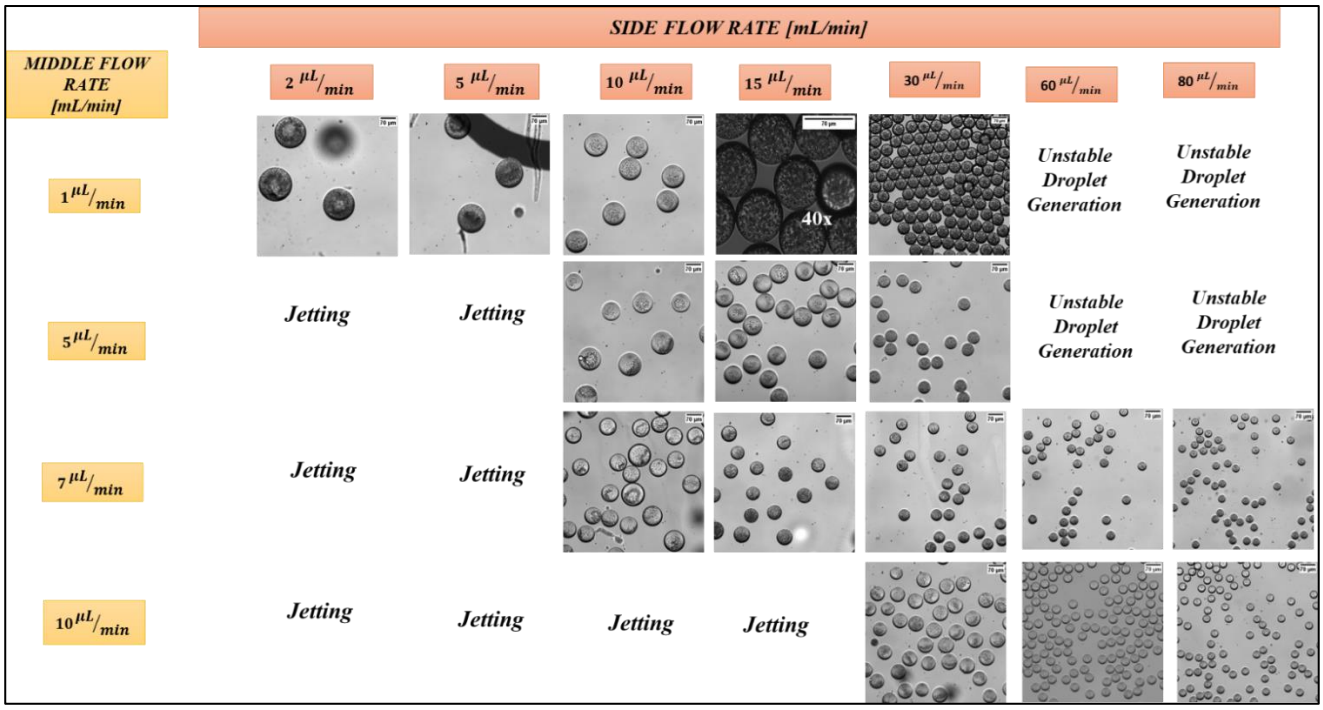

Figure 15 *– Feasibility Study for PLGA microparticle production*

As it is possible to observe from *Figure 15*, the increase of both the middle and side flow rates led to a reduction of the diameter of collected microparticles, while increasing the production regime. This is confirmed by the graphs reported in *Figure 16 a* and in *Figure 16 b*, in which the diameter of the droplet inside the chip and immediately collected at the outlet tube decreased, increasing both the side and middle flow rate.

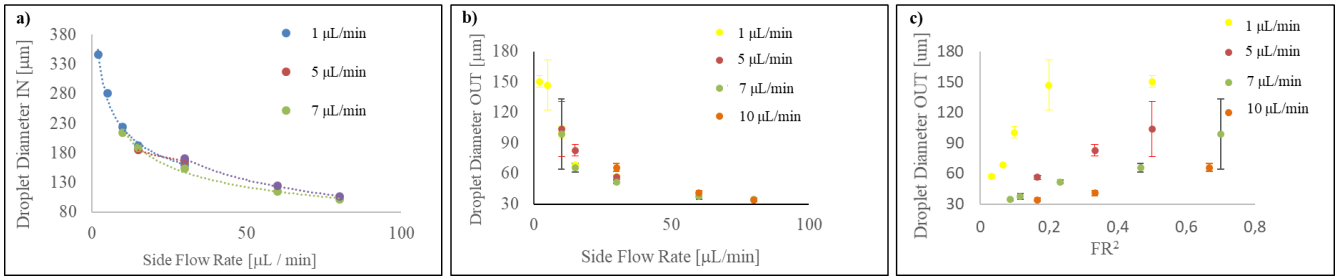

Figure 16 – *a) Diameter of the droplet within the X-junction chip as function of the side flow rate; b) Diameter of the microparticles outside the chip as function of the side flow rate; c) Diameter of the microparticles as function of the flow rate ratio (FR^2)*

On the other hand, from *Figure 17 a* it can be asserted that a reduction in droplet size both inside and outside the chip led to an increase in Generation Rate of the microparticles.

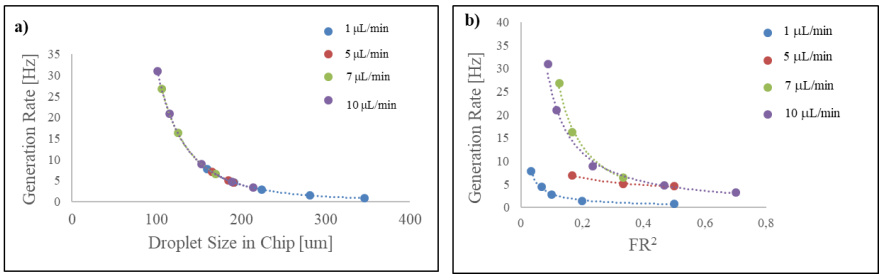

Figure 17 – *a) Generation rate vs Droplet size in chip; b) Generation rate vs* FR^2

SEM observations are performed to understand the precipitation of microparticles, once collected from the outlet tube. To this purpose, the analysis is performed at different time points, while the collected sample was kept in stirring on the wheel and SEM observation are reported in *Figure 18*.

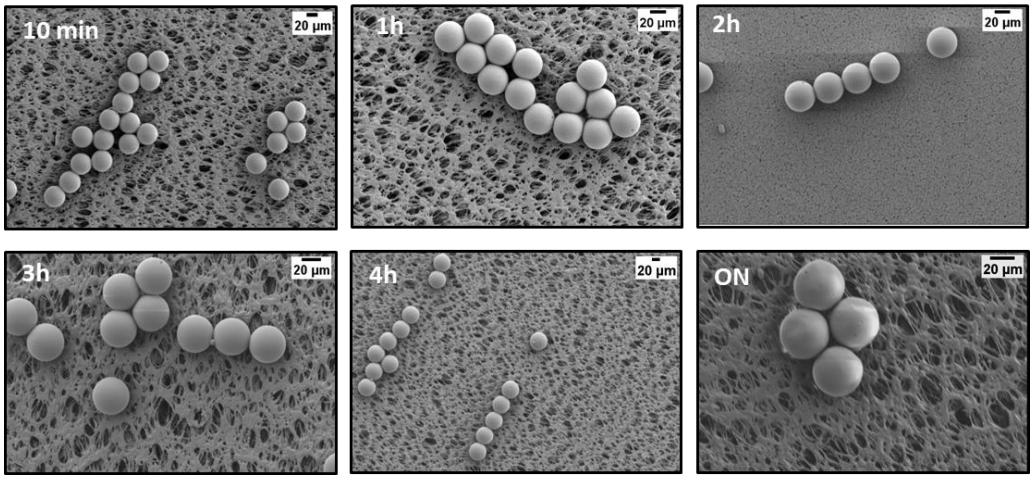

Figure 18 *– precipitation analysis of microparticles by SEM observation with a 1:20 diluition at different time points collection during wheel stirring*

Even after $36h$ post precipitation, microparticles were retaining their shape and structural stability, as it can be observed in *Figure 19.*

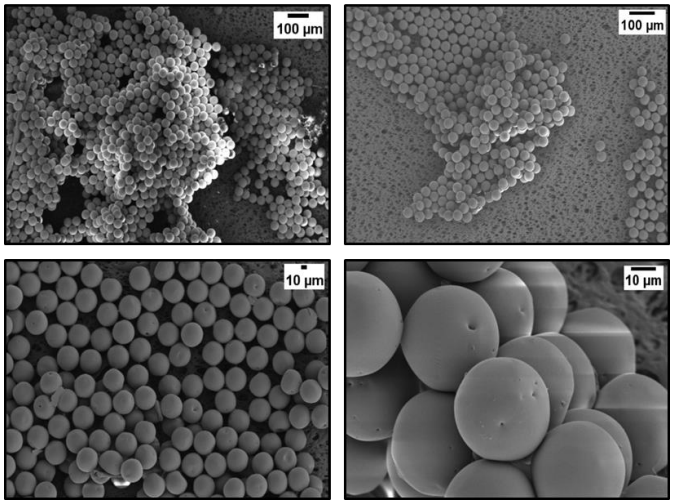

Figure 19 – *SEM observation of microparticles' structure at 36h post precipitation (without diluition)*

A further step was the evaluation of a different PLGA polymer concentration on the final size of the microparticles. This can be observed in *Figure 20*, where diminishing of the PLGA polymer concentration from 5% w/v to 2,5% w/v leads to a decrease both in the diameter of the droplet observed inside the chip and of the microparticle after precipitation.

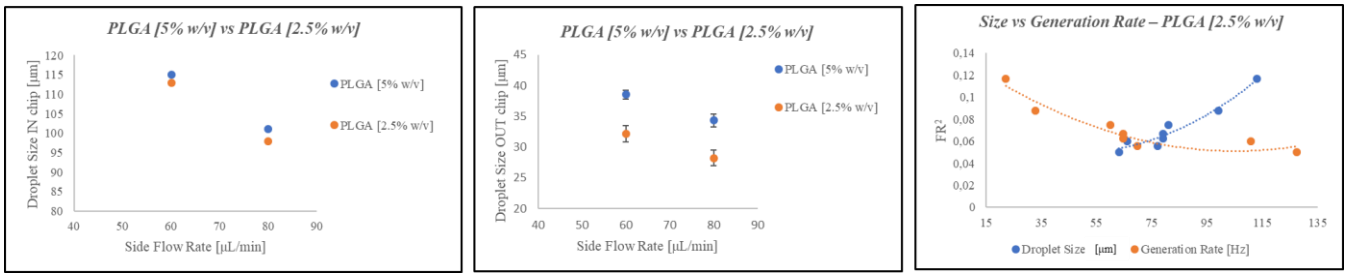

Figure 20 *– effect of different PLGA polymer concentration: 5% vs 2.5% PLGA concentration*

Finally, by using a PLGA concentration of 2.5% w/v, setting the middle flow rate at 5 $^{\mu L}/_{min}$ and side flow rate at 100 $^{\mu L}/_{min}$ and collecting for 70 min, it is possible to achieve the minimum microparticle diameter for the process conditions explored of 16.5 μm as shown in *Figure 21*.

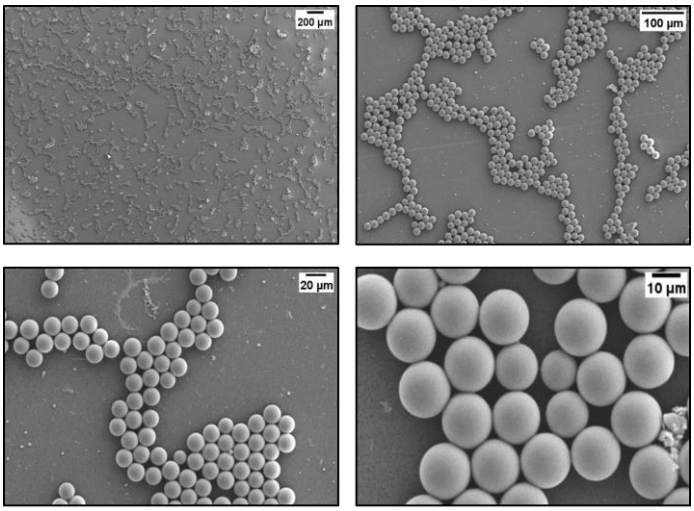

Figure 21 *– SEM observation of microparticles of minimum diameter achieved* (16.5 *µm)*

Preliminary results on the encapsulation of sulforhodamine yielded very low encapsulation efficiency (<4%), but they also demonstrated that the addition of water within the production process led to a change in the internal structure of the microparticles (as depicted in *Figure 22 b*). This alteration may have a significant impact on the release kinetics properties of the DDS.

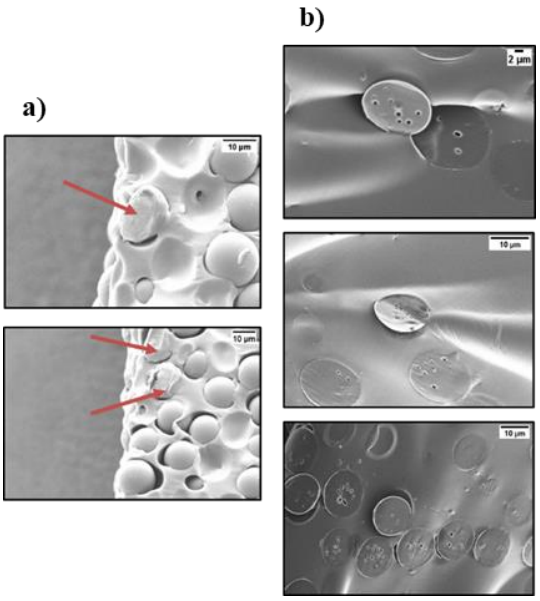

Figure 22 *– internal microparticles' structure: a) no encapsulation leads to smooth external surface and compact internal surface; b) encapsulation of sulforhodamine with water added to the continuous phase*

4.2 cHANPs optimization by microfluidics

cHANPs production is a patented and consolidated process[39, 69], in particular regarding the encapsulation of the contrast agent Gd-DTPA with the well-established and discussed hydrodenticity effect. In this context studies about Flow Rate Ratio, DVS and polymer concentration are performed.

4.2.1 Flow Rate Ratio and DVS concentration

A study about Flow Rate Ratio is conducted, starting from the gold standard condition previously defined[39, 69]. 3 different set of FR^2 are chosen and outcoming results are analysed. In *Figure 23*, results are reported regarding nanoparticles encapsulating Gd-DTPA:

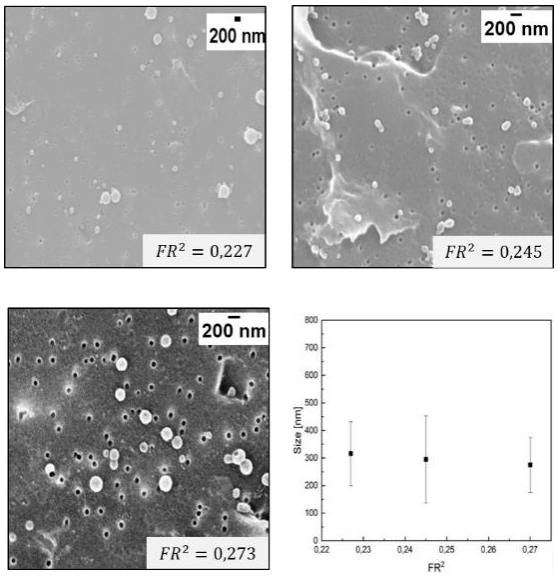

Figure 23 - Gd-DTPA loaded cHANPs at different FR^2: a) 0,227; b) 0,245; c) 0,273; d) DLS measurement of nanoparticles size with respect to FR^2.

The 3 different FR^2 are obtained with a constant flow rate for the lateral channels equal to 110 $\mu L/_{min}$ and varying the one of the central channel; it has been imposed equal to 25 $\mu L/_{min}$, to set FR^2 at 0.227, equal to 27 $\mu L/_{min}$, to set FR^2 at 0.245 and, finally, equal to 30 $\mu L/_{min}$ to set FR^2 at 0.273.

As it can be observed, in the first case, by setting FR^2 equal to 0.227, very polydisperse nanoparticles are produced probably due to the instability of the flow-focusing determined by a too low middle channel flow rate with respect to the lateral ones. By setting FR^2 equal to 0.273, monodisperse nanoparticles are obtained with dimension $> 100\ nm$. Finally, the best condition about FR^2 has been determined by setting this value to 0.245. In this case monodisperse nanoparticles with a mean dimension lower than $100\ nm$ are obtained. Even though DLS measurement reports a mean dimension around $300\ nm$, SEM images show a size of $79.21 \pm 23.44\ nm$ for the considered flow rate ratio of 0.273. This can be explained, first of all, considering that DLS

measures the hydrodynamic diameter of nanoparticles in solution, so it considers also the solvent hydration layer formed around nanoparticles which contributes to their diffusion; especially in the case of hydrogels, water absorption around nanoparticles may be significant. Secondly, the presence of nanoparticles aggregate in solution may determine a much higher nanoparticles size measurement with respect to SEM images. In SEM images, on the other hand, nanoparticles are observed in dried condition, providing information only about the polymer core. Regarding the discordance in the nanoparticles size measure in DLS with respect to SEM images, several adjustments in the DLS protocol may be introduced: for example, a surfactant may be added to the nanoparticles solution to avoid their aggregation or a higher dilution factor may be applied to have a better quality of the measurement. A study about DVS concentration is, then, conducted. Two different DVS concentrations are chosen: $4M$ and $8M$. Adjusting DVS concentration allows to modulate the crosslinking degree and density of polymeric meshes, analysing the effect of DVS on relaxivity boosting of nanoparticles. The results are reported in *Figure 24* regarding cHANPs encapsulating Gd-DTPA.

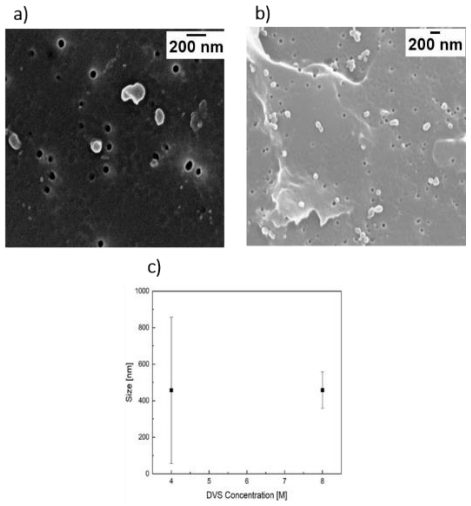

Figure 24 *- Gd-DTPA loaded cHANPs at different DVS concentration: a) 8M DVS concentration; b) 4M DVS concentration; c) DLS measurement of nanoparticles size with respect to DVS concentration.*

As it can be observed by *Figure 24 a*, nanoparticles obtained with a higher DVS concentration are characterized by a distorted morphology, a mean dimension higher than the requested one and, with respect to the dehydrated condition in ethanol, they show significant swelling and aggregation phenomena in water. In *Figure 25* DLS measurements with double DVS concentration are reported, with nanoparticle solution in acetone and in ethanol; as it can be observed, in the passage from acetone to ethanol, the average dimension of nanoparticles enlarges up to $400\ nm$.

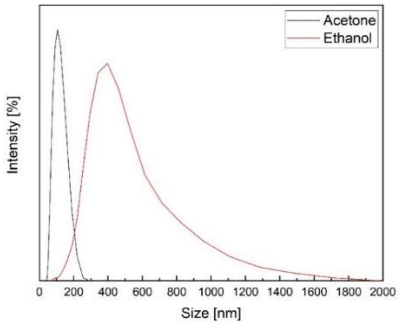

Figure 25 - DLS measurements of cHANPs produced with double DVS concentration in acetone and ethanol

Furthermore, the high DVS concentration may induce the formation of a too much cross-linked nanostructure which has a significant impact on the hydrodenticity effect: actually, the relaxivity boosting, in this case, is drastically reduced and lower than 2 times. Russo et al. reported that increase in cross-linking density is associated with a decrease in water content and diffusion inside the polymeric matrix. Lowering in water content decreases osmotic pressure inside the water compartments of the meshes, determining a reduction in hydration status of Gd-DTPA which could limits the enhancement of the relaxometric properties in the nanostructure. On the other hand, decreased water diffusion may imply a too slow water exchange between the inner and outer sphere water molecules, so that the relaxation effect is poorly transmitted to the bulk and relaxometric properties are consequently limited[39].

4.2.2 Gd-DTPA and ATTO633 co-encapsulation

In order to obtain cHANPs for multimodal imaging purposes, several active agents are encapsulated inside them together with Gd-DTPA. In the first case, ATTO633 is chosen as fluorophore for multimodal imaging and encapsulated with Gd-DTPA. Two different initial concentration of ATTO633, 10 $^{\mu g}/_{mL}$ and 20 $^{\mu g}/_{mL}$, are explored setting the $FR^2 = 0.245$ and $DVS = 4M$, which can be defined as standard flow conditions; the aim is to increase fluorophore encapsulation inside nanoparticles. Increasing initial ATTO633 concentration does not affect nanoprecipitation process and allows to encapsulate a higher amount of fluorophore, since in both cases ATTO633 encapsulation efficiency, evaluated through spectrofluorometer, is around 15%. The optimization of ATTO633 encapsulation inside cHANPs is necessary in order to make clear confocal visualization of nanoparticles (*Figure 26 b*) and, possibly, in vitro and in vivo study to evaluate their accumulation. Nanoparticles morphology is reported in *Figure 26 a* and DLS size distribution, compared to cHANPs encapsulating only Gd-DTPA, in *Figure 26 c*. In order to observe nanoparticle distribution at confocal microscope, high dilution factors, up to 1:1000, are exploited. In this way, visualization of single nanoparticles rather than aggregates is made possible, reducing the background noise caused by large aggregates of nanoparticles which could give a wide fluorescence signal.

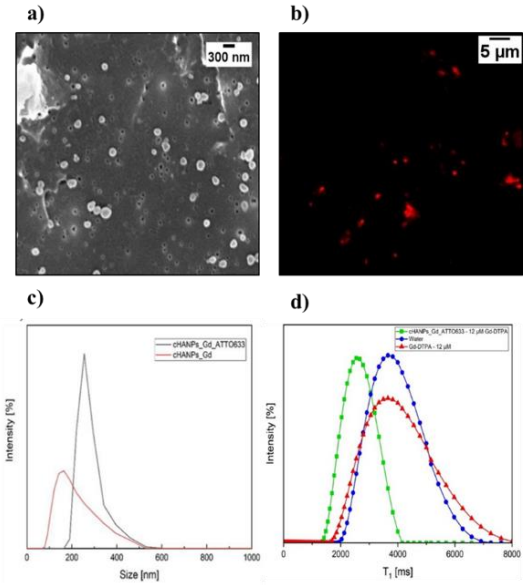

Figure 26 *- Gd-DTPA and ATTO633 loaded cHANPs a) SEM image; b) confocal image; c) effect of fluorophore encapsulation on NPs dimension*

Concerning Gd-DTPA encapsulation, Minispec and ICP-MS analysis have been performed, to evaluate relaxivity boosting. In *Figure 26 d*, results regarding Minispec and ICP-MS are reported; they show a net increase in relaxivity both with respect to pure water and to the amount of Gd-DTPA effectively encapsulated inside nanoparticles (i.e. 12 μM in the case reported). This means that, thanks to the hydrodenticity effect, it is possible to achieve a lower T_1 relaxation time, which implies a better image contrast, with less amount of Gd-DTPA. This aspect is really important since it is possible to improve magnetic resonance image quality, by using lower amounts of contrast agents and, thus, reducing possible side effects related to confirmed toxicity and accumulation issues of Gadolinium-based contrast agents.

4.3 Scale-up of cHANPs production

TELOS® System has been selected with the purpose to scale at an industrial level the consolidated and patented production process of cHANPs, since to be clinically relevant nanoparticles have to be produced in high doses and with very low batch-to-batch and intra-batch variability.

In this set of experiment, two Telos® modules have been used, with 14 X-junctions run at the same time. The flow rate of the central channels (i.e. of the solvent solution constituted by: $water, Hyaluronic\ Acid\ and\ active\ agents$) can be imposed without the necessity of a calibration curve, due to the presence of a flow rate sensor. The flow rate imposed is equal to 14 times the desired one at the junction, since 14 X-junctions and 14 central channels composing these last ones are present. As it can be appreciated from the chip geometry (*Figure 27 a*), instead, two different inlets which feed two separate channels are dedicated to the water flow, but, at the junction, these channels are joined into a single one. On the other hand, differently, the flow rate of the side solution (i.e. of the non-solvent solution constituted by:

$acetone\ and\ Divinyl\ Sulfone\ (DVS)\ as\ cross-linking\ agent$) imposed is equal to 28 times the desired one at the junction, due to the presence of two separate side channels at each X-junction. In this case, the flow rate cannot be imposed directly, since no flow sensor is used on the acetone pump, but a pressure value has to be set. The pressure which allows to guarantee the desired flow rate is determined based on a calibration curve: at a fixed time-interval and with a known flow rate set for the water pump, specific values of pressure for the acetone pump are imposed; the collected volume, at which the known flown water volume is subtracted, is measured, making possible to derive the non-solvent flow rate correspondent to that pressure. Collection in $10\ mL$ of acetone is performed separately for the two chips.

Visual observation of the stability of the flow focusing in the different chips' junctions allowed to set the flow rate of the central channel to $100\ \mu L/min$ and the pressure of the side channel to $150\ mbar$, in order to achieve a flow rate ratio (FRR) of 0.245, which has been previously shown to guarantee the best process conditions for cHANPs production on a lab-scale microfluidic device, keeping concentration of Hyaluronic Acid to $0.05\%\ w/v$, concentration of Gd-DTPA to $0.1\%\ w/v$, concentration of NaOH to $0.75\%\ V/V$ and DVS concentration to $4\%\ V/V$. Nanoparticles produced on TELOS® with the process conditions above described, show, as it can be observed in *Figure 27 b* and in *Figure 27 c*, reporting Scanning Electron Microscopy (SEM) and Nanoparticle Tracking Analysis (NTA) respectively, slight polydispersity, with a mode dimension, derived from NTA analysis, that is around $200\ nm$. As a next step, $ATTO633$ ($20\ \mu g/mL$) has been encapsulated in nanoparticles. As it can be observed from *Figure 27 d*, nanoparticles, at confocal observation, retain their spherical shape proving the encapsulation of the dye inside them. However, spectrofluorometer analysis shows a quite low encapsulation efficiency for the dye, around $3\% - 6\%$ for nanoparticles produced from chip1 (the closest to the TELOS® inlets) and chip2, respectively. Minispec and ICP-MS analysis have been, then, performed, to evaluate relaxivity boosting. cHANPs produced with the process conditions above described do not show relaxivity boosting, probably due to a too high rigidity of the polymeric meshes of the nanoparticles, which can be explained by the mixing conditions, due to TELOS® chip geometry (*Figure 26 a*), which completely change from lab-scale platform to pilot system device. To increase relaxivity boosting, then, attempts to reduce cross-linking agent concentration have been performed. In particular, DVS concentration has been reduced to $1\%\ V/V$, keeping all the other process conditions equal; this allows to increase relaxivity boosting up to 3.5 times. However, further experimental campaign needs to be performed to improve relaxivity boosting, by trying different DVS concentrations and/or reducing Gd-DTPA concentration, to reduce nanoparticles' polydispersity, by trying different flow rate ratios, and to increase the encapsulation efficiency of active agents.

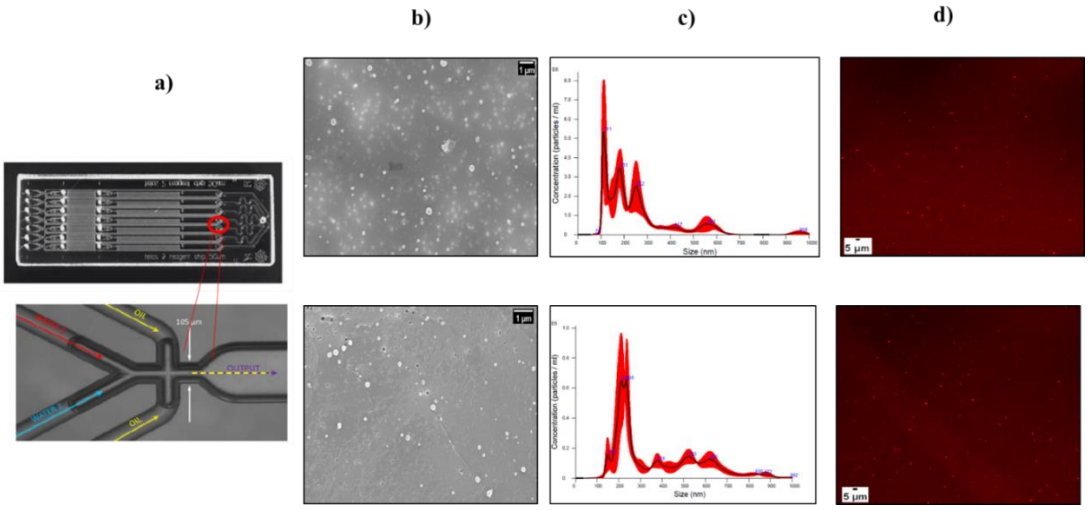

Figure 27 *– Preliminary results about cHANPs production through Telos® system: a) Telos®2 Reagent Chip with junction geometry and flow path; b) SEM analysis; c) NTA Analysis; d) Confocal Microscope Analysis. Top line in b),c),d) represents cHANPs collected from chip1 /the closest to the inlet), while bottom line represents cHANPs collected from chip2.*

5 Future perspectives

5.2 Microfluidics as a tool to understand and discover nano-bio interactions

Almost daily, new nanoparticles with different architectures and complex designs, i.e. different synthetic identities, are being produced and tested on lab-scale or in pre-clinical and clinical settings, with more than 3000 patents of nanomedicine technology nowadays available [70]. To make numbers clearer, suffice it to say that patented nanoparticles far outnumber the FDA-approved nanoparticle-based drugs for cancer treatment [71, 72]. This makes evident that, despite there is a wide technological knowledge for nanomedicine production (i.e. in terms of composition, size, shape, stiffness, surface charge and decoration), only a small percentage of nanoparticles has been able to reach the clinics (more than a hundred) [72].

This uncontrolled and unsuccessful behavior *in vivo* (i.e. pharmacokinetics and pharmacodynamics) is mainly due to the poor ability to rationalize the nanoparticles physicochemical features with respect to their way of interacting with the barriers at each organ, sub-organ or subcellular level (i.e. biological identity) [6, 73].

Thus, this missing connection between the synthetic and the biological identity of nanoparticles has drastically hindered the precise tuning of their design according to the tumor-related biological, physicochemical and mechanical barriers, which vary intra- and inter- patients and during the progression or regression of the disease [5, 6].

Nowadays, the attention is increasingly shifting towards the comprehension of nano-bio interactions; actually, all the available information about nanoparticles' health and safety associated properties, nano-biological activities (cell uptake, cell viability and ROS production) and production processes is being collected in nanoinformatics datasets (i.e. *caNanoLab, ISA-TAB-Nano, PubVINAS and Nanoparticle Information Library*).

However, the high volume of non-organized data, the complexity and heterogeneity in the data standard of these datasets do not offer an easy tool for data-driven rationalization of nanoparticle design [74, 75]. This pushes the scientific community towards the development of individual sets of experimental data that are specific for each single nano-bio-interaction and are then further processed through artificial intelligence attempting to highlight patterns in the biological behavior of nanoparticles.

As first efforts, *in vitro* cytotoxicity [76, 77], cellular uptake [78] or protein corona composition [79], as function of different nanoparticle characteristics, have been exploited to develop, through artificial intelligence/machine learning (*AI/ML*) algorithms, Quantitative Structure Activity Relationships (*QSARs*) that reveal non-evident links between structural properties of nanoparticles and their biological activity *in vitro*. Notably, *Mirkin et al.*, developed powerful XGBoost model (a ML algorithm), capable of correlating the *in vitro* immune response of macrophages with the structural properties of nanoparticles. In particular, they identify, among a library of 1000 spherical nucleic acids (SNAs), which results from the combination of 11 design parameters, the key parameters that lead to higher levels of immune activation [4].

However, developed models suffer of poor reproducibility and limited applicability since nanoparticles are not produced, manipulated and characterized accurately. The high batch-to-batch and intra-batch variability of NPs produced by conventional batch techniques has, actually, posed a limit to the discovery of nano-bio interfaces, since even slight and minute changes in nanoparticle features may determine radically different behavior *in vitro* and *in vivo* and inconsistent and uncertain biodistribution outcomes [80, 81].

Why not take a step back and exploit microfluidic technology for the discovery of poorly understood nano-bio interactions?

In this scenario, with respect to batch production of nanoparticles, microfluidics has proven to be a valuable and disruptive tool in producing large libraries of nanoparticles, each one of them with slightly different, unique, very well defined and controlled properties. The high reliability in nanoparticles' features allows to discern the effect of each single design property on the resulting nano-bio interactions, identifying and selecting optimal sizes and size distributions for cellular uptake [36, 82-86], optimal release profiles for anticancer efficacy [86, 87], optimal ligand-surface functionalization for cell uptake [26, 51, 88, 89] and optimal nano-vector rigidity for cellular uptake and viability [55, 90]. In this perspective, microfluidics offers the possibility to acquire knowledge about the **one-to-one relationships** between the specific synthetic identity of NPs and the triggered nano-bio-interactions.

Why and how to choose the optimal nano-vector for a specific pathology and clinical stage?

Moving to personalized medicine, this awareness should be adapted or re-shaped according to the complexity and heterogeneity, not reproducible *in vitro*, of the biological characteristics of each individual. Actually, it has to be taken into account that, in an *in vivo* complex tumor microenvironment, nano-bio interactions occur at the interface of each biological barriers; these barriers are extremely heterogeneous intra- and inter- patients and their anatomical, mechanical and fluido-dynamic properties change by the stage of the disease and the

pathophysiology of the patient [6], impacting on the final biological outcome of the nanoparticles, in terms of their pharmacokinetics and pharmacodynamics [73, 91, 92]

In this sense, *Karageorgis et al.* found that tumor microvasculature structure and permeability parameters, derived by Magnetic Resonance Imaging (MRI) clinical characterization *(in particular by means of Dynamic Contrast-Enhanced and Vessel Index MRI*), as a function of tumor stage and variability among different types of mice models, hugely impact on the accumulation of the same type of lipidic nanocapsules [2].

Similarly, *Sykes et al.* histologically characterized different-sized mice tumor (from low to high tumor volume due to the progression of the disease), in terms of increased vascular density, cell density and extracellular matrix content, and associated these parameters to the ability of the tumor to accumulate PEGylated gold nanoparticles of different sizes.

Why not explore clinical data and move the attention towards their rationalization and organization, to provide a rational design of nanoparticles?

Every day **2.3 trillion gigabytes** of data and information are collected from patients by different techniques (as conventional tests, omics-based medicine, next-generation sequencing and clinical imaging) [93]; however, they have not been really exploited to characterize patient-specific biological barriers and consequently guide the optimal design of nanoparticles in a personalized medicine perspective.

In conclusion, we propose a paradigm shift in the conception of nanoparticle design by microfluidics, paving the way to a disease/patient driven approach. Once the complex interplay between synthetic and biological identity of nanoparticles has been highlighted by the microfluidics-driven development of models, clinical and quantitative characterization of tumor microenvironment and barriers can guide and inform the optimal design of nanoparticles, with each property finely tuned to achieve the desired nano-bio interactions. Among all the techniques for nanoparticles' production, microfluidics is noteworthy for reliable production processes offering the molecule by molecule on the final architecture and functionality of the nanoparticles.

But, are we getting the most by microfluidics?

The rapidity and scalability of nanoparticles' production offered by microfluidics and the possibility to combine on the same microfluidic chip different stages for production, purification [94] and sterilization [95], offer the possibility, in the next future, of providing ready-to-use and injectable nanoparticle formulations. Indeed, in the wake of the recent progresses in the field of microfluidic-driven production of radioisotopes (i.e. *Advion NanoTek*), through which it is possible to decentralize the radioisotope production from the cyclotron directly to the radiopharmacies and allow the radiopharmacist to produce, on the microfluidic device, a single and on-demand dose of personalized tracers for each patient [96, 97], we foresee microfluidics as a tool to implement the

production of nanoparticles directly in the hospital, with optimal design selection provided directly by the real-time characterization (in the hospital) of the patient-related tumor parameters.

Chapter 3 - *the role of clinical imaging in personalized medicine and nanomedicine: the case study of PET image reconstruction*

Some parts of this chapter are taken from a published paper: ***Cece et al., Spatio-temporal Positron Emission Tomography Reconstruction with Attenuation and Motion Correction, MDPI Journal of Imaging[98].***

1 Background

1.1 Basic physical principles of PET

Positron Emission Tomography (PET) is a medical imaging technique that reconstructs the 3D metabolic activity of body cells, allowing to discern between tumour and normal tissues. In most of the tumours the rate of glucose uptake is much higher with respect to normal tissues. Therefore, PET imaging commonly employs an analogue of 2-deoxyglucose (DG) labelled with a positron-emitting isotope (18F), resulting in FDG, to visualize tumor cells. A positron has the same mass, but opposite charge with respect to an electron. When positrons emitted from the isotope interact with the electrons in the surrounding tissue, they gradually lose their energy. Eventually, the energy of the positron become sufficiently small and a collision with a free electron in the tissue results in a matter-antimatter annihilation. This annihilation produces two 511 keV γ photons that emerge in opposite direction, at 180° from each other, as represented in *Figure 28*. When the photons are detected from PET scanner detectors placed in opposite direction, the millions of recorded coincidence events form the basis for PET image formation [99, 100].

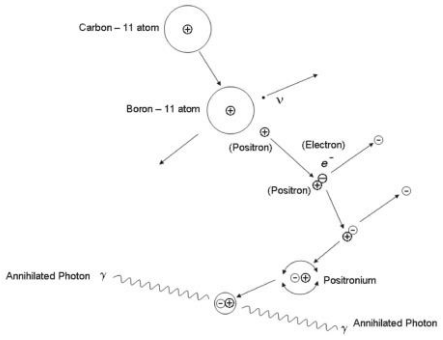

Figure 28 *– schematics of positron annihilation (from [100])*

1.1.1 Data Acquisition

The Line of Response (LOR) is the *tube* that connects two individual scintillator crystal in a block-type PET detector scanner as reported in *Figure 29*.

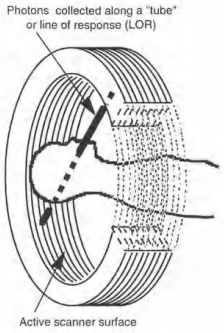

Figure 29 *– multi-ring PET scanner showing a single LOR intersecting the patient in the field of view*

In absence of attenuation, scatter and random events, the number of coincidence events recorded along a LOR is proportional to the integral of the tracer concentration along the LOR. More precisely, the sum of coincidence events is a realization of a random distribution according to a Probability Density Function (PDF), which is usually assumed to be Poisson distributed[99]:

$$E\left[\sum_{LOR}(events)\right] = c\int_{LOR} f(x)dx \qquad (Eq.4)$$

After 100000 or more annihilation events are recorded, radiotracer distribution is computed through tomographic reconstruction approaches from the recorded projection data:

$$P = e^{-\int a(x)dx}\int f(x)dx \qquad (Eq.5)$$

where P is the projection data, $a(x)$ is the linear attenuation coefficient for $511 - keV\ \gamma - rays$ and $f(x)$ is the radiotracer distribution. The exponential factor considers the attenuation of the two $\gamma - rays$ inside the patient's body. Scattering is, on the other hand, not taken in consideration in the *Eq. 5*. After attenuation and scattering correction are performed, the reconstructed image gives a quantitative measure of the radiotracer distribution.

PET imaging can be performed with or without incorporating information about the time it takes for γ photons emitted during positron annihilation to be detected (*i.e.*, Time-of-Flight or ToF information). It is known that including ToF information can improve the overall performance of PET scans.

In a standard PET system, when positron annihilation occurs, it is assumed to be somewhere along a Line of Response (LoR), but there is no precise information about the exact interaction point. Annihilation events along this LoR are considered to be uniformly distributed, which introduces noise into the resulting image. In contrast, ToF-PET makes use of the time difference (Δt) between the detection of the gamma photon pairs that

travel in opposite directions. This time difference is correlated to a specific position (Δx) along the LoR where the annihilation occurred:

$$\Delta x = c\frac{\Delta t}{2} \qquad \text{(Eq. 6)}$$

By analyzing this time difference (Δt), it is possible to estimate the exact location of the annihilation event. This localization improves the Signal-to-Noise Ratio (SNR) in the final PET image. The difference between conventional and ToF-PET can be seen in *Figure 30*[101].

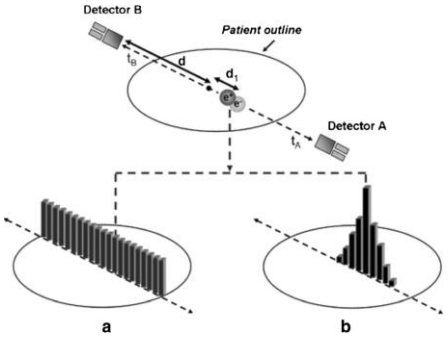

Figure 30 *– difference between conventional PET and ToF-PET*

1.2 Main Tomographic Reconstruction Algorithms

Projection data are usually reconstructed with the *filtered backprojection algorithm*.
In this case, the process of PET reconstruction is linear and performed through successive operations on the projection data P:

$$f = \sum_{\vartheta} BPF^{-1}[\mathcal{R}F(f)] \qquad \text{(Eq. 7)}$$

where f is the image, F is the Fourier transform, $\mathcal{R}$ is the ramp-shaped high pass filter, BP is the backprojection algorithm. Another class of reconstruction algorithm involve iterative solutions to the classic inverse problem

$$P = Af \qquad \text{(Eq. 8)}$$

where P is the projection matrix, f is the matrix of the true image data and A is the projection operator. The inverse,$f = A^{-1}P$, is computed by iteratively estimating the data f' and modifying the estimate by comparison of the calculated projection set P' to the true observed projections P.
The expectation maximization (EM) algorithm solves the inverse problem by updating each pixel value f_i in accord with:

$$f_i^{k+1} = \sum_j p_j \frac{f_i^k a_{ij}}{\sum_{i'} f_{i'}^k a_{i'j}} \qquad \text{(Eq. 9)}$$

where p is the measured projection data, a_{ij} is the probability that a source at pixel i will be detected in projection detector j, and k is the iteration.

1.3 Artifacts in PET image reconstruction: motion and attenuation derived artifacts

Artifacts commonly observed in PET image reconstruction primarily arise from various sources, including respiratory and cardiac motion, as well as the absence of accurate attenuation correction.

Figure 31 shows, as an example, an inconsistency in the positioning of the diaphragm between PET and CT scans due to respiratory motion, which often results in the occurrence of a visible artifact known as a "cold artifact" at the lung base. Numerous studies have documented significant misalignments between CT and PET data.

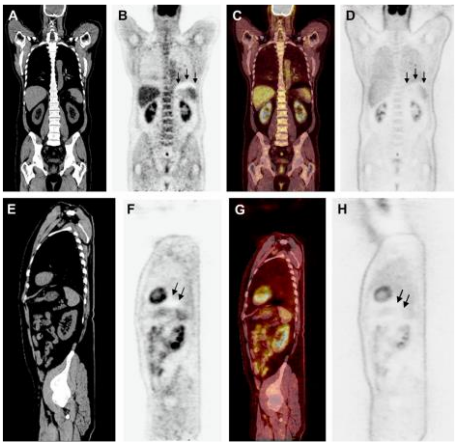

Figure 31 *- Illustration of a respiratory motion related artifacts on positron emission tomography (PET) images reconstructed with CT-based attenuation correction.*

Figure 32, on the other hand, shows typical reconstruction artifacts for a uniform distribution of activity in a cylindrical phantom, resulting in the depression of activity in the middle of the object.

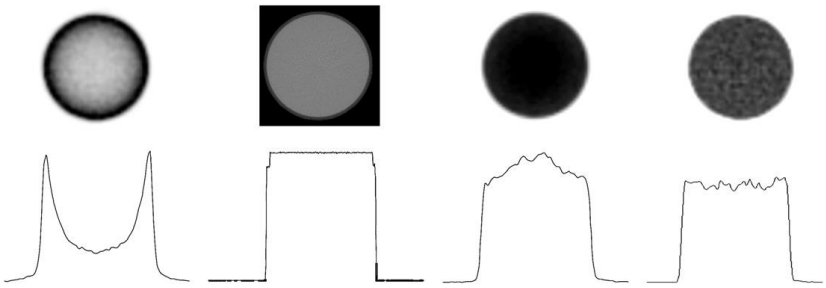

Figure 32 *- From left to right: reconstructed image without attenuation correction, the CT-based attenuation map, the same slice after applying attenuation correction but without scatter correction, and finally the same slice after applying attenuation and scatter corrections.*

2 Aim of the work

The detection of early-lung cancer lesions of size comparable to that of system resolution is a long-standing problem in Positron Emission Tomography (PET). In this chapter, we propose two algorithms which jointly correct for patient motion and attenuation, by investigating the effect of composing an image-registering convolutional network with the modeling of the static data acquisition (*i.e.*, the forward model). Their performance is evaluated on synthetic data mimicking small pulmonary lesions. The commonly used figure of merits Peak Signal to Noise Ratio (PSNR), Recovery Coefficient (RC) and Signal Difference to Noise Ratio (SDNR) give incoherent results, whereas visual inspection and a Channelized Hotelling Observer suggests that the proposed algorithm outperform current clinical practice.

3 Materials and Methods

3.1 non-ToF and ToF MLAA algorithms

In this paragraph, the equations for the implementation of the non-TOF and TOF-MLAA algorithm are reported.

3.1.1 non-TOF MLAA implementation

For the non-TOF implementation of the MLAA algorithm, we have used the equations from paper [102]. By defining f the reconstruction of the activity distribution, μ the reconstruction of the attenuation map, A as the forward operator, y the projection data acquired, a the attenuation factors, α and N as two parameters to be set, the update for activity and attenuation reconstruction are reported following, considering no scatter or random events:

$$\boldsymbol{Activity\ update}: f^{k+1} = \frac{f^k}{A^{-1}a} A^{-T} \frac{y}{Af^k}$$

$$\boldsymbol{Attenuation\ update}: \mu^{k+1} = \mu^k + \frac{\alpha}{N}\left(1 - \frac{A^{-T}y}{A^{-T}[aAf^{k+1}]}\right)$$

3.1.2 ToF-MLAA algorithm implementation

MLAA algorithm provides iterative updates for activity and attenuation reconstruction. The equations are implemented from paper[103].

Considering that:

$$a_i^h = e^{-\sum_j l_{ij}\mu_j^h}$$

which represents the non-ToF sinogram of the attenuation, computed from the current attenuation map estimation, the equation for the update of the activity, keeping the attenuation constant, is given by the following equation:

$$\lambda_j^{h+1} = \frac{\lambda_j^h}{\sum_{it} a_i^h c_{ijt}} \sum_{it} a_i^h c_{ijt} \frac{y_{it}}{\sum_\zeta a_i^h c_{i\zeta t}\lambda_\zeta^h + s_{it}} \qquad \text{(Eq. 10)}$$

The previous equation, *Eq. 10*, is the Maximum Likelihood Expectation Maximization (MLEM) algorithm for TOF data. Once the activity is updated, it is kept constant to update the attenuation map reconstruction, through the following equation:

$$\psi_i^h = a_i^h \sum_{jt} c_{ijt}\lambda_j^{h+1} \qquad \text{(Eq. 11)}$$

Eq. 11 is the non-TOF sinogram that represents the expected TOF - integrated count for LOR i, but without the additive contribution of the scatter, s_i. Activity is kept constant and the attenuation is updated through the Maximum Likelihood Transmission (MLTR) algorithm for TOF-integrated counts:

$$\mu_j^{h+1} = \mu_j^h + \frac{\sum_i l_{ij} \frac{\psi_i^h}{\psi_i^h + s_i}(\psi_i^h - y_i + s_i)}{\sum_i l_{ij} \frac{(\psi_i^h)^2}{\psi_i^h + s_i} \sum_\zeta l_{i\zeta}} \qquad \text{(Eq. 12)}$$

In *Eq. 12* the term $\sum_\zeta l_{i\zeta}$ represents the diameter of the transaxial field of view.

3.1.3 Wrapping between SIRF and ODL operators

To exploit the flexibility of the Operator Discretization Library (ODL), a Python wrapping between the forward and backward operators of the ODL library and of the ToF-branch of the Synergistic Image Reconstruction Framework (SIRF) has been implemented and reported in the following scripts. ODL works by approximating and discretizing forward and backward operators in a discrete, numerical form.

```
class ForwardProjectorByBinWrapper(Operator):

    """A forward projector using STIR.

    Uses "ForwardProjectorByBinUsingProjMatrixByBin" as a projector.
    """

    def __init__(self, acquisition_data, image, adjoint=None):
        """Initialize a new instance.

        Parameters
        ----------
        domain : `DiscreteLp`
            Volume of the projection. Needs to have the same shape as
            ``volume.shape()``.
        range : `DiscreteLp`
            Projection space. Needs to have the same shape as
            ``proj_data.to_array().shape()``.
        volume : ``stir.FloatVoxelsOnCartesianGrid``
            Stir volume to use in the forward projection
        proj_data : ``stir.ProjData``
            Stir description of the projection.
        projector : ``stir.ForwardProjectorByBin``, optional
            A pre-initialized projector.
        adjoint : `BackProjectorByBinWrapper`, optional
            A pre-initialized adjoint.
        """
        # Check data sizes


        image = pet.ImageData(acquisition_data)
        self.image = image
        am = pet.AcquisitionModelUsingRayTracingMatrix()
        am.set_up(acquisition_data,image)

        self.forward= am.forward

      image_array = image.as_array()

      domain = odl.discr.uniform_discr(min_pt=np.zeros(np.ndim(image_array)),
                      max_pt=np.ones(np.ndim(image_array)),
                  shape=image_array.shape)

      codomain = odl.discr.uniform_discr(
  min_pt=np.zeros(len(acquisition_data.dimensions())),
  max_pt=np.ones(len(acquisition_data.dimensions())),
      shape=acquisition_data.dimensions())


      if adjoint is None:
          self._adjoint = BackwardProjectorByBinWrapper(acquisition_data, image, adjoint=self)
      else:
          self._adjoint = adjoint


      # Set domain, range etc
      super().__init__(domain=domain, range=codomain, linear=True)


  def _call(self, volume, out):
      """Forward project a volume."""
      # Set volume data
      self.image.fill(volume.asarray())

      out[:] = self.forward(self.image).as_array()

  @property
  def adjoint(self):
      """Back-projector associated with this operator."""
      return self._adjoint
```

```
class BackwardProjectorByBinWrapper(Operator):

    """A backward projector using STIR.

    Uses "ForwardProjectorByBinUsingProjMatrixByBin" as a projector.
    """

    def __init__(self, acquisition_data, image, adjoint=None):
        """Initialize a new instance.

        Parameters
        ----------
        domain : `DiscreteLp`
            Volume of the projection. Needs to have the same shape as
            ``volume.shape()``.
        range : `DiscreteLp`
            Projection space. Needs to have the same shape as
            ``proj_data.to_array().shape()``.
        volume : ``stir.FloatVoxelsOnCartesianGrid``
            Stir volume to use in the forward projection
        proj_data : ``stir.ProjData``
            Stir description of the projection.
        projector : ``stir.ForwardProjectorByBin``, optional
            A pre-initialized projector.
        adjoint : `BackProjectorByBinWrapper`, optional
            A pre-initialized adjoint.
        """
        # Check data sizes


        image = pet.ImageData(acquisition_data)
        self.image = image
        self.data = acquisition_data
        am = pet.AcquisitionModelUsingRayTracingMatrix()
        am.set_up(acquisition_data,image)

        self.backward= am.backward
        # backward_TOF=am.backward

        image_array = image.as_array()

    codomain = odl.discr.uniform_discr(min_pt=np.zeros(np.ndim(image_array)),
                    max_pt=np.ones(np.ndim(image_array)),
                shape=image_array.shape)


    domain = odl.discr.uniform_discr(
min_pt=np.zeros(len(acquisition_data.dimensions())),
max_pt=np.ones(len(acquisition_data.dimensions())),
    shape=acquisition_data.dimensions())


    if adjoint is None:
        self._adjoint = ForwardProjectorByBinWrapper(acquisition_data, image, self)
    else:
        self._adjoint = adjoint


    # Set domain, range etc
    super().__init__(domain=domain, range=codomain, linear=True)


def _call(self, volume, out):
    """Backward project a volume."""
    # Set volume data
    self.data.fill(volume.asarray())

    out[:] = self.backward(self.data).as_array()

# @property
def adjoint(self):
    """Back-projector associated with this operator."""
    return self._adjoint
```

3.2 Proposed algorithms

In the following, the algorithm proposed in [104] is extended to 3D and the attenuation correction of the projections is included in the reconstruction in two different ways. The case of gated sinogram data, with $N + 1$ gates $g_0, \ldots, g_N$, in each of which the patient is assumed to be stationary, was considered. The corresponding images of the activity distribution will be denoted by $f_0, \ldots, f_N$ and the relative attenuation maps by $\mu_0, \ldots, \mu_N$, whereas the attenuation map obtained from an X-ray CT scan will be indicated by μ_{CT}. Data acquisition is modelled by a forward operator, A, such that:

$$A f_j e^{-A\mu_j} = g_j \qquad \text{(Eq. 13)}$$

Eq. 13 refers to the expectation values of f_j and g_j, which are both, in fact, Poisson-distributed random variables.

Finally, let W_j be the registration action between gates f_j and f_{j+1}:

$$f_j = W_j f_{j+1} \qquad \text{(Eq. 14)}$$

and A_j is defined as the composition of the forward operator with the registration action: $A_j \equiv A \circ W_j$, so that $A_j f_{j+1} e^{-A\mu_{j+1}} = g_j$. Disregarding the effect of attenuation, the reconstruction of all data in the reference gate, f_0, can be performed using the Morphed-Maximum Likelihood Expectation Maximisation, M-MLEM, introduced in[104] and reported hereafter:

Algorithm 1 M-MLEM algorithm

Require: $n \geq 0$
Require: $m \geq 0$
Require: $N \geq 1$
$A \leftarrow A$ ▷ Radon transform
$A^* \leftarrow A^*$ ▷ adjoint operator of Radon transform
$\theta \leftarrow \theta$ ▷ learned parameters of Synthmorph network
$n \leftarrow MLEM_{iter}$ ▷ nb of MLEM iterations
$m \leftarrow MMLEM_{iter}$ ▷ nb of M-MLEM iterations
$N \leftarrow nb_{gates} + 1$ ▷ nb total of gates
$f_0, \ldots, f_N \leftarrow 1 \ldots 1$ ▷ init of the distribution estimation
$g_0, \cdots, g_N$ ▷ data for every gates
$W_0, \ldots, W_N \leftarrow Id, \ldots, Id$ ▷ Init registration fields
for $i \leftarrow 0, N$ **do**
  for $k \leftarrow 1, n$ **do**
    $f_i \leftarrow f_i \frac{A^* g_i}{A f_i^k A^* 1}$ ▷ MLEM iteration
  end for
  if $i > 0$ **then**
    $W_{i,i-1} \leftarrow H(f_{i-1}, f_i, \theta)$ ▷ vector field between two close gates
    $W_{i-1,i} \leftarrow -W_{i,i-1}$ ▷ approximate estimation of inverse
    $W_i \leftarrow W_{i,i-1} \circ \ldots \circ W_{1,0}$
    $W_i^{-1} \leftarrow W_{0,1} \circ \ldots \circ W_{i-1,i}$
  end if
end for
for $k \leftarrow 1, m$ **do**
  $f_0 \leftarrow \frac{\sum_{j=1}^{N} A_{j-1}^* \left[\frac{g_j}{A_j(f_0^k)} \right]}{\sum_{j=1}^{N} A_{j-1}^* 1} f_0 \frac{\sum_{j=0}^{N} |\det D\varphi_j| \left(A^T \frac{g_j}{A(f_0 \circ \varphi_j^{-1})} \right) \circ \varphi_j}{\sum_{j=0}^{N} |\det D\varphi_j| \left(A^T 1 \right) \circ \varphi_j}$ ▷ M-MLEM iteration
end for

3.2.1 M-MLEM + CT

The first algorithm proposed here performs the attenuation correction by deforming the CT-based attenuation map, μ_{CT}, to the reference gate and will be called Morphed Maximum Likelihood Expectation Maximisation with CT-based attenuation map ($MLEM + CT$) in the remainder of the chapter. The activity distribution is updated as reported in Algorithm 2, where μ_{CT-0} denotes the CT-based attenuation map after it has been morphed to the reference gate.

Algorithm 2 M-MLEM + CT algorithm

Require: $n \geq 0$
Require: $m \geq 0$
Require: $p \geq 0$
Require: $N \geq 1$
$A \leftarrow A$ ▷ Radon transform
$A^* \leftarrow A^*$ ▷ adjoint operator of Radon transform
$\theta \leftarrow \theta$ ▷ learned parameters of Synthmorph network
$m \leftarrow MLAA_{iter}$ ▷ nb of MLAA iterations
$p \leftarrow MMLEM_{iter}$ ▷ nb of M-MLEM iterations
$N \leftarrow nb_{gates} + 1$ ▷ nb total of gates
$f_0, \ldots, f_N \leftarrow 1 \ldots 1$ ▷ init of the distribution estimation
$g_0, \ldots, g_N$ ▷ data for every gates
$W_0, \ldots, W_N \leftarrow Id, \ldots, Id$ ▷ init registration fields
for $k \leftarrow 0, m$ **do**
$f_0^{k+1} \leftarrow f_0^k \frac{A^*\left[e^{-A(\mu_0^k)} \frac{g_0}{[e^{-A(\mu_0^k)} A(f_0^k)]}\right]}{A^*[1 \cdot e^{-A(\mu_0^k)}]}$ ▷ MLAA iteration - MLEM step
$\mu_0^{k+1} \leftarrow \mu_0^k + \frac{A^*[e^{-A(\mu_0^k)} A(f_0^k)]}{A^*[e^{-A(\mu_0^k)} \cdot A(1)]}$ ▷ MLAA iteration - MLTR step
$W_{CT,0} \leftarrow H(\mu_0, \mu_{CT}, \theta)$ ▷ vector field between CT attenuation map and μ_0
$W_{0,CT} \leftarrow -W_{CT,0}$ ▷ approximate estimation of inverse
$\mu_{CT-0} \leftarrow W_{CT,0}(\mu_0)$ ▷ attenuation map deformed in gate0
for $i \leftarrow 0, N$ **do**
for $k \leftarrow 1, n$ **do**
$f_i^{k+1} \leftarrow f_i^k \frac{A^*\left[e^{-A(\mu_i^k)} \frac{g_i}{[e^{-A(\mu_i^k)} A(f_i^k)]}\right]}{A^*[1 \cdot e^{-A(\mu_i^k)}]}$ ▷ MLAA iteration: MLEM step
$\mu_i^{k+1} \leftarrow \mu_i^k + \frac{A^*[e^{-A(\mu_i^k)} A(f_i^k)]}{A^*[e^{-A(\mu_i^k)} \cdot A(1)]}$ ▷ MLAA iteration: MLTR step
end for
if $i > 0$ **then**
$W_{i,i-1} \leftarrow H(f_{i-1}, f_i, \theta)$ ▷ vector field between two close gates
$W_{i,i-1} \leftarrow H(\mu_{i-1}, \mu_i, \theta)$ ▷ vector field between two close gates
$W_{i-1,i} \leftarrow -W_{i,i-1}$ ▷ approximate estimation of inverse
$W_i \leftarrow W_{i,i-1} \circ \ldots \circ W_{1,0}$
$W_i^{-1} \leftarrow W_{0,1} \circ \ldots \circ W_{i-1,i}$
end if
end for
for $k \leftarrow 1, p$ **do**
$f_0 \leftarrow f_0^k \frac{\sum_{j=1}^N A_{j-1}^* \left[e^{-A_j(\mu_{CT-0})} \frac{g_j}{e^{-A_j(\mu_{CT-0})} A_j(f_0^k)}\right]}{\sum_{j=1}^N A_{j-1}^*[1 \cdot e^{-A_j(\mu_{CT-0})}]} f_0 \frac{\sum_{j=0}^N |\det D\varphi_j| \left(A^T \frac{g_j}{A(f_0 \circ \varphi_j^{-1})}\right) \circ \varphi_j}{\sum_{j=0}^N |\det D\varphi_j| (A^T 1) \circ \varphi_j}$ ▷ M-MLEM iteration
end for

3.2.2 M-MLAA

The second proposed algorithm will be called the Morphed Maximum Likelihood Activity and Attenuation (*M-MLAA*). It follows the interleaved updates of activity distribution and attenuation map as in its original version[103], but the forward and backward operators are composed with the registration fields evaluated by Synthmorph, as described in Paragraph 3.2. The two update steps will be, consequently, called $M-MLEM$ and $M-MLTR$ and are reported in Algorithm 3.

Algorithm 3 M-MLAA

Require: $n \geq 0$
Require: $m \geq 0$
Require: $N \geq 1$
$A \leftarrow A$ ▷ Radon transform
$A^* \leftarrow A^*$ ▷ adjoint operator of Radon transform
$\theta \leftarrow \theta$ ▷ learned parameters of Synthmorph network
$m \leftarrow MLAA_{iter}$ ▷ nb of MLAA iterations
$p \leftarrow MMLEM_{iter}$ ▷ nb of M-MLAA iterations
$N \leftarrow nb_{gates} + 1$ ▷ nb total of gates
$f_0, \dots, f_N \leftarrow 1 \dots 1$ ▷ init of the distribution estimation
$g_0, \dots, g_N$ ▷ data for every gates
$W_0, \dots, W_N \leftarrow Id, \dots, Id$ ▷ init registration fields
for $i \leftarrow 0, N$ **do**
  for $k \leftarrow 1, n$ **do**

$$f_i^{k+1} \leftarrow f_i^k \frac{A^*\left[e^{-A(\mu_i^k)} \frac{g_i}{[e^{-A(\mu_i^k)} A(f_i^k)]}\right]}{A^*[1 \cdot e^{-A(\mu_i^k)}]}$$ ▷ MLAA iteration: MLEM step

$$\mu_i^{k+1} \leftarrow \mu_i^k + \frac{A^*[e^{-A(\mu_i^k)} A(f_i^k)]}{A^*[e^{-A(\mu_i^k)} \cdot A(1)]}$$ ▷ MLAA iteration: MLTR step

  end for
  if $i > 0$ **then**
    $W_{i,i-1} \leftarrow H(f_{i-1}, f_i, \theta)$ ▷ vector field between two close gates
    $W_{i,i-1} \leftarrow H(\mu_{i-1}, \mu_i, \theta)$ ▷ vector field between two close gates
    $W_{i-1,i} \leftarrow -W_{i,i-1}$ ▷ approximate estimation of inverse
    $W_i \leftarrow W_{i,i-1} \circ \dots \circ W_{1,0}$
    $W_i^{-1} \leftarrow W_{0,1} \circ \dots \circ W_{i-1,i}$
  end if
end for
for $k \leftarrow 1, m$ **do**

$$f_0 \leftarrow f_0^k \frac{\sum_{j=1}^N A_{j-1}^* \left[e^{-A_j(\mu_{CT-0})} \frac{g_j}{e^{-A_j(\mu_{CT-0})} A_j(f_0^k)}\right]}{\sum_{j=1}^N A_{j-1}^*[1 \cdot e^{-A_j(\mu_{CT-0})}]} f_0 \frac{\sum_{j=0}^N |\det D\varphi_j| \left(A^T \frac{g_j}{A(f_0 \circ \varphi_j^{-1})}\right) \circ \varphi_j}{\sum_{j=0}^N |\det D\varphi_j| \left(A^T 1\right) \circ \varphi_j}$$ ▷ MMLAA iteration: MMLEM step

$$\mu_0^{k+1} \leftarrow \mu_0^k + \frac{\sum_{j=1}^N A_{j-1}^*[e^{-A_j(\mu_0^k)} A_j(f_0^k)]}{\sum_{j=1}^N A_{j-1}^*[e^{-A_j(\mu_0^k)} \cdot A_j(1)]}$$ ▷ MMLAA iteration: MMLTR step

end for=0

3.3 Implementation of the Algorithms

Forward and backward operators are implemented from the Time of Flight (ToF) branch of the Synergistic Image Reconstruction Framework (SIRF) library[105], and are wrapped in the Operator Discretization Library (ODL) (Available online: https://github.com/odlgroup/odl) in which all the algorithms are implemented. The

operators are defined according to the geometry of the Siemens mCT scanner. Registration fields are computed using the pre-trained convolutional neural network Synthmorph. Synthmorph is trained on synthetic, semantic segmented images and provides modality-agnostic and contrast-invariant registration. Registration fields, W_j, registering f_j and f_{j+1}, are computed from images obtained with two initial MLAA iterations. Inverse diffeomorphisms, W_j^{-1}, are computed by first order approximation of W_j, as: $-W_j(\cdot)$. For both approaches, two sets of diffeomorphisms for the activity distributions and the attenuation map are evaluated. In order to enhance Synthmorph registration performances, the attenuation map reconstructions are segmented to remove the artifacts in the region of the field of view not covered by the object. These artifacts are commonly seen whenever applying MLTR-MLAA update[106]. For $M - MLEM + CT$, Synthmorph is further deployed as a first step in the registration of the CT-based attenuation map, μ_{CT}, to the reconstruction of the reference gate, f_0, obtained after the same number of initial MLAA iterations.

3.4 Generation of Synthetic Data

In order to assess the performance of the proposed algorithms synthetic projection data has been generated from the digital 4D extended cardiac-torso XCAT phantom[107], in which five lesions have been added. The voxel size of the generated XCAT phantom is $0,316 \times 0,316 \times 0,16\ cm^3$ and four respiratory and cardiac gates have been used in this study. The proximity to real respiratory and cardiac motion of the XCAT phantoms is ensured by the fact that they were obtained from X-ray CT and Magnetic Resonance measurements of healthy male volunteers. In particular, 4D tagged Magnetic Resonance Imaging data and 4D high-resolution respiratory-gated CT data, are used [107]. The size, relative uptake and positioning of the lesions have been carefully chosen. The size is almost the same for all of the lesions and comparable to system resolution. Their position is shown in Figure 1, two lesions are localized in slice 55, two lesions in slice 65 and one lesion in slice 80. The rationale for their positioning is described in the following. One of the lesions is placed in the upper part of the lungs, this should be the easiest one to detect as respiratory motion is lower in that region. Two of them are placed in proximity to the hearth, which has a high uptake through the blood pool, and are therefore expected to have a lower contrast compared to their surroundings. The remaining two lesions are placed around the middle of the lungs, one on each side. Uptake is chosen to be either 4:1 or 6:1 compared to the blood pool, reflecting typical standard uptake values in fluorodeoxyglucose PET.

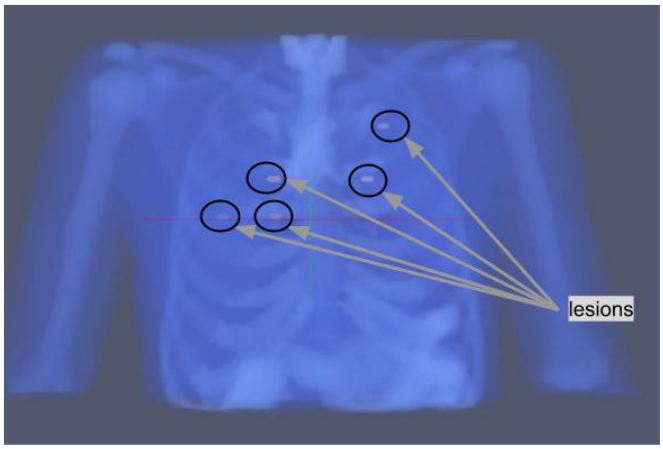

Figure 33 *- Position of the five lung lesions in the XCAT phantoms*

From the labels in the XCAT phantom, a radiotracer distribution and an attenuation map have been estimated in the way described in the following:

- **Radiotracer distribution**: Uptake for healthy tissues has been taken from [108]with an educated guess for tissues not present in the reference. The activity in has been scaled to a level consistent to the dose injected at Karolinska Hospital in Huddinge (3 MBq/kg up to a max of 400 MBq total). The scaling has been done considering a mass of 70 kg for the full-body XCAT-phantom and by setting the average uptake 158 per voxel to be equal to the total injected dose divided by the number of voxels in the XCAT-phantom. Lungs uptake is considered to be 0,75 of the average uptakes and the scaling factors for remaining organs are derived from table 2 in [108] by dividing the median activity concentration in the organ (column 2) by the median activity of lungs divided by 0,75. The five lesions were given an activity corresponding to 4 or 6 times that of the blood pool. One of the lesions in slice 55 has a dimension of 6×5 voxels whereas the other is 6×4, the lesions in slice 80 and 65 are all 6×5 voxels in dimension[108].
- **Attenuation map**: The attenuation map has been estimated from the labels of the XCAT using the values from the National Institute of Standards and Technology tables. Since at the energy of interest most human tissues have similar attenuation, apart from bone and lung tissues, we only used the x different value for the linear attenuation coefficients reported in Table 9.

Tissue/material	Linear attenuation coefficient (cm^{-1})
air	0
lung tissue	0,01
bladder	0,05
liver	0,08
cartilage	0,15
bone	0,17
remaining tissues	0,1

Table 9 *- Linear attenuation coefficients used for obtaining an attenuation map at 511 keV from the XCAT phantom labels*

Once the activity distribution and the attenuation map have been created, attenuated sinograms are generated with forward projection and Poisson noise is added.

3.5 Hardware and Software

The hardware used is an Intel(R) Xeon(R) CPU E5-2690 v3 @ 2.60GHz with one GPU from the ASPEED Graphics Family, with 500 Gigabyte memory and 8 Terabyte hard disk. All computations are run in Python 3.7.4, using TOF capabilities of the Synergistic Image Reconstruction Framework (SIRF 3.4) library and the Operator Discretization Library (ODL 178 0.7.0). Voxelmorph 0.2 and Tensorflow 2.11.0 are used for Synthmorph registration.

3.6 Evaluation of M-MLAA and M-MLEM + CT reconstruction algorithms

$M-MLAA$ and $M-MLEM+CT$ reconstructions have been compared against:

- MLAA reconstruction of reference gate, f_0; this corresponds to the situation in which a large amount of projection data is thrown away in order to avoid motion blurring (called in the remainder *Single-gate MLAA*);
- MLAA reconstruction from the sum of the data in all of the four gates; this corresponds to disregarding motion correction (called in the remainder *Total-gate MLAA*);
- MLAA single-gate reconstructions summed after registration in the reference gate with Synthmorph (called in the remainder *Sum+Synthmorph*);
- MLEM reconstruction of the reference gate, f_0, with attenuation correction performed through CT-derived attenuation map. This corresponds to the most common clinical practice and disregards motion correction (called in the remainder *Clinical Standard MLEM*).

The comparison of the algorithm performances is carried out through the evaluation of chosen Figures of Merit (FOMs) and a Channelized Hotelling Observer (CHO).

3.6.1 Figures of Merits (FOMs)

The FOMs that have been evaluated are: Peak Signal to Noise Ratio (PSNR), Recovery Coefficient (RC) and Signal Difference to Noise Ratio (SDNR). PSNR has been evaluated on the whole reconstructed images with a data range equal to 500; RC and SDNR have been evaluated within Regions of Interest (*i.e.*, ROIs) around

the five lesions in the phantom. With I_1 indicating the phantom, I_2 the reconstructed image from noisy and attenuated sinograms, Ω_l the ROI around the lesion and Ω_b the ROI within the background, the chosen FOMs have been evaluated as follows:

- PSNR:

$$PSNR = 10log_{10}(\frac{d^2}{MSE})$$

  Here, d is the maximum fluctuation in the input image data type and MSE is the Mean Squared Error, computed as follows:

$$MSE = \sum_{M,N} \frac{[I_1(m,n) - I_2(m,n)]^2}{M \cdot N}$$

- RC:

$$RC = \frac{\sum_{\Omega_l} I_2}{\sum_{\Omega_l} I_1}$$

- SDNR:

$$SDNR = \frac{\frac{1}{N_{pixel_l}} \sum_{\Omega_l} I_2 - \frac{1}{N_{pixel_b}} \sum_{\Omega_b} I_1}{\sqrt{\sigma(I_1(\Omega_l)) + \sigma(I_1(\Omega_b))}}$$

3.6.2 Channelized Hotelling Observer (CHO)

Model observers are used to assess the quality of medical images with respect to a clinical task of interest, which in our case is a lesion detection task[109, 110]. They function as a powerful surrogate of human performance. The Channelized Hotelling Observer, CHO, belongs to the class of linear model observers, which act by applying a linear template w to the image data vector f to compute a scalar test statistic t as a decision variable, according to:

$$t = \boldsymbol{w}^T \boldsymbol{f}$$

The decision variable is, then, compared against a threshold to determine if the lesion is present ($t > threshold$) or absent ($t < threshold$). By varying the threshold, it is possible to compute the Receiver Operating Characteristic (ROC) Curve and the Area Under the Curve (AUC) and use those to compare the performances of the tested algorithms.[111] The CHO operates through a set of channels, which allow to extract

specific features from the images, as the ones that can be extracted by the human visual system. The outputs of the channels are then linearly combined through the Fisher-Hotelling rule in order to achieve the optimal CHO template. The Fisher-Hotelling rule states that the vector a, containing the best linear combination of the channel weights, is to be computed as follows[112]:

$$\mathbf{a} = \mathbf{K_v}^{-1}[< \mathbf{f_{V/s}} > - < \mathbf{f_{V/b}} >]$$

Here, $\boldsymbol{K_v^{-1}}$ is the covariance matrix of the output of the channels to the images, $< f_{V/s} >$ is the mean signal plus background as seen by each channel and $< f_{V/b} >$ is the mean background only as seen by each channel. The optimal template is, finally, used to compute the test statistic and evaluate ROC and AUC for each of the algorithm tested. In this paper, the CHO is implemented through 4 Gabor filters. Gabor filters have been chosen since they are a validated model to mimic the response of the cells in the visual cortex[111, 112]. The parameters of the Gabor filters have been set to a spatial frequency that varies between 0,01 and 0,02 pixels, orientation that varies between 0, 01 and 0, 05 radians, bandwidth of 0,9 octaves and standard deviation set to 3. Twenty-five ROIs have been considered each with a dimension of 10 × 10 pixels. Five ROIs are evaluated around the lesions of interest and twenty in the background only; they are taken within the slices $55{,}65\ and\ 80$. Before feeding in the CHO and extracting features through the channels, a Gaussian filter with $\sigma = 0.8$ is used to reduce the noise within the reconstructed images.

4 Results

4.1 Non-TOF and TOF implementation of MLAA algorithm

4.1.1 The artifacts of non-TOF implementation of MLAA algorithm

When applying the MLAA algorithm to non-Time-of-Flight (non-ToF) synthetic data, as represented by the simple squared phantoms in *Figure 34 a*, it becomes clear that the choice of initialization for the attenuation map plays a fundamental role on the reconstruction of the activity. Specifically, we explored several initialization options for the attenuation map, including setting it to all zeros, all ones, random values, the mean value, and shifted values. Importantly, the choice of initialization for the attenuation map persists throughout the reconstruction process. This persistence is clearly evident in *Figure 34 c*, where, for instance, selecting a “shifted" attenuation map as the initial condition results in a shifted reconstructed attenuation map. Moreover, regardless of the number of iterations applied in the algorithm, the shifting remains unchanged. This persistence in the attenuation map initialization also impacts on the reconstruction of the activity, leading to artifacts in the activity reconstruction, as illustrated in *Figure 34 c*.

To solve this problem of persistency for the initialization of the attenuation map, further attempts have been made in increasing the number of MLEM iterations before MLTR iterations and viceversa, observing slightly better results in the first situation, as it is possible to observe in *Figure 34 f*, where the behavior of the log-likelihood maximization, varying the chosen number iterations for MLEM and MLTR update, is reported. In particular, best results seem to be obtained by applying, for each algorithm iteration, 3 MLEM updates and 1 MLTR update, with the attenuation map initialized to shifted values. This could be an interesting situation for a real-case scenario, in which the attenuation map can be initialized through a CT from a different gate with respect to the one under consideration. However, it has to be considered that non-TOF MLAA algorithm results to be ill-posed.

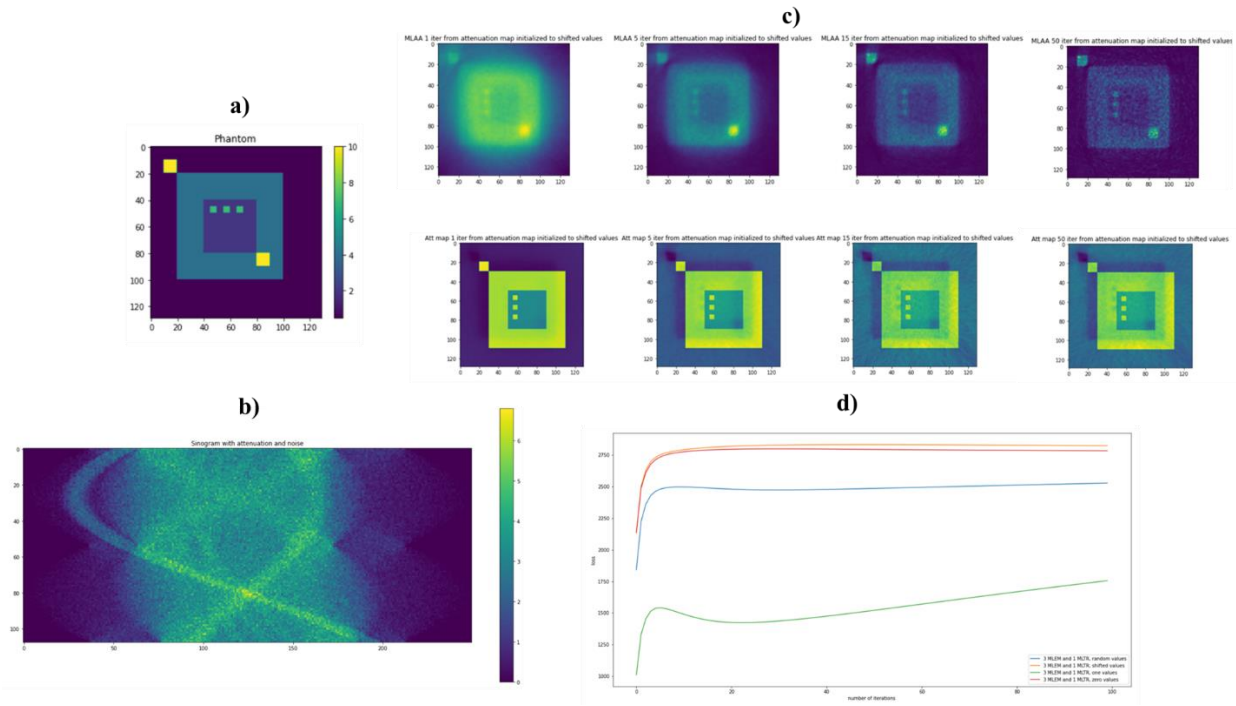

Figure 34 *– non-TOF implementation of MLAA algorithm: a) synthetic non-anthropomorphic phantom; b) correspondent non-TOF sinogram; c) on the top the reconstruction of the activity and on the bottom the reconstruction of the attenuation map; d) evaluation of the loss*

4.2 Evaluation of the proposed algorithms' performance by Visual Inspection

For the purpose of visual inspection, the reconstruction of the entire slices (i.e., 55, 65, and 80) containing the lesions, and the reconstructions of a region of interest around the lesions (with a dimension of 25 × 25 pixels) are reported, for each of the algorithms tested, in *Figure 35* and *Figure 36*, respectively. The number of iterations has been fixed to 50 for all the algorithms, except for Clinical Standard MLEM, which is instead

visualised after 20 iterations and at the same dynamic range as the other algorithms. This choice is dictated by the fact that Clinical Standard MLEM is commonly regularised by early stopping, since it is known that the MLEM reconstructions tend to become noisier after a certain number of iterations[113]. Thus, we have shown the reconstructions from *Clinical Standard MLEM* at the best of the algorithm performance, according to the qualitative assessment of the visibility of the small lesions. In *Figure 36*, a blow-up of the area around the lesions in the different reconstructions is shown. A Gaussian filter with $\sigma = 0.8$ has been applied to reduce the noise of the reconstructions. A visual estimate of the contrast and spatial resolution of the reconstructions, obtained using the different tested algorithms in the area surrounding the lesions, suggests that *Single gate MLAA*, *M-MLAA*, and *M-MLEM + CT* are the best-performing algorithms. *Clinical Standard MLEM* reconstruction of the activity obtained after 20 iterations has a much higher value than the actual value, as well as than any of the other reconstructions. We have chosen to present the reconstruction with the same dynamic range as the others in order to make the comparison somewhat fair. By a visual inspection of *Figures 35 and 36*, we can make different observations regarding the reconstruction of the five lesions. The two lesions in slice 55 are better visually reconstructed in *M-MLEM + CT* and *M-MLAA*, with *single-gate MLAA* being highly noisy and easily leading to the misinterpretation of the artefacts. Blurring from motion can be clearly observed in *Clinical Standard MLEM* and *total gates MLAA*. In slice 65, the lesion that is very close to the heart is not captured by any of the tested algorithms, probably due to the combination of the high uptake in the heart and the cardiac movement. The second lesion in slice 65 seems to be reconstructed better by *M-MLAA* and *M-MLEM + CT*, which both provide better contrast and spatial resolution. The lesion in slice 80 seems, similarly, to be captured better by the *M-MLEM + CT* algorithm. In the following paragraph, instead, we show reconstructions at the iteration number that maximize the chosen figure of merit (see *Figures 37-39*).

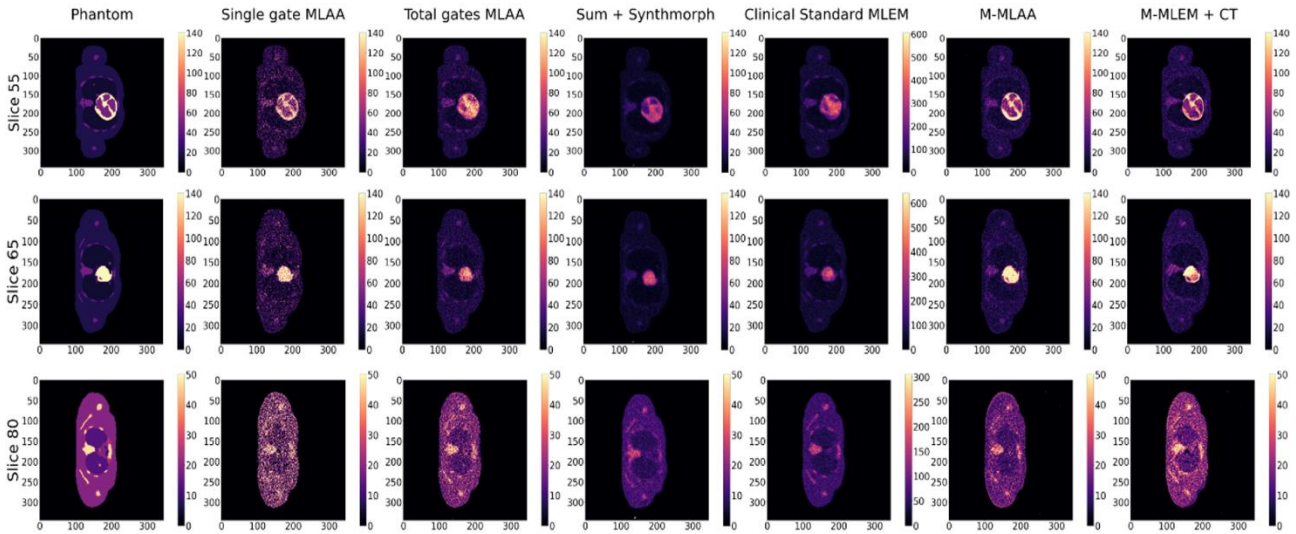

Figure 35 *- Slices 55, 65, and 80 of the XCAT phantom (uttermost left column) and their reconstructions with the different algorithms compared in this work.*

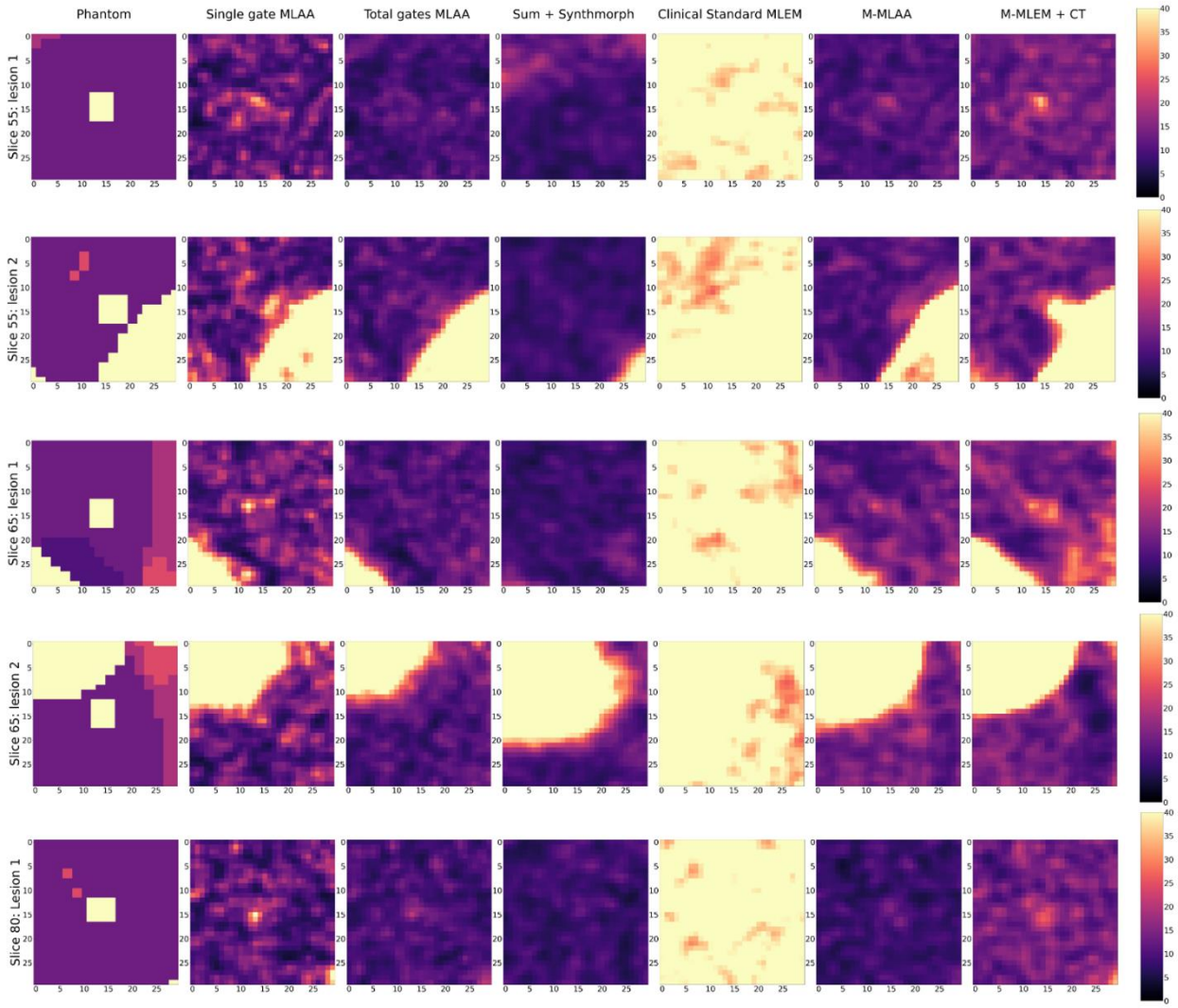

Figure 36 *- Blow-up of a region of interest around the five lung lesions in the XCAT phantom (uttermost left column) and of the same region of interests in the image reconstructed with the different algorithms compared in this work.*

4.3 Evaluation of the proposed algorithms' performance by FOMs and CHO

In *Figures 37-39*, the trends of the FOMs with respect to the number of iterations for each of the tested algorithms are plotted. This allows for determining the optimal number of iterations at which the FOM reaches the maximum value for each of the algorithms under investigation. Entire slices or only the lesions are, afterwards, reconstructed at each of the identified optimal numbers of iterations and reported correspondingly. Finally, to further assess the quality of the reconstructed images, a CHO is implemented. In order to compare the performances of the algorithms, ROC and AUC are plotted for each one of them and reported in Figure 40.

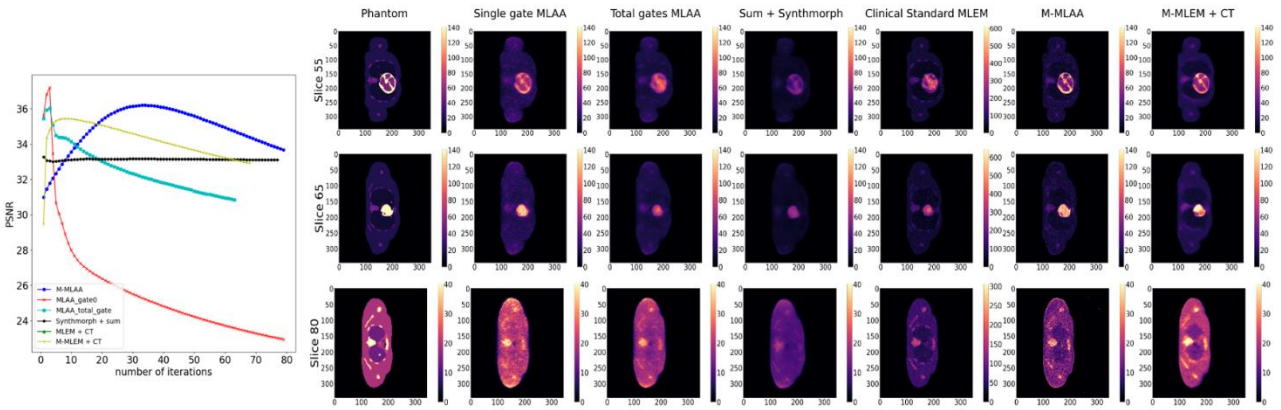

Figure 37 *- PSNR as a function of iteration number (left pane) and reconstruction of chosen slices at the optimal number of iterations for each of the tested algorithms.*

Looking at *Figures 37-39*, it is evident that the response from the chosen FOMs does not correlate with the visual assessment of the lesion visibility and fidelity to the phantom. In *Figure 37*, it is possible to observe that the maximum PSNR values are obtained by the *single-gate MLAA* after only a few iterations. However, the corresponding image seems to be of inferior quality compared to both *M-MLEM + CT* and *M-MLAA* at their best PSNR value, which is obtained for a larger number of iterations. Similarly, in *Figure 38*, the RC value for each of the algorithms as a function of the number of iterations is shown together with the corresponding reconstructions of an ROI around the lesions at the optimal number of iterations. For all lesions, RC favours single gate MLAA and total-gate MLAA. However, this does not seem to be the case when looking at the corresponding reconstructions. Finally, SDNR *(Figure39)* shows rather inconsistent behaviour over the different lesions, making it difficult to establish which algorithm offers the best performance in reconstructing the lesions.

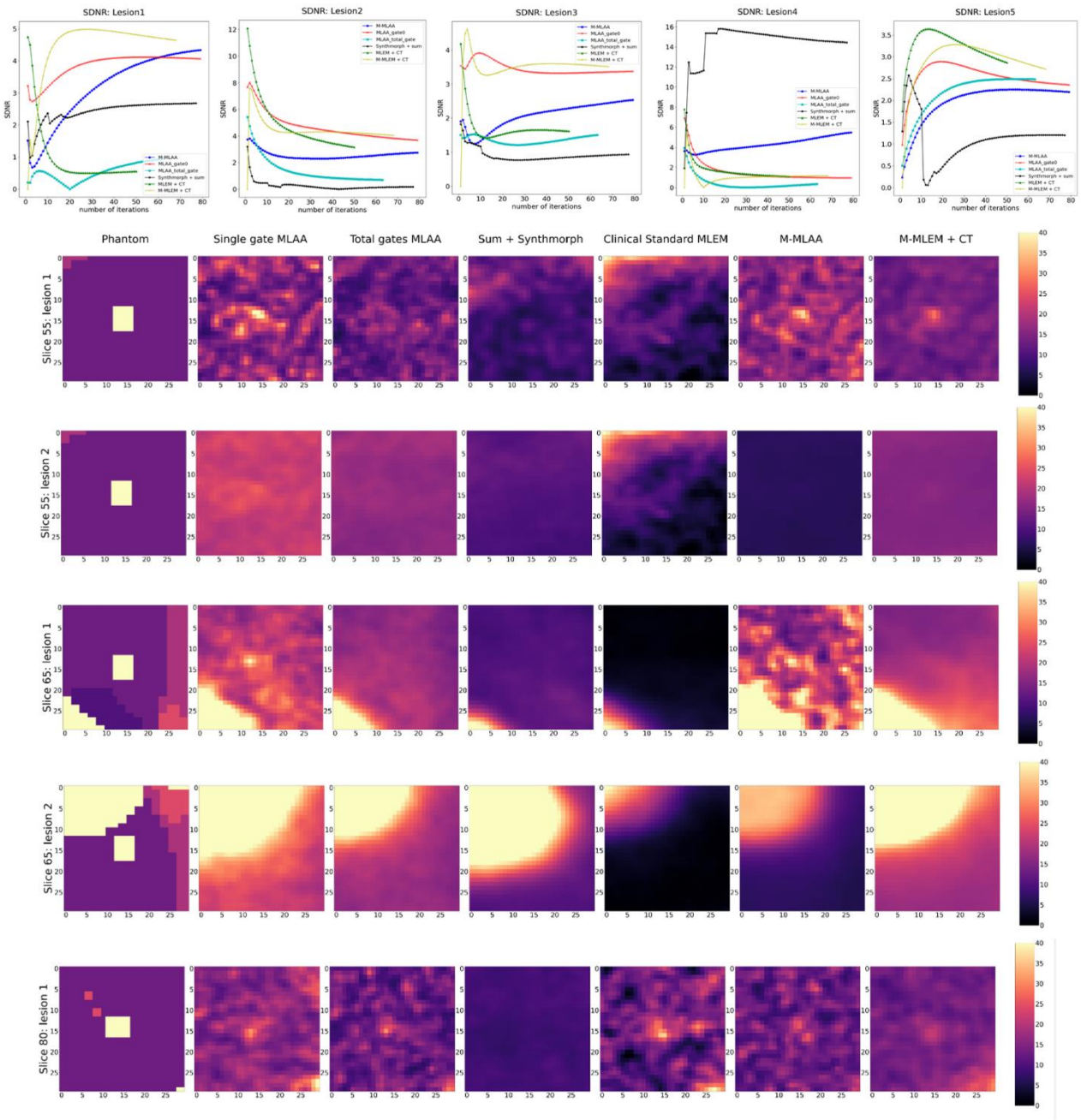

Figure 38 *- RC as a function of iteration number (top row) and reconstruction of the lesions at the optimal number of iterations for each of the tested algorithms.*

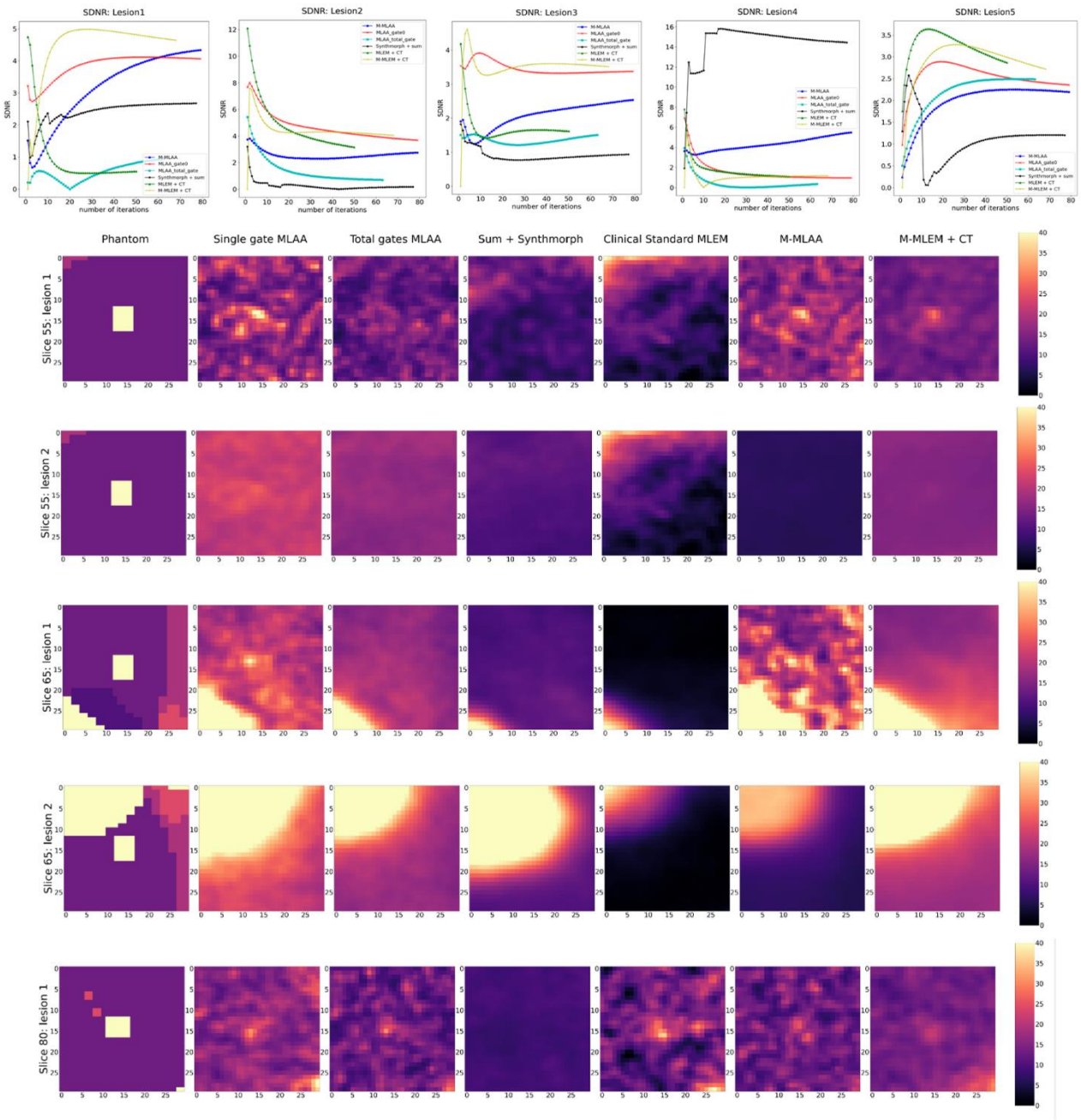

Figure 39 *- SDNR as a function of iteration number (top row) and reconstruction of the lesions at the optimal number of iterations for each of the tested algorithms.*

The CHO here implemented consists of four channels, each one constituted by a Gabor filter. Gabor filters are chosen because they have been proved to mimic the response of cells of the striate cortex. Gabor filters have been implemented using the skimage.filters module from the Scikit-image library. The parameters of the Gabor filters have been set to a spatial frequency that varies between 0.01 and 0.02 pixels, orientation that varies between 0.01 and 0.05 radians, bandwidth of 0.9 octaves and standard deviation of 3. The ROIs that have been considered have dimension of 10x10: 5 are evaluated around the lesions and 20 in the background only; in both cases they are taken within the slices 55,65 and 80 which contain the lesions in the 4D XCAT phantom.

Before feeding in the CHO, a Gaussian filter with $\sigma = 0.8$ is used to reduce the noise within the reconstructed images. Gaussian filters have been implemented from the scipy.ndimage.gaussian_filter module of the scipy.ndimage package. A block scheme for the implementation of the CHO is reported in *Figure 40 a*, with the aim to compute the test statistic.

The results obtained with the CHO are, instead, more compatible with what the visual inspection suggests (see *Figure 40 b*), with *M-MLEM + CT* and *M-MLAA* outperforming the other algorithms and having similar performances (AUC of 0.78 and of 0.77, respectively). According to the CHO, *single-gate MLAA* and *sum + Synthmorph* give the worst reconstructions, with *sum + Synthmorph* exhibiting a worse performance than simple random guessing. On passing, let us here point out that we are aware of the fact that, in cases like the one here presented, it is always possible to improve the performance of an observer that is performing under the 0.5 AUC threshold (corresponding to random guessing), by simply reversing the observer predictions. This is, however, not relevant in the present case as the above inversion would still yield an AUC value of 0.54, which is still close to random guessing. As a last note, it is worth noting that scatter and random corrections have not being considered in this study and need to be included before applying the two proposed algorithms to clinical data. This does not constitute a substantial challenge, since the algorithms can be easily extended to account for those two corrections, just as is routinely done with MLEM. Also, the hyperparameters of both *M-MLEM + CT* and *M-MLAA* can be further optimised, in particular regarding the optimal number of initial MLAA iterations before feeding reconstructed images in Synthmorph for the evaluation of the registration fields.

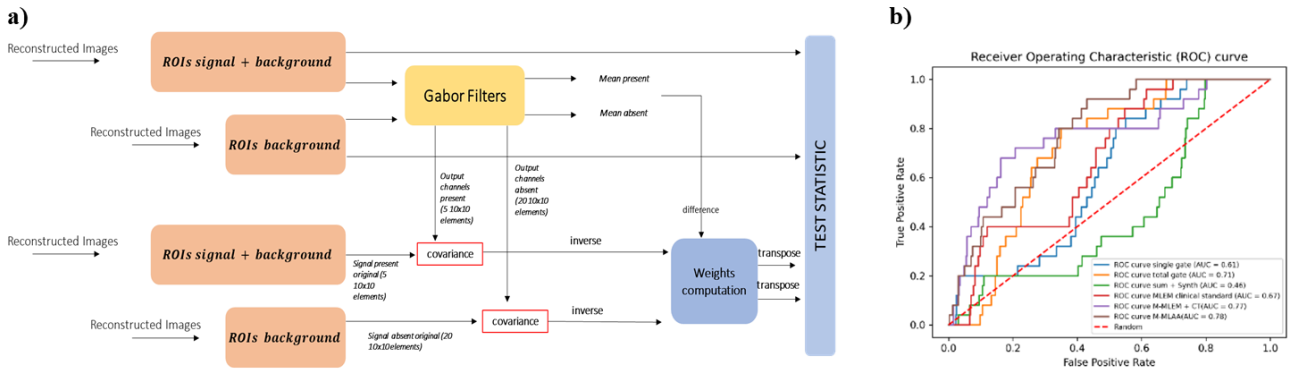

Figure 40 *– a) block-scheme for the implementation of the CHO; b) ROC-AUC curve of the different algorithms evaluated through CHO*

5 Future perspectives

The M-MLEM algorithm presented in reference [104]has been further developed to enable the reconstruction of the entire 3D volume from a realistic PET scan at once, and attenuation correction has been added to the algorithm. Our results on synthetic data suggest that the proposed M-MLEM + CT and M-MLAA algorithms have the potential to improve PET imaging diagnostic power for small pulmonary lesions at a low extra

computational cost compared to standard MLEM or MLAA. Considering that SynthMorph does not need any training on clinical data, there is a good potential for this method to be clinically viable.

Chapter 4 – *in-vitro analysis of nanoparticles library diffusion in ECM-mimicking hydrogels: an approach towards the definition of connections between nanoparticles properties and their diffusion behaviour in hydrogels mimicking different pathological stage of ECM.*

1 Background

1.1 Extracellular matrix as a biological hydrogel

The Extracellular Matrix (ECM) comprises the non-cellular components of all tissues, serving as both a structural scaffold and a source of biochemical signals. The ECM functions as a biological hydrogel, acting as a selective diffusion barrier that permits the passage of certain macromolecules while excluding others. This selective filtration in a biological hydrogel is mainly achieved through two mechanisms. The first mechanism is size exclusion, where macromolecules smaller than a specific mesh size can pass through. The second mechanism involves interaction-based filtration, where some macromolecules, due to their surface properties, can strongly interact with ECM components and become trapped within it[114]. Size exclusion and interaction filter are not mutually exclusive. The two mechanisms are reported in Figure 41.

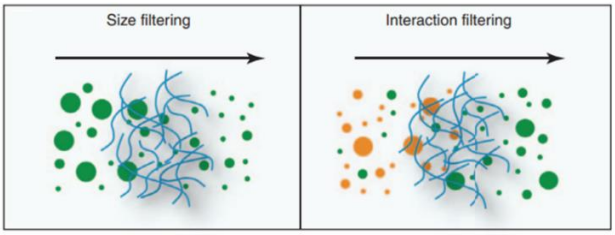

Figure 41 *– size exclusion and interaction filtering in biological hydrogels (from [114])*

In this context, *Sykes et al.* [3] developed a confocal microscope protocol to measure the diffusion of gold nanoparticles into hydrogels with varying collagen concentrations, simulating changes in the ECM caused by tumor growth. *Tomasetti et al.* [115] employed Fluorescence Recovery After Photobleaching (FRAP) to analyse the effect of different PEGylation degree of silica nanoparticles within collagen hydrogel and Matrigel models. *Burla et al.* [116] utilized Differential Dynamic Microscopy (DDM) and Single Particle Tracking (SPT) to investigate the diffusion of PEGylated polystyrene nanoparticles in various types of hyaluronan hydrogels, each characterized by a different degree of cross-linking.

2 Short Aim of the chapter

In this chapter, the aim is to present a tool for probing the diffusion of nanoparticles within hydrogels that mimic tumor ECM at different stages of the disease. These stages are characterized by different Young's modulus and porosity values. Looking ahead, the preliminary results obtained suggest that a more extensive analysis can be performed using a wider library of nanoparticles and testing it in different pathophysiological conditions. This analysis aims, as future perspective, to uncover hidden connections between the tumor ECM properties and the design features of nanoparticles.

3 Materials and Methods

3.1 Materials

3.1.1 Biomimesys hydroscaffolds

BIOMIMESYS® matrices are made of Hyaluronic Acid (HA), collagens and adhesion proteins. Their composition can be finely tuned by varying extracellular matrix components and their proportions, thus allowing a more or less dense and compact cellular environment (*i.e.*, through different Elastic Modulus and porosity) to be mimicked, depending on the organ or tissue of interest. Moreover, BIOMIMESYS® matrices are different from standard hydrogels because, due to their hydroscaffold nature, exhibit a dual behavior between a solid scaffold and a hydrogel, as the in vivo ECM.
Among the available types of hydroscaffold offered by BIOMIMESYS®, BIOMIMESYS® *Oncology* has been selected; this hydroscaffold is enriched in collagen I and can be characterized by different stiffnesses ($1\ kPa, 8\ kPa, 16\ kPa$ are the one that have been selected).

3.1.2 Hydration Scaffold Protocol

To hydrate the de-hydrated Biomimesys Hydroscaffolds, different steps have been followed:

1) Add slowly 30 μL of water, PBS or medium alone or with nanoparticles/dye inside in the middle of the de-hydrated scaffold.
2) Wait until diffusion of water, PBS or medium inside the de-hydrate scaffolds.
3) Add 170 μL of aqueous medium around the hydrated scaffold to keep it hydrated.
4) Store Overnight in the refrigerator at 4°C.

5) Once the scaffold has been hydrated, remove the aqueous medium and transfer the scaffold in the observation plate.

3.1.3 Confocal Protocol Settings and Experiment Analysis

To analyse diffusion of nanoparticles in Biomimesys Hydroscaffold, different steps have been followed:

1) $100\ \mu L$ of nanoparticles' suspension at a concentration of $10^9 - 10^{11}\ {particles}/{mL}$ is put directly in contact with the scaffold hydrated as above described;
2) an overnight experiment is conducted, by selecting different interfaces, different positions and different time points at each of which z-stacks are captured;
3) two different tools, described below, are used to derive the number of nanoparticles at each interface or the diffusion coefficient of nanoparticles.

Two different tools have been selected to analyse the confocal microscope experiments executed as before:

1. The *ImageJ Particle Analyzer Tool* allows for the selection of particle size and circularity criteria, allowing the counting of nanoparticles present at each interface.
2. Additionally, a Python script, employing *scipy.optimize.curve_fit*, has been developed for Mean Squared Displacement analysis, enabling the extraction of the diffusion coefficient.

4. Results

4.1 Validation of the Confocal Microscope Protocol

As it is reported in *Figure 42*, different attempts were made in defining the right protocol that can allow to quantify the diffusion behavior of the nanoparticles in the hydroscaffold. Firstly, $10\ and\ 20\ \mu L$ of nanoparticles' solution was used to directly hydrate the hydroscaffold (*Figure 42 a*), but in this case, since the hydroscaffolds' structure is thought to accommodate cells for 3D cell culture purposes, the nanoparticles were distributed immediately inside the matrix. Even if, at different time instants, it was possible to observe nanoparticles' diffusion inside the scaffold at a fixed interface along its depth, this kind of experiment didn't allow to perform observations about the dynamic of nanoparticles' penetration and diffusion. The second attempt was to create a separation between the hydroscaffold and the nanoparticle solution (*Figure 42 b*), by hydrating the hydroscaffold with PBS and creating an interface between nanoparticle solution and hydroscaffold with another layer of PBS. The best results were obtained, however, by putting directly in

contact the hydroscaffold with the nanoparticles' solution (*Figure 42 c*), at a concentration of 10^9 $\frac{particles}{mL}$, but ensuring that the hydroscaffold was well hydrated with PBS before running the experiment. This allowed, by performing an overnight experiment and by fixing an interface along the depth of the hydroscaffold, to visually observe how the accumulation of nanoparticles changed in time.

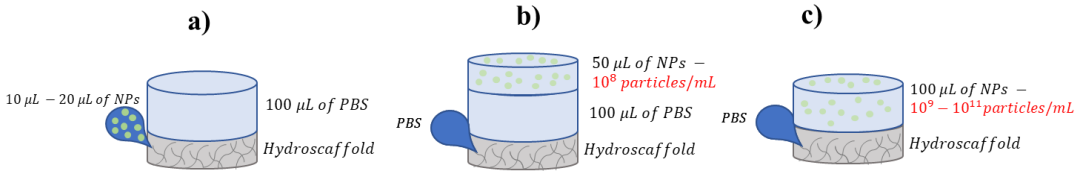

Figure 42 *– Validation of the Confocal Microscope Protocol*

4.2 1 *kDa ECM* mimicking hydroscaffold: *cHANPs vs polystyrene*

Two different set of nanoparticles have been used to conduct the confocal microscope experiment, as above explained. Commercially available $80nm$ polystyrene nanoparticles have been tested in a $3h$ experiment, while cHANPs have been tested for $14h$. ImageJ tools has been exploited to analyse diffusion of cHANPs and derive the number of nanoparticles at the different time points, as it is possible to observe from *Figure 43*.

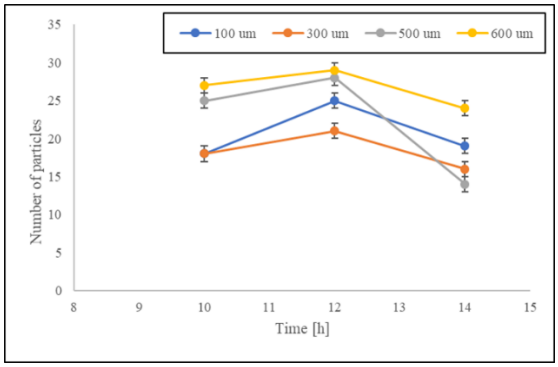

Figure 43 *– number of cHANPs nanoparticles accumulated within the hydroscaffold at different time points*

Figure 43 shows the accumulation of the nanoparticles at the bottom of the hydroscaffold, with a higher number of counts at the 600 μm interface at each time point.

On the other hand, Python scripts were used to analyse both the experimental set-ups and two different diffusion coefficients were extracted. Specifically, polystyrene nanoparticles exhibited a diffusion coefficient of 0.00055 $\mu m^2/_s$, whereas cHANPs showed a diffusion coefficient of 0.00041 $\mu m^2/_s$. Even though not significantly different, the lower diffusion coefficient observed in the case of cHANPs can be attributed by both the size-exclusion and interaction filtering mechanisms. cHANPs have a higher dimension with respect to polystyrene nanoparticles and being composed of hyaluronic acid, they have a higher interaction with hydroscaffold components compared to polystyrene ones.

5. Future perspectives

A further experimental campaign needs to be performed to validate this diffusion-analysis protocol, derive a diffusion/penetration model in the ECM and test different types of nanoparticles, (*i.e.*, in particular lipid-based and cell-derived ones), to make a comparison with the diffusion behavior of polymeric nanoparticles and derive a dataset to connect nanoparticles' design and ECM parameters, namely Young's modulus and porosity.

Chapter 5 – *predictive in silico model of nanoparticles delivery efficiency as a function of tumour type: a new proposed approach towards personalized nanomedicine*

This chapter includes parts taken from a paper under preparation: Cece, Fiorenza et al., "*A new approach towards personalized nanomedicine: from data generation to machine learning analysis of nanoparticles transport condition in pathological tissues for the identification of Nanoparticle Delivery Efficiency"*

1. Background

1.1 Artificial Neural Network for the Inverse Design of nanoparticles

ML/AI tools, as already underlined in the previous chapters, have found their application in nanomedicine. However, few attempts have been made in trying to modulate the NP design by looking at desired nano-bio interactions. In one of most significant attempts, *Hassan et al.* [117] proposed an approach to design NPs with specific nano-bio behaviours, referring, specifically, to ultrasmall NPs interacting with membranes. The approach integrates multiscale and pattern recognition techniques to guide NP design by collecting data from simulations or experiments to train artificial neural networks optimized for various nano-bio interactions. These trained networks are then interconnected to determine the NP core morphology and layer composition that best satisfy complex behaviours. In particular, as it can be observed from *Figure 44*, the inputs of the neural network are represented by $\boldsymbol{p}$ and $\boldsymbol{e}$. With $\boldsymbol{p}$ it is intended the characterization of the nanoparticle; $\boldsymbol{p}$ by itself is constituted by other two nodes, which are $\boldsymbol{d}$, that is the core morphology and $\boldsymbol{l}$ that is the coating layer. On the other hand, $\boldsymbol{e}$ stands for the bio-environment and the two constituting nodes are $\boldsymbol{m}$, that is the type of membrane, and $\boldsymbol{c}$, that are the solution conditions. The paper proposes a *reverse engineering* approach by which the best nanoparticles properties (*i.e.*, $\boldsymbol{p}$), for the desired binding energy $\boldsymbol{\varepsilon}$, binding mode $\boldsymbol{\rho}$ and membrane penetration $\boldsymbol{\mu}$, are selected. In this paper, it is, thus, introduced the approach of *inverse design*, through which it is possible to find, through the use of an artificial neural network, the input data that are most compatible with the desired output data.

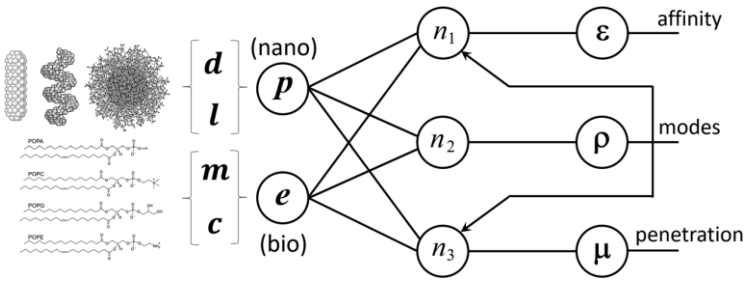

Figure 44 - *Schematic representation of the neural network proposed for the inverse design of nanostructures with specific nano-bio interactions*[117]

2. Short Aim of the work

In this chapter, we aim to develop a machine learning/artificial intelligence model capable of predicting, nanoparticle delivery efficiency (NDE), based nanoparticles design features and clinical characterization of tumors. This prediction relies on identifying the optimal and best transport properties of nanoparticles, specifically vascular permeability and ECM diffusivity. In order to do so, we rely on the generation of "synthetic data", by performing a screening of existing literature data. This screening involves the analysis of the impact of physical properties of different macromolecules (*i.e.*, BSA, dextran, liposomes) on their vascular permeability and ECM diffusivity in tumor animal models.

3. Methods

3.1 Identification of nanoparticles properties and tumour parameters

The dataset defines relationships between specific nanoparticles properties and clinical characterization of the tumor.

To identify nanoparticles properties, a screening of literature data, demanded at analyzing the impact of physical properties of different macromolecules (*i.e.*, BSA, dextran, liposomes) on their vascular permeability and extracellular matrix (ECM) diffusivity in tumor animal model, was performed. To this purpose, six trends were extracted from relevant studies: vascular permeability *vs* size, vascular permeability *vs* charge, vascular permeability *vs* viscosity, ECM diffusivity *vs* size, ECM diffusivity *vs* charge, ECM diffusivity *vs* viscosity. *Details on the selected studies are included in Appendix of this chapter.*

While the meaning of size and charge of a nanoparticle suspension is straightforward, viscosity was used to account for the material type and concentration of the nanoparticle suspension and was set to three different arbitrary chosen thresholds. On the other hand, to connect vascular permeability and ECM diffusivity of the

nanoparticles to structural clinical properties of the tumor, two transport phenomena equations were used (*look at* Eq.1, Eq.2 and Eq.3 reported in chapter 1)[7]. Since, the second term on the right side of Eq. 1 represents the convective contribute to the flux J of nanoparticles and since it is shown that it mainly relies on a diffusive transport mechanism [7], Eq. 2 is directly used in the dataset generation to account for vascular permeability of nanoparticles.

3.2 Identification of dataset structure

From the transport phenomena equations (Eq. 2 and Eq. 3) and pre-processed collected trends, an Excel spreadsheet was used to build two different datasets for vascular permeability and ECM diffusivity respectively. The first, outlined in *Figure 45*, computes $\frac{P}{P_{normal(max)}}$ according to the following formula (Eq. 15):

$$\frac{P}{P_{normal(max)}} = \left[\left(\frac{H*\gamma}{L}\right) * \left(\frac{correction\ factor\ for\ size}{P_{normal(max)\_correspondent\_study}}\right) + \left(\frac{H*\gamma}{L}\right) * \left(\frac{correction\ factor\ for\ charge}{P_{normal(max)\_correspondent\_study}}\right) + \left(\frac{H*\gamma}{L}\right) * \left(\frac{correction\ factor\ for\ viscosity}{P_{normal(max)\_correspondent\_study}}\right)\right] * (clinical\ penalty\ term) * \mathcal{D}_0 \qquad \text{(Eq. 15)}$$

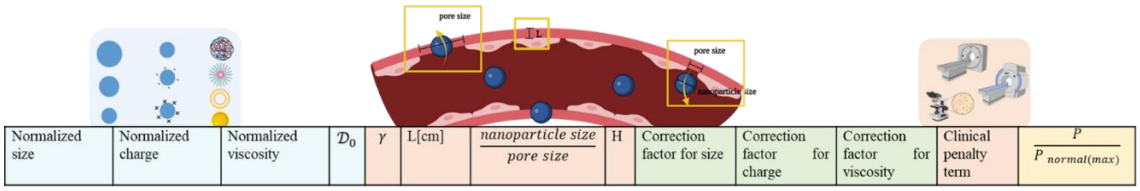

Figure 45 *- Vascular permeability computation*

The latter, outlined in *Figure 46*, computes $\frac{D}{D_{normal(max)}}$ according to the following formula (Eq. 16):

$$\frac{D}{D_{normal(max)}} = \left[\left((1-\varphi)^2 * \exp\left(-\sqrt{\varepsilon_{int}} * \frac{nanoparticle\ size}{R_f}\right)\right) * \left(\frac{correction\ factor\ for\ size}{D_{normal(max)_correspondent_study}}\right) + \left((1-\varphi)^2 * \exp\left(-\sqrt{\varepsilon_{int}} * \frac{nanoparticle\ size}{R_f}\right)\right) * \left(\frac{correction\ factor\ for\ charge}{D_{normal(max)_correspondent_study}}\right) + \left((1-\varphi)^2 * \exp\left(-\sqrt{\varepsilon_{int}} * \frac{nanoparticle\ size}{R_f}\right)\right) * \left(\frac{correction\ factor\ for\ viscosity}{D_{normal(max)_correspondent_study}}\right)\right] * (clinical\ penalty\ term) * \mathcal{D}_0 \qquad \text{(Eq. 16)}$$

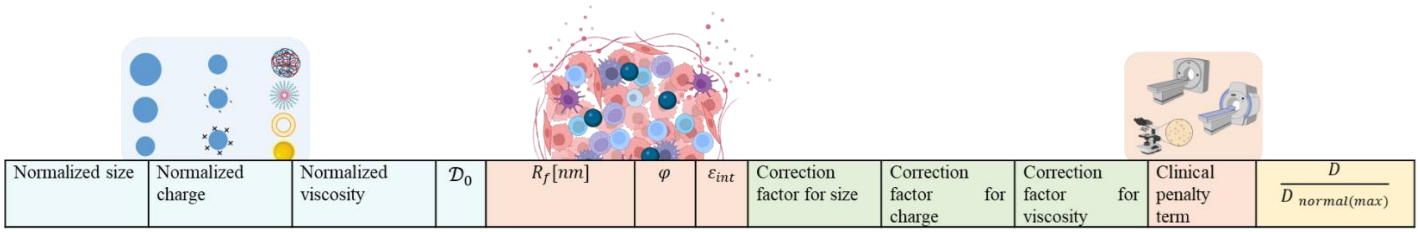

Figure 46 - ECM diffusivity computation

3.3 Data pre-processing and dataset generation

Each trend collected from literature was pre-processed in the following way, through a *two-step normalization strategy*.

First of all, vascular permeability and ECM diffusivity of each molecule were normalized, dividing them by the maximum vascular permeability ($P_{normal(max)}$) and ECM diffusivity ($D_{normal(max)}$) of the same molecule in the non-pathological tissue. More in detail, the vascular permeability and ECM diffusivity of the molecule in the tumor tissue model was divided by the correspondent maximum values in the equivalent non-pathological tissue (when available from the same study) or by averaging the molecule vascular permeability and ECM diffusivity in multiple non-pathological tissues. *The obtained trends are reported in Appendix of the chapter*. Then, each physical property (*i.e.*, size, charge, viscosity) of the molecule was normalized dividing by the corresponding maximum value included in the study, thus obtaining normalized size, normalized charge and normalized viscosity. The trends resulted by considering both the normalized physical properties of the molecule and the normalized transport properties (*i.e.* $\frac{P}{P_{normal(max)}}$ vs normalized size; $\frac{P}{P_{normal(max)}}$ vs normalized charge; $\frac{P}{P_{normal(max)}}$ vs normalized viscosity; $\frac{D}{D_{normal(max)}}$ vs normalized size; $\frac{D}{D_{normal(max)}}$ vs normalized charge; $\frac{D}{D_{normal(max)}}$ vs normalized viscosity) were respectively used to compute different correction factors (*i.e.*, correction factor for size, correction factor for charge, correction factor for viscosity) for both vascular permeability and ECM diffusivity. These correction factors were combinedly used as multiplicative terms in the computation of $\frac{P}{P_{normal(max)}}$ and $\frac{D}{D_{normal(max)}}$, as reported in *Eq. 15* and *Eq. 16*. Finally, two further multiplicative terms (*i.e.*, penalty terms) were introduced for vascular permeability and ECM diffusivity respectively. In particular, the penalty term for vascular permeability was computed averaging the k_{trans} (representing the capillary permeability) values across different stages of the same tumor; two types of tumor (*i.e.*, brain and breast) were considered. Similarly, penalty term for ECM diffusivity was computed averaging ADC values (measuring the diffusion degree of water molecules within the tissue). These penalty terms were used in the computation of $\frac{P}{P_{normal(max)}}$ and $\frac{D}{D_{normal(max)}}$.

The k_{trans} and ADC values were got from different studies [12, 14, 17, 118] and the respective data are reported in Appendix of the chapter. Equivalently to the approach used for the two-step normalization, the clinical penalty

terms were normalized dividing each of them by the maximum ADC and the maximum k^{trans} respectively, considering the two tumor types (*i.e.*, brain and breast tumor).

3.4 Definition of the Nanoparticle Delivery Efficiency (NDE) and building of the predictive in-silico model

Since the computation of the viscosity for a nanoparticle suspension is not straightforward and given the strong impact of the material on the aforementioned transport properties, three different averaged viscosities (1.0 cP, 2.5 cP, and 3.5 cP) were set to simulate three different materials (Material_1, Material_2, and Material_3).

The final generated dataset has been used to define the *Nanoparticle Delivery Efficiency (NDE)*, computing $\frac{P}{P_{\,normal(max)}}$ and $\frac{D}{D_{\,normal(max)}}$ for specific nanoparticles features and tumor type and comparing these values against two thresholds, namely $threshold_P$ and $threshold_D$. These two thresholds were computed considering the average of $\frac{P}{P_{\,normal(max)}}$ and $\frac{D}{D_{\,normal(max)}}$ across all the nanoparticle features and tumor type of the generated dataset.

The comparison of $\frac{P}{P_{\,normal(max)}}$ with $threshold_P$, and $\frac{D}{D_{\,normal(max)}}$ with $threshold_D$ resulted in the definition of an *efficient nanoparticle* when both the obtained values were higher than the respective thresholds, a *moderate efficient nanoparticle* when only one of the two values was higher than the respective thresholds, and a *not efficient nanoparticle* when both the values were lower than the respective thresholds; the strategy is schematized in *Table 10*.

If $\frac{P}{P_{\,normal(max)}} > threshold_P$ & if $\frac{D}{D_{\,normal(max)}} > threshold_D$	**EFFICIENT NANOPARTICLE**
If $\frac{P}{P_{\,normal(max)}} < threshold_P$ & if $\frac{D}{D_{\,normal(max)}} > threshold_D$	**MODERATE EFFICIENT NANOPARTICLE**
If $\frac{P}{P_{\,normal(max)}} > threshold_P$ & if $\frac{D}{D_{\,normal(max)}} < threshold_D$	**MODERATE EFFICIENT NANOPARTICLE**
If $\frac{P}{P_{\,normal(max)}} < threshold_P$ & if $\frac{D}{D_{\,normal(max)}} < threshold_D$	**NOT EFFICIENT NANOPARTICLE**

Table 10 *- Strategy for the definition of the NDE*

The *NDE* of a number of nanoparticles with respect to two tumor types (*i.e.*, brain and breast) was then computed. To this purpose, nanoparticles made of three different materials at a fixed concentration of 1 mg/mL, with sizes ranging from 20 nm to 150 nm, and charges from $-30mV$ to $+30mV$, were chosen. The *NDE* of the same nanoparticle was evaluated both for brain and breast tumor.

Nanoparticles properties and tumor type were, subsequently, selected as the input of different classification algorithms, with the previously computed *NDE* (*i.e.*, *EfficientNanoparticle*, *ModerateEfficiency*, and *NotEfficient*) as predicted output of the model. A schematic outline of the dataset is reported in *Table 11*.

INPUT					OUTPUT
Size[nm]	Charge [mV]	Material	Concentration [mg/mL]	Tumor Type	NDE

Table 11 *– ML/AI dataset structure*

3.5 Selection, implementation and evaluation of Classification Models

The aforementioned dataset was analyzed and modeled through different machine learning (ML) methods: Support Vector Machines (SVMs), Decision Trees (DTs) and Multi-Layer Perceptron Artificial Neural Network (MLP-ANN).

ML methods were implemented in Python language (ver. 3.0), using the web-based interactive computational environment Jupyter Notebook. SVM and DT algorithms were written through the open-source Python module Scikit-learn (ver. 1.2.2) [119], while the MLP-ANN algorithm was written through TensorFlow module (v2.12.0) [120].

The dataset was properly pre-processed before the implementation of the algorithms by means of one-hot encoding of the two categorical features (*i.e.*, material and tumor type), standard scaling of the numerical ones (*i.e.*, size, charge, and concentration), and label encoding of the output variable (*i.e.*, *NDE*) to convert the dependent variables to numeric form.

The pre-processed dataset was then split into training and testing sets, with a proportion of 80-to-20 %, and the training set was used to train the algorithm, leaving all hyperparameters to default values.

Several metrics commonly employed in classification tasks were used to evaluate the performance of the three models; such metrics provide insights into different aspects of the models' performance and are hereby described:

1. *Accuracy* measures the proportion of correctly classified instances (of the testing set) out of the total number of instances in the dataset. It provides a general overview of the model's overall performance.
2. *Precision* measures the proportion of the true positive predictions (of the testing set) out of the total predicted positives.
3. *Recall* (*i.e.*, sensitivity or true positive rate) measures the proportion of true positive predictions (of the testing set) out the total actual positives. It is representative of the model's ability to correctly spot positive instances.
4. *F1 score* is obtained as harmonic mean of recall and precision. It is representative of a balanced measure of the model's performance.
5. *Area under the curve* (AUC) provides a measure of the classifier's ability to distinguish between classes.

Confusion Matrix was built to have a visual representation of the true values against the predicted ones.
To understand the relative importance (or contribution) of each independent variable in predicting the target one, feature importances was evaluated. As one-hot encoding was used to represent categorical variables, so that each label is transformed into a separate binary feature, feature importances was then computed separately for each of these binary features, thus indicating the importance of each label in predicting the target variable. For the MLP-ANN, the feature importance is directly estimated from the weights of each node.
Moreover, the Receiver Operating Characteristic (ROC) for each model was computed and plotted to visualize the models' performances.
After the general implementation, each one of the models was optimized through a two-steps approach: grid search and k-fold cross-validation. The optimization process is detailed below, together with a description of the three algorithms.

3.5.1 Support Vector Machine (SVM) classifier

Support Vector Machine (SVM) is a supervised machine learning algorithm used for both regression and classification tasks. In this work, the SVM algorithm is implemented for classification purposes. The algorithm works by finding an optimal hyperplane that maximally separates different classes in the feature space. SVM appears to be particularly effective in scenarios where data are not linearly separable, given its ability to leverage kernel functions to transform the data into higher-dimensional feature spaces [121].
A preliminary model optimization was performed through grid search approach, a method used to tune the model's hyperparameters. It works by defining a grid of hyperparameter values to be investigated and searching through them to find the combination leading to the best performance according to the metrics discussed above. In this work, the searching grid is composed by the kernel choice (*linear* and *round basis function*), the regularization parameter C (*0.1*, *1*, and *10*), and the *gamma* kernel-specific parameter (*scale* and *auto*).
Once the best combination of hyperparameters was obtained, the generalization performance of the SVM classifier model was assessed through the k-fold cross-validation technique. It involved splitting dataset into k equally sized folds, training the model on k-1 folds, and testing it on the last fold; this process is then repeated k times, with each fold being used as the validation set once. The performance metrics were then averaged across all folds, thus leading to a more robust estimation of the model's performance. For this purpose, a number of folds equal to 5 was selected.
Further details of the models' implementation are included in Appendix of the chapter.

3.5.2 Decision Tree (DT) classifier

The Decision Tree algorithm is a tree-based machine learning algorithm used for both classification and regression tasks. It recursively partitions the data points into subsets based on the values of the input features

[122]. The algorithm learns a tree-like structure, in which each internal node represents an input feature, each branch represents a decision based on the respective feature, and each leaf node represents a class label (*i.e.*, output variable).

A preliminary model optimization was performed through grid search approach described above; the searching grid is composed by the criterion choice, that is the function demanded to measure the quality of a split, being set to *Gini impurity* and *entropy*, the maximum depth of the tree (*None*, *5*, *10*, and *15*), the maximum number of samples required to split an internal node (*2*, *5*, and *10*), and the minimum number of samples required to split an internal node (*1*, *2*, and *4*).

Once the best combination of the aforementioned hyperparameters was obtained, the generalization performance of the DT classifier was assessed through the k-fold cross-validation by selecting a number of folds equal to 5. Then, the quality metrics were averaged across all folds.

Further details of the models' implementation are included in Appendix of the chapter.

3.5.3 Multi-Layer Perceptron Artificial Neural Network (MLP-ANN) classifier

The Multi-Layer Perceptron Artificial Neural Network (MLP-ANN) is a type of feedforward neural network consisting of multiple layers of fully interconnected nodes (*i.e.*, neurons). Each neuron applies a specific non-linear activation function to the weighted sum of its inputs.

The implementation, done by using the TensorFlow module (v2.12.0) [120], was based on the Sequential model which allows to stack multiple layers sequentially. Four layers were defined, each one with an activation function and a fixed number of nodes: the first layer (*i.e.*, the input layer) accounting for 8 nodes (each one for a specific input variable) and Rectified Linear Unit (ReLU) as activation function, the second one (*i.e.*, the first hidden layer) accounting for 10 nodes and ReLU as activation function, the third one (*i.e.*, the second hidden layer) accounting for 5 nodes and ReLU as activation function, and the fourth one (*i.e.*, the output layer) accounting for 3 nodes and SoftMax as activation function.

The model was then compiled choosing the sparse categorical cross-entropy as loss function to minimize, using the Adam optimizer and the accuracy metric.

Finally, the model was trained over 100 epochs selecting a batch size equal to 32.

Further details of the models' implementation are included in Appendix of the chapter.

4. Results

4.1 Application of transport phenomena equations to compute dataset features and nanoparticle delivery efficiency

Literature has widely demonstrated that design properties of nanoparticles (*i.e.*, charge, material, shape and surface decoration) have a significant impact on their transport properties (*i.e.*, extravasation across blood vessels, intercellular diffusion within tissues and intracellular uptake by tumor target cells).

Prior to the application of transport phenomena equations, since data were collected referring to both different molecules (*i.e.*, BSA, dextran and liposomes) and different tumor models (*i.e.*, human squamous cell carcinoma in dorsal chamber, VX2 carcinoma in ear chamber and human colon adenocarcinoma in dorsal chamber, Matrigel Matrix), the two-step normalization strategy, described in Methods section, was applied. The first step aimed to make vascular permeability and ECM diffusivity values, across different tumor types and experimental conditions, dimensionless, comparable and uniform.

The second normalization step aimed to extend the range of properties that can be investigated through the proposed approach by capturing, in the generated dataset, properties closer to the ones of nanoparticles rather than to the ones of the small molecules analyzed in the collected studies.

The trends, generated through the explained strategy, are reported in *Figure 47*.

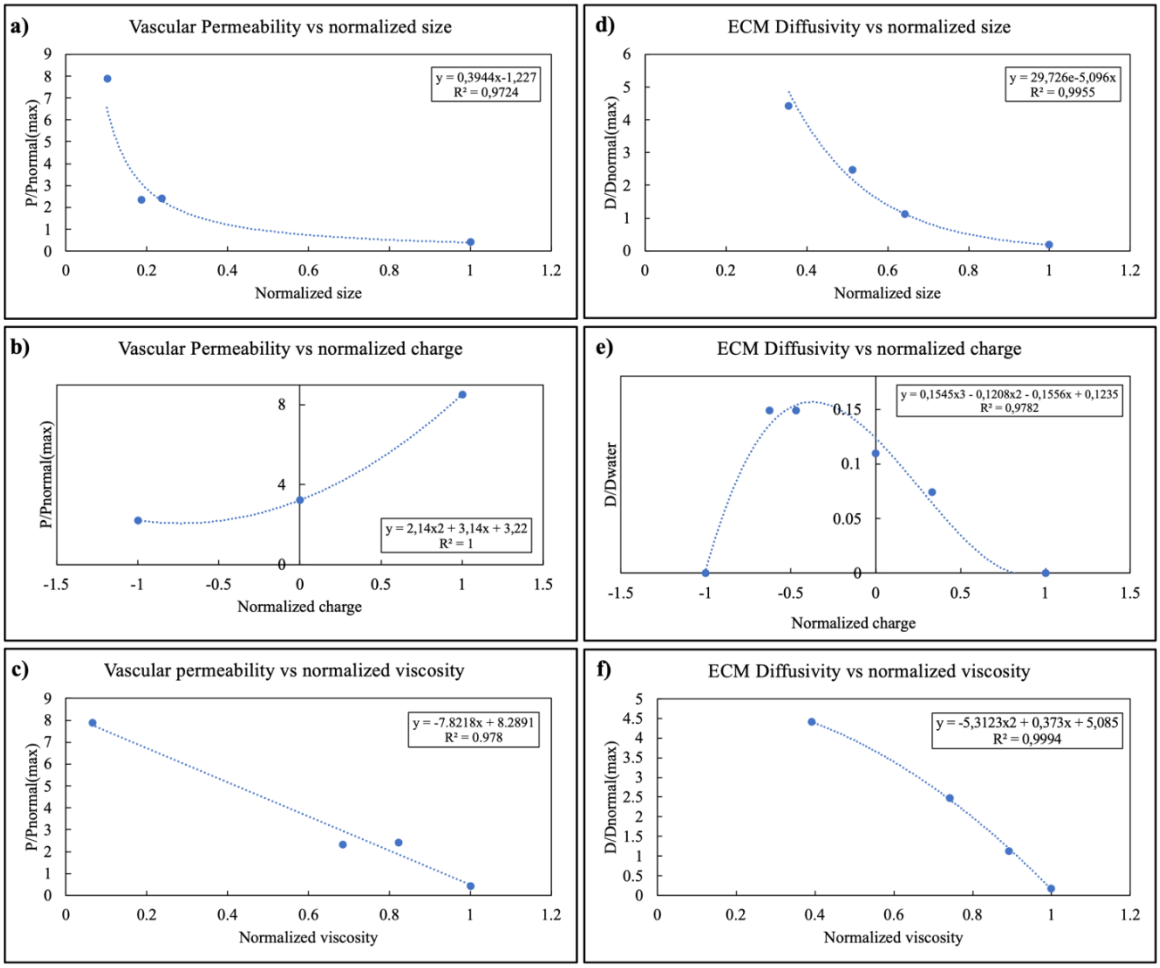

Figure 47 *- Generated trends: vascular permeability vs normalized size (a), normalized charge (b), and normalized viscosity (c); ECM diffusivity vs normalized size (d), normalized charge (e), and normalized viscosity (f).*

The generated trends show that, in accordance with the available knowledge about nanoparticles transport properties [6, 7, 123-126], the increase in nanoparticle size and stiffness leads to a decrease in vascular permeability

and ECM diffusivity. Relatively to the effect of charge, positively charged nanoparticles show a higher vascular permeability due to their electrostatic interaction with the negatively charged endothelial cells; on the other hand, slightly negative charged and neutral nanoparticles show enhanced ECM diffusivity due to their reduced electrostatic interaction with ECM fibers.

The corrections factors for vascular permeability and ECM diffusivity, computed from the trends in *Figure 47*, are reported in *Tab. 11*.

Correction factors are exploited as multiplicative factors for the calculation of $\frac{P}{P_{normal(max)}}$ and $\frac{D}{D_{normal(max)}}$ as explained in the Methods section, thus accounting for the change of vascular permeability and ECM diffusivity depending on size, charge and viscosity of the nanoparticles. As it is possible to observe from *Tab.12*, through the correction factors both $\frac{P}{P_{normal(max)}}$ and $\frac{D}{D_{normal(max)}}$ values may be reduced up to two orders of magnitude from their maximum values, according to the change of nanoparticles properties. In particular, the correction factor for normalized nanoparticle size showed the highest impact on vascular permeability and ECM diffusivity, while the one for normalized nanoparticle charge had the lowest impact.

a)

Size[nm]	Normalized size	Correction factor for normalized size
5	0,05	15,570
25	0,25	2,161
50	0,5	0,923
75	0,75	0,561
100	1	0,394

Charge [mV]	Normalized Charge	Correction factor for normalized charge
-20	-1	2,22
-10	-0,5	2,185
0	0	3,22
10	0,5	5,325
20	1	8,5

Viscosity [cP]	Normalized Viscosity	Correction factor for normalized viscosity
0,7	0,583	3,726
0,78	0,65	3,205
0,8	0,667	3,075
1	0,833	1,771
1,2	1	0,467

b)

Size[nm]	Normalized size	Correction factor for normalized size
5	0,05	23,040
25	0,25	8,315
50	0,5	2,326
75	0,75	0,651
100	1	0,182

Charge [mV]	Normalized Charge	Correction factor for normalized charge
-20	-1	0,0038
-10	-0,5	0,152
0	0	0,124
10	0,5	0,035
20	1	0,0016

Viscosity [cP]	Normalized Viscosity	Correction factor for normalized viscosity
0,7	0,5833	3,495
0,78	0,65	3,083
0,8	0,667	2,973
1	0,833	1,707
1,2	1	0,146

Table 12 *- Correction factors computed from generated trends: a) correction factors for vascular permeability; b) correction factors for ECM diffusivity.*

By using this strategy, the minimum and maximum values of $\frac{P}{P_{normal(max)}}$ and $\frac{D}{D_{normal(max)}}$ computed from the final generated dataset were not absolute values, but had to be considered as relative to the range of sizes, charges and viscosities of the nanoparticles under consideration within the dataset, thus defining a relative scale of *NDE*.

Two further multiplicative terms, namely clinical penalty terms, were introduced (*Tab. 13*) to account for the clinical differentiation between tumors; those penalty terms were identified as a function of ADC and k^{trans} for both the tumor types under consideration (*i.e.*, brain and breast tumor).

Tumor Type	ADC[$10^{-7}\ cm^2/s$]	k_{trans} [min^{-1}]	ADC/ADC(max)	k_{trans} /k_{trans} (max)
Brain	132,4	0,086	1	0,148
Breast	94,7	0,578	0,715	1

Table 13 - Clinical penalty terms

An example of the computed *ND*E for different types of nanoparticles and the two tumors under consideration is reported in *Tab.14*. *Table 14* shows the potentiality of this approach in selecting the most promising nanoparticle, in terms of delivery efficiency, with respect to a specific tumor type. NP_1 was classified as an efficient nanoparticle for brain tumor and as a not efficient one for breast tumor; conversely, NP_3 resulted to be not efficient for brain tumor and presented a moderate delivery efficiency for breast one.

	Size[nm]	Charge [mV]	Material	Concentration [mg/mL]	Tumor Type	NDE
NP_1	60	0	Material_1	1	Brain	Efficient Nanoparticle
	60	0	Material_1	1	Breast	Not efficient
NP_2	100	-10	Material_2	1	Brain	Not efficient
	100	-10	Material_2	1	Breast	Moderate Efficiency
NP_3	60	20	Material_3	1	Brain	Not efficient
	60	20	Material_3	1	Breast	Moderate Efficiency

Table 14 - *NDE classification for different types of nanoparticles and tumors*

4.2 Machine Learning models optimization and evaluation

SVM and DT models were optimized using grid search and k-fold cross-validation in order to find the best combination possible of hyperparameters. For the SVM model, the best combination of hyperparameters found was C=10 and gamma='scale', with a round basis function as kernel. For the DT model instead, the best combination found was criterion='gini', max_depth=15, min_samples_leaf=1, min_samples_split=2. A graphical representation of both the Decision Tree (DT) and the Multi-Layer Perceptron Artificial Neural Network (MLP-ANN) implemented, is reported in *Figure 48*.

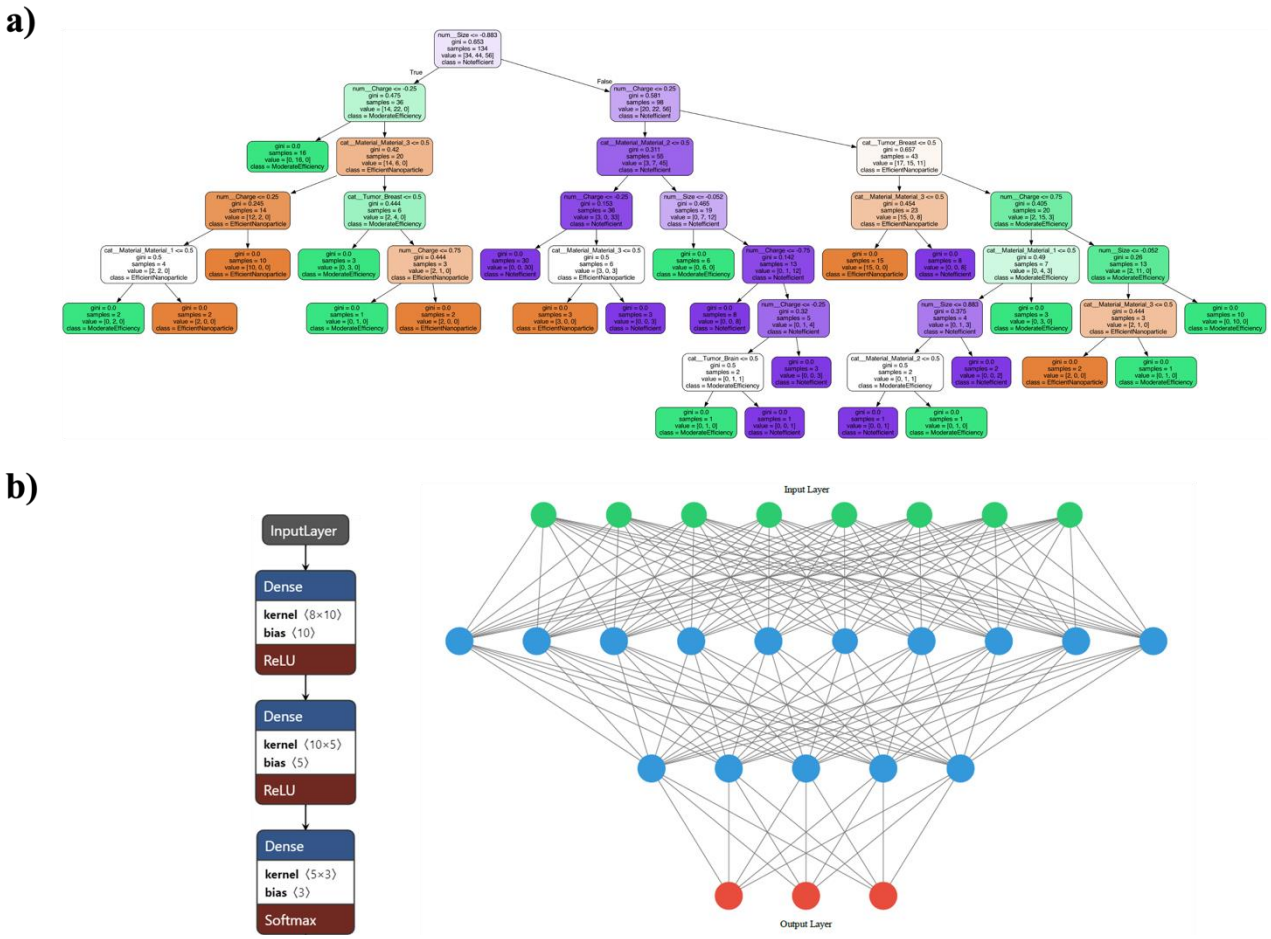

Figure 48 *- Decision Tree model (a); multi-layer perceptron artificial neural network (b).*

In case of the DT structure, reported in *Figure 48 a*, the color coding serves as a distinction between classes in the tree; more specifically, the color indicates to which class most of the samples belong to for that node: the darker the color, the higher is the concentration of samples for a particular class of the node. The MLP-ANN (*Figure 48 b*), accounting for eight input nodes (one for each independent feature, reported in green), two hidden layers (ten nodes for the first, five for the second one, reported in blue), and three output nodes (one for each predicting variable, reported in red), was built. Its structural optimization goes beyond the scope of this work. We evaluated the performances of SVM, DT and MLP-ANN in predicting the *NDE* on the generated dataset. *Tab. 15* summarizes the averaged classification accuracy, precision, recall, F1 Score, and AUC for each algorithm. In particular, the AUC was computed with respect to each output variable.

Algorithm	Accuracy	Precision	Recall	F1 Score	AUC
SVM	0.91	0.93	0.91	0.91	0.97
DT	0.79	0.85	0.79	0.80	0.86
MLP-ANN	0.76	0.77	0.76	0.76	0.91

Table 15 -Averaged evaluation metrics for all the algorithms implemented.

The SVM algorithm achieved an accuracy of 91% with a precision of 0.93, recall of 0.91, F1 Score of 0.91, and AUC of 0.97, indicating very good discriminative power. The DT algorithm achieved an accuracy of 79% with a precision of 0.85, recall of 0.79, F1 score of 0.80, and AUC of 0.86 suggesting good discriminative ability. The MLP-ANN showed an accuracy of 76% with a precision of 0.77, recall of 0.76, F1 Score of 0.76, and AUC of 0.91, indicating a moderate discriminative power. The confusion matrices (*Figure 49 a, b, c*), computed for each model, show the counts of true positive, true negative, false positive, and false negative predictions; basically, they allow to evaluate of how well the model is predicting each class and they represent a starting point to identify areas for improvement. In particular, a higher value on the diagonal (*i.e.*, true positive counts for each class) indicates a higher number of correct predictions. The confusion matrix related to the MLP-ANN (*Figure 49 c*) shows a slightly higher misclassifications compared to the other two (*Figure 49 a, b*), especially for the "*ModerateEfficiency*" class. The area under the ROC curve (ROC-AUC), reported in *Figure 49 d, e, f,* provides a measure of the classifiers' ability to distinguish between classes, by comparing the True Positive Rate (TPR) versus the False Positive Rate (FPR) for each one of the three predicting classes (*i.e., "EfficientNanoparticle", "ModerateEfficiency", "NotEfficient"*).

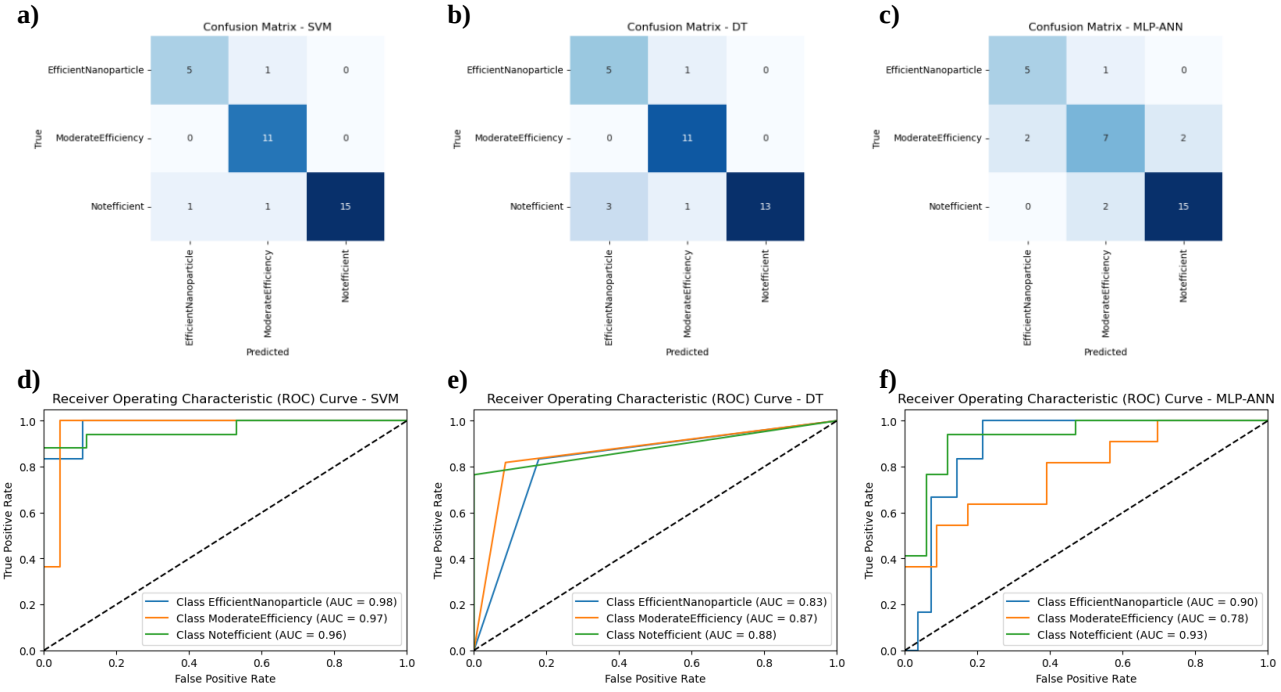

Figure 49 *- Confusion matrix for: SVM classifier (a), DT classifier (b), and MLP-ANN (c). ROC curve and AUC for: SVM classifier (d), DT classifier (e), and MLP-ANN (c).*

These results demonstrate the effectiveness of the SVM, DT, and MLP-ANN algorithms in classifying our dataset. The SVM algorithm showed highest accuracy and AUC compared to the other two, suggesting superior performances in this specific task; moreover, its ROC curves (*Figure 49 d*) are the closest to the upper-left corner of the plot (highest TPR and lowest FPR), indicating best-performing model for the three classes.

Finally, feature importances were computed (*Figure 50*). This approach allowed to assess the impact of each label within the categorical features on the models' predictions.

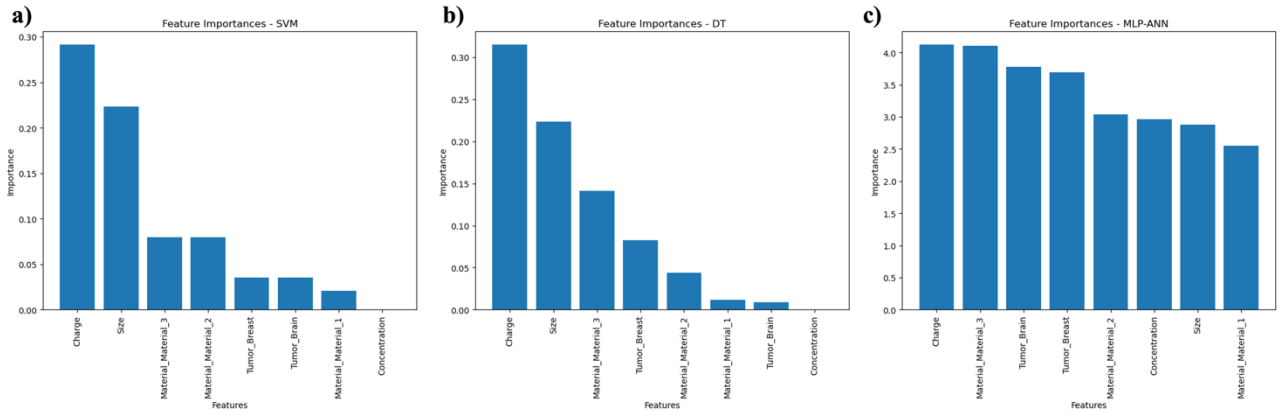

Figure 50 *- Feature Importances for: SVM classifier (a), DT classifier (b), and MLP-ANN (c).*

Feature importances play a crucial role in understanding the predictive power and contribution of each feature (independent variable) in the machine learning model. It provides a quantitative measure of the relevance of each feature in making predictions of the *NDE*. Influential features were determined by ranking; the most relevant ones resulted to be charge and size, for the SVM and DT models, with charge having the highest importance (*Figure 50 a, b*). On the other hand, in the MLP-ANN there is no significant difference between the feature importances. This could be due to how the feature importances are computed for the different ML models. In fact, in tree-based modeling they are retrieved directly from how much each feature contributes to the decision-making process; for ANN models, instead, which are based on complex interconnected layers, feature importances are not as straightforward to calculate. Since ANN models are highly flexible and capable of capturing very complex nonlinear relationships between features and target variables, the model relies on intricate combinations of features. As a result, feature importances are more distributed and less distinguishable for the MLP-ANN as can be noticed in *Figure 50 c*.

Appendix

Computation of vascular permeability in non-pathological tissues

Permeability of dextran and BSA in normal tissue were extracted respectively from [127] and [128] and reported in Table S1:

Macromolecule	MW [kDa]	Size [nm]	Pnormal[10-7cm/s]
Dextran	150	8,25	0,73
	10	5,01	4,06
	70	6,39	1,24
	2000	27	0,2

Macromolecule	Pnormal[10-7 cm/s]	Tissue
BSA	0,2-0,8	Normal cranium
	0,5	Normal liver
	0,5	Normal pancreas
	0,3-0,7	Normal skin

Table S16 – Permeability of Dextran (left); permeability of BSA (right) in normal tissues.

It is worth precising that $Pnormal$ for BSA was then computed by averaging across the values found for the different normal tissues.
On the other hand, ECM diffusivity of dextran and BSA in normal tissue were available from the same study considered to derive the trends of interest.

Trends extracted from literature

The data used to compute the trends were extracted from the following literature studies and are hereby reported (Table S2):

- Data for *Vascular Permeability vs Size* trend were adjusted from [129];
- Data for *Vascular Permeability vs Charge* trend were adjusted from [130];
- Data for *ECM Diffusion vs Size* trend were adjusted from [131];
- Data for *ECM Diffusion vs Charge* were adjusted from [132] and [115];
- Data for *Vascular Permeability vs Viscosity* and *ECM Diffusion vs Viscosity* trends were adjusted from [129] and [131] respectively, after proper computation of dextran viscosity from [133], as reported in the paragraph *Viscosity computation for the generation of the trends.*

- Vascular Permeability vs Size

Macromolecule	MW [kDa]	Size[nm]	P [10-7 cm/s]	Pnormal [10-7 cm/s]	P/ Pnormal	P/Pnormal(max)
Dextran	3.3	NA	154	NA	NA	NA
	10	2,73	32	4,06	7,881773399	7,881773399
	40	5,01	9,5	1,24*	7,661290323	2,339901478
	70	6,39	9,8	1,24	7,903225806	2,413793103
	2000	27	1,7	0,2	8,5	0,418719212

- Vascular Permeability vs Charge

Macromolecule	Isoelectric Point (pI)	P [10-7 cm/s]	Pnormal[10-7 cm/s]	P/ Pnormal(max)	Legend(0=native; -1=most negative; 1=most positive)
Native BSA	4.5	1,61	0,5	3,22	0
Anionized BSA	2	1,11	0,5	2,22	-1
Cationized BSA	8.6-9.1	4,25	0,5	8,5	1

- ECM Diffusion vs Size

Macromolecule	Size[nm]	MW [kDa]	D [10-7 cm2/s]	Dnormal	D/Dnormal(max)
FITC-D20	3,2	20	7,5	1,7	4,411764706
FITC-D40	4,62	40	4,2	0,22	2,470588235
FITC-D70	5,79	70	1,9	0,048	1,117647059
FITC-D150	9	150	0,3	NA	0,176470588

- ECM Diffusion vs Charge

Macromolecule	Size[nm]	Zeta Potenial [mV]	D [µm2/s]	D/Dwater
Liposome	165	-32	0,00005	0,00004
		-30	0,0001	0,00007
		-20	0,2	0,1489
		-15	0,2	0,1489
		0	0,15	0,11
		5	0,1	0,0745
		15	0,00002	0,00004

Table S2 - Data used to compute trends

It is worth noting that in the data for *ECM Diffusivity vs Charge* trend, the diffusion coefficient was computed from the analysis of the diffusion of liposomes in an ECM-mimicking hydrogel (*i.e.*, Matrigel), due to the lack of significant studies for diffusion of macromolecules in animal model to the best of our knowledge; moreover, the normalization was obtained by dividing for the free diffusion coefficient of liposomes in water, since a value of diffusion coefficient of liposomes in normal tissue was not available from the same study or from other relevant literature studies.

Viscosity computation for the generation of the trends

Viscosity of dextran is reported against the molecular weight of dextran from [133] (Fig. S3-(a)).
This allowed to plot the molecular weights of dextran, available in the studies of interest [129] and [131], as a function of the computed viscosity (Fig. S3-(b)), against the correspondent Vascular Permeability and ECM diffusivity, with the aim to obtain the trends *Vascular Permeability vs Viscosity* and *ECM Diffusion vs Viscosity* trends.

a)

Dextran MW [kDa]	Dextran viscosity [cP/mM]
10	0
20	0,25
40	0,65
70	1,56
148	4,4
260	7,9
500	15

b)

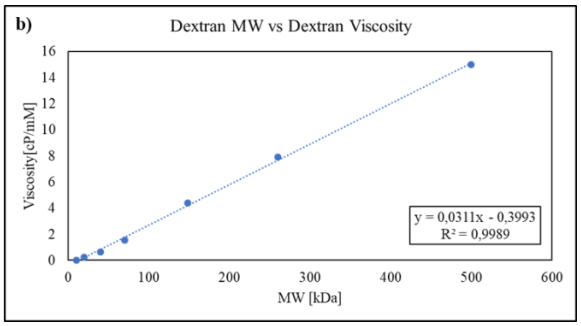

Figure S3 – Dextran viscosity at different MW (a); Dextran MW vs Dextran viscosity trend (b).

The data for the *Vascular Permeability vs Viscosity* and *ECM Diffusivity vs Viscosity* trends were subsequently computed, as explained before, and are reported in *Tab. S3*.

a)

Dextran MW [kDa]	Injected [mg]	Concentration [mg/ml]	Concentration [mM]	Viscosity [cP]	P/Pnormal(max)
10	0,5	0,5	0,05	0	7,881773399
40	0,5	0,5	0,0125	0,01055875	2,339901478
70	0,5	0,5	0,007142857	0,012697857	2,413793103
2000	0,5	0,5	0,00025	0,015450175	0,418719212

b)

Dextran MW [kDa]	Concentration [g/L]	Concentration [mM]	Viscosity [cP]	D/Dnormal(max)
20	2,5	0,125	0,0278375	4,411764706
40	2,5	0,0625	0,05279375	2,470588235
70	2,5	0,035714286	0,063489286	1,117647059
150	2,5	0,016666667	0,071095	0,176470588

Table S3 - Computation of dextran viscosity, P/Pnormal(max) (a), D/Dnormal(max) (b) at the concentration under analysis

The concentration was computed and the viscosity was derived subsequently as explained above, starting from the data about dextran concentration, available in the respective works [129] and [131].

Trends before two-step normalization strategy

Intermediate trends before the normalization for size, charge and viscosity were also computed and reported below (*Fig. S2*).

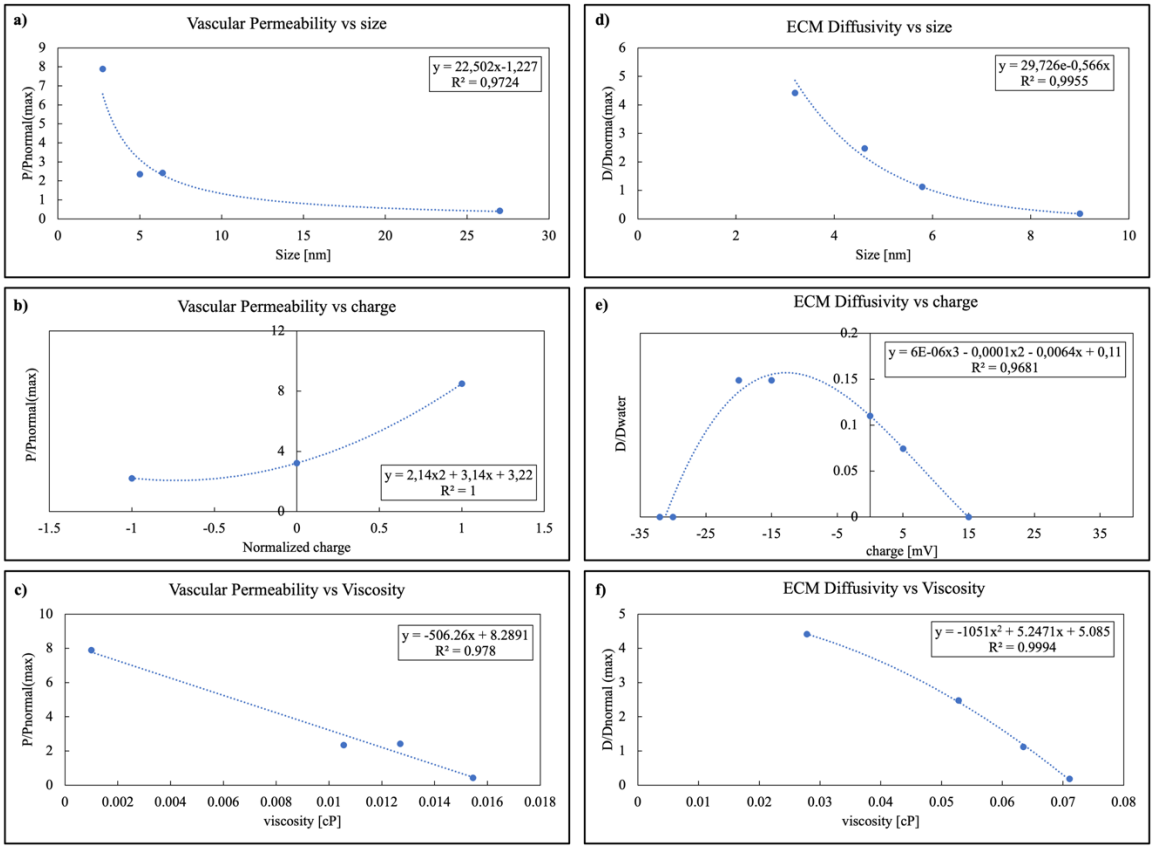

Figure S51 – Trends of Vascular Permeability (a-c) and ECM Diffusivity (d-f) before size, charge and viscosity normalization.

Models' implementation

Support Vector Machine (SVM) and Decision Tree (DT) classifiers

1. Data Preprocessing:
    - Numerical variables ('Size', 'Charge', 'Concentration') were standardized using the StandardScaler.
    - Categorical variables ('Material', 'Tumor') were one-hot encoded using the OneHotEncoder.
    - The ColumnTransformer was used to apply the appropriate preprocessing steps to the respective variable types.
2. Splitting the Dataset:
    - The dataset was divided into independent variables (X) and the dependent variable (y) which was to be predicted.
    - X consisted of columns 'Size', 'Charge', 'Material', 'Concentration', and 'Tumor', while y contained the values from column 'NDE'.
    - The train_test_split function from sklearn.model_selection was used to split the data into training and testing sets, with a test size of 20%.
3. Support Vector Machine (SVM) model:
    - An SVM classifier with a radial basis function (RBF) kernel was used.
    - The SVM classifier was trained on the training data using the fit method.
    - Predictions were made on the testing data using the predict method.
4. Decision Tree (DT) model:
    - A DT classifier with standard parameters was defined and used.
    - The DT classifier was trained on the training data using the fit method.
    - Predictions were made on the testing data using the predict method.
5. Models Evaluation:
    - Accuracy score, F1 Score, and the classification report were computed using appropriate functions from sklearn.metrics.

- The confusion matrix was calculated to analyze the number of correct and incorrect predictions for each class.
- Additionally, the receiver operating characteristic (ROC) curve and area under the curve (AUC) were plotted to visualize the models' performance.

6. Feature Importances:
   - Permutation importance was computed to determine the importance of each feature in the SVM model.
   - The permutation_importance function from sklearn.inspection was used, considering 10 repetitions.
   - The feature importances and feature names were obtained, sorted in descending order and a bar plot was created.
7. Cross-Validation:
   - Cross-validation was performed using the cross_val_score function from sklearn.model_selection with a specified number of folds (k=5), for both SVM and DT models.
   - The accuracy scores for each fold were computed, and the mean accuracy score was calculated.

Multi-Layer Perceptron Artificial Neural Network (MLP-ANN)

1. Data Preprocessing:
   - Numerical variables ('Size', 'Charge', 'Concentration') were standardized using the StandardScaler.
   - Categorical variables ('Material', 'Tumor') were one-hot encoded using the OneHotEncoder.
   - The ColumnTransformer was used to apply the appropriate preprocessing steps to the respective variable types.
2. Splitting the Dataset:
   - The dataset was divided into independent variables (X) and the dependent variable (y) which was to be predicted.
   - X consisted of columns 'Size', 'Charge', 'Material', 'Concentration', and 'Tumor', while y contained the values from column 'NDE'.

- The train_test_split function from sklearn.model selection was used to split the data into training and testing sets, with a test size of 20%.

3. Multi-Layer Perceptron Artificial Neural Network (MLP-ANN) model:
    - The MLP-ANN was constructed using the Sequential model, built in the Keras library (with a TensorFlow backend) allowing to stack multiple layers sequentially. It is composed by one input layer, two hidden layers, and one output layers hereby described.
    - Input layer has 8 nodes, one for each independent variable of the dataset.
    - The first hidden layer has 10 nodes, fully connected to the input layer and to the second hidden one, with ReLU activation function.
    - The second hidden layer has 5 nodes, fully connected to the first hidden layer and to the output one, with ReLU activation function.
    - The output layer has 3 nodes, one for each predicting class of the dependent variable set, with SoftMax activation function.
    - MLP-ANN was compiled selecting the Adam optimizer, spars categorical cross entropy as loss function, and accuracy as metrics.
    - The MLP-ANN was trained on the training data using the fit method, by selecting 100 epochs, and a batch size of 32.
    - Predictions were made on the testing data using the predict method.
4. Model Evaluation:
    - Accuracy score, F1 Score, and the classification report were computed using appropriate functions from sklearn.metrics.
    - The confusion matrix was calculated to analyze the number of correct and incorrect predictions for each class.
    - Additionally, the receiver operating characteristic (ROC) curve and area under the curve (AUC) were plotted to visualize the models' performance.
5. Feature Importances:
    - Feature Importances were computed directly from the weights of the MLP-ANN model, by calculating the absolute values of the mean.
    - The Feature Importances and feature names were obtained, sorted in descending order and a bar plot was created.

6. Cross-Validation:
    - Cross-validation was performed using the cross_val_score function from sklearn.model_selection with a specified number of folds (k=5).
    - The accuracy scores for each fold were computed, and the mean accuracy score was calculated.

6. Discussions and Conclusions

DDSs, in general, and nanoparticles are subjected to a series of biological barriers spanning across multiple scales, from protein corona formation, once injected in the blood, to margination towards blood vessels and consequently extravasation in tumor tissue, diffusion in ECM and interaction and uptake by tumor cells. The anatomical, mechanical, and fluido-dynamic properties of these barriers change extremely depending on the pathological conditions and on the patient; clinical parameters change according to the type of tumor and the patient's pathophysiological state. The changes in barriers encountered will determine different transport conditions to which nanoparticles are subjected and, subsequently, different *in vivo* interactions with organs, tissues, and cells in the body. This means that nanoparticle design should be meticulously and precisely informed by the patient and by the pathology. Clinical characterization of the barriers is nowadays performed through a series of techniques, with clinical imaging assessing as a powerful and reliable tool to extract the clinical parameters of interest that can instruct the design of DDSs. However, the availability of high-quality and artifacts-free images still represents an expanding and challenging field of interest. In this work we have, indeed, proposed two PET reconstruction algorithms that can improve the reconstruction and capturing of very small lung cancer lesions, with size comparable to PET scanner resolution which is a current challenge in the field. The algorithms seem to show improved performance with respect to the ones used in the current clinical practice, providing a clinically translatable tool for improving lung cancer early diagnosis, thus leading to an opportunity for the personalization of the treatment. Once clinical parameters are extracted and the tumor characterization is performed properly, we have identified pathophysiological features in two tumor case studies (*i.e.,* brain and breast tumors). The performed categorization and characterization of the biological barriers encountered by nanoparticles offer the possibility for a tailored design of the nanoparticles; as examples, it could be possible to modulate the size, shape or stiffness of the nanoparticles depending on the ECM porosity or tortuosity or to use different targeting strategies, depending on the ECM components or receptors overexpressed in the pathology addressed.

This makes clear that it is necessary to perform a thorough clinical characterization of the tumor to be able to inform *a-priori* the design and personalization of the nanoparticles' features.

However, understanding the effect of the combination of all the physicochemical properties of the nanoparticles on their biological identity *in vivo* and on their final clinical outcome, is still a major challenge for the clinical translation of personalized nanomedicine. Thus, it is necessary to match the synthetic and the biological identity of nanoparticles and modulate the design features of nanoparticles depending on the clinical case under consideration. In this sense, it is necessary to determine the *optimal design of nanoparticles* which is firmly responsible for effective immune system escape, effective margination and extravasation within the tumor tissue, diffusive penetration in tumor, cell targeting and uptake.

Firstly, we must rely on tools that allow us to finely adjust nanoparticle properties accordingly.

Microfluidics allows the production of different types of drug delivery systems (*from microparticles to nanoparticles*), depending on the clinical application of interest (*therapeutic, imaging or theranostic*), ranging

between different types of production processes (*in this work droplet generation and flow focusing are investigated*), different types of materials (*in this work we have selected PLGA and hyaluronic acid*) and different targeting properties.

In this sense, microfluidics is establishing as a tool through which it is possible to produce nanoparticles with a narrow size distribution, tunable physicochemical properties, and reliable batch-to-batch reproducibility, making possible to screen libraries of nanoparticles in parallel. Moreover, microfluidics allows to implement very complex principles, as *hydrodenticity* by tuning hydrogel properties and increasing the MR relaxivity boosting properties of the so produced nanoparticles. However, the scalability of nanoparticles production remains challenging, thus pushing towards the implementation of different methods and manufacturing procedures. In this work, Telos® has been investigated for the purpose, but showing that still some work needs to be done in this direction, especially when trying to "scale" complex principles such as *hydrodenticity*. Nonetheless, microfluidics shows its potential in finely tuning and modulating the synthetic identity of nanoparticles.

Secondly, we have collected data (*in vitro* and *in vivo*) and provided tools for the exploration and validation of biological identity of nanoparticles. In particular, our analysis of nanoparticles' penetration studies within hydrogels that mimic ECM of the tumor at different pathological degrees serves as preliminary step in demonstrating that features like size, material, and stiffness impact diffusion within the ECM and interaction with its components. While our initial analysis focuses on two types of nanoparticles, polystyrene and hyaluronic acid-based nanoparticles, our preliminary results show that there is the potential to test a wider library of nanoparticles and unravel relationships between the choice of some specific design features, like size, material and stiffness, and diffusion within ECM. This knowledge could facilitate the *a-priori* design of the nanoparticles, depending on the porosity and stiffness of the hydroscaffolds considered, which directly reflect and correlate the degree of the pathology.

While databases on clinical tumor characterization and nanomedicine exist, there is currently limited integration of data between them. This lack of integration becomes evident even when conducting *in vivo* studies on nanoparticle biodistribution, evidencing the absence of clinical characterization for the specific tumor models under examination.

Consequently, there is a clear absence of databases that aim to establish connections between nanoparticles' physicochemical properties and tumor characterization. This gap in scientific knowledge underlines the necessity to generate "synthetic data" to address this deficiency, by analyzing literature studies about vascular permeability and ECM diffusivity of macromolecules (*i.e.,* BSA, dextran, liposomes). We translate the insights from the collected studies into incorporating nanoparticles' features, specifically size, charge and stiffness, into transport equations that guide the extravasation of nanoparticles across vessel walls and diffusion within the tumor ECM. This has allowed to develop in this thesis work a preliminary model that, exploiting specific tumor parameters, can support in selecting the most suitable nanoparticle design for the particular tumor being analyzed, through machine learning and artificial intelligence techniques to the generated dataset. Moreover, this approach has showed how ML/AI can be incorporated in the shift from "one-size-fits-all" approach to

personalized nanomedicine. To achieve this, we foresee the multiple disciplinary fields' collaboration, the standardization in collecting data, and conducting in vitro and/or in vivo nanoparticle analysis.

References

(1) Wilhelm, S.; Tavares, A. J.; Dai, Q.; Ohta, S.; Audet, J.; Dvorak, H. F.; Chan, W. C. W. Analysis of nanoparticle delivery to tumours. *Nature Reviews Materials* **2016**, *1* (5). DOI: 10.1038/natrevmats.2016.14.
(2) Karageorgis, A.; Dufort, S.; Sancey, L.; Henry, M.; Hirsjarvi, S.; Passirani, C.; Benoit, J. P.; Gravier, J.; Texier, I.; Montigon, O.; et al. An MRI-based classification scheme to predict passive access of 5 to 50-nm large nanoparticles to tumors. *Scientific Reports* **2016**, *6*. DOI: 10.1038/srep21417.
(3) Sykes, E. A.; Dai, Q.; Sarsons, C. D.; Chen, J.; Rocheleau, J. V.; Hwang, D. M.; Zheng, G.; Cramb, D. T.; Rinker, K. D.; Chan, W. C. W. Tailoring nanoparticle designs to target cancer based on tumor pathophysiology. *Proceedings of the National Academy of Sciences of the United States of America* **2016**, *113* (9), E1142-E1151. DOI: 10.1073/pnas.1521265113.
(4) Mirkin, C. Exploration of the nanomedicine-design space with high-throughput screening and machine learning. *Abstracts of Papers of the American Chemical Society* **2019**, *258*.
(5) Zhao, Z. M.; Ukidve, A.; Kim, J.; Mitragotri, S. Targeting Strategies for Tissue-Specific Drug Delivery. *Cell* **2020**, *181* (1), 151-167. DOI: 10.1016/j.cell.2020.02.001.
(6) Blanco, E.; Shen, H.; Ferrari, M. Principles of nanoparticle design for overcoming biological barriers to drug delivery. *Nature Biotechnology* **2015**, *33* (9), 941-951. DOI: 10.1038/nbt.3330.
(7) Lane, L. A. Physics in nanomedicine: Phenomena governing the in vivo performance of nanoparticles. *Applied Physics Reviews* **2020**, *7* (1). DOI: 10.1063/1.5052455.
(8) Jain, R. K.; Stylianopoulos, T. Delivering nanomedicine to solid tumors. *Nature Reviews Clinical Oncology* **2010**, *7* (11), 653-664. DOI: 10.1038/nrclinonc.2010.139.
(9) Stylianopoulos, T.; Munn, L. L.; Jain, R. K. Reengineering the Physical Microenvironment of Tumors to Improve Drug Delivery and Efficacy: From Mathematical Modeling to Bench to Bedside. *Trends in Cancer* **2018**, *4* (4), 292-319. DOI: 10.1016/j.trecan.2018.02.005.
(10) Chauhan, V. P.; Stylianopoulos, T.; Boucher, Y.; Jain, R. K. Delivery of Molecular and Nanoscale Medicine to Tumors: Transport Barriers and Strategies. *Annual Review of Chemical and Biomolecular Engineering, Vol 2* **2011**, *2*, 281-298. DOI: 10.1146/annurev-chembioeng-061010-114300.
(11) Garcia-Figueiras, R.; Baleato-Gonzalez, S.; Padhani, A. R.; Luna-Alcala, A.; Vallejo-Casas, J. A.; Sala, E.; Vilanova, J. C.; Koh, D. M.; Herranz-Carnero, M.; Vargas, H. A. How clinical imaging can assess cancer biology. *Insights into Imaging* **2019**, *10* (1). DOI: 10.1186/s13244-019-0703-0.
(12) Li, X. G.; Zhu, Y. S.; Kang, H. Y.; Zhang, Y. L.; Liang, H. P.; Wang, S. M.; Zhang, W. G. Glioma grading by microvascular permeability parameters derived from dynamic contrast-enhanced MRI and intratumoral susceptibility signal on susceptibility weighted imaging. *Cancer Imaging* **2015**, *15*. DOI: 10.1186/s40644-015-0039-z.
(13) Chang, J. M.; Moon, W. K.; Cho, N.; Park, J. S.; Kim, S. J. Radiologists' performance in the detection of benign and malignant masses with 3D automated breast ultrasound (ABUS). *European Journal of Radiology* **2011**, *78* (1), 99-103. DOI: 10.1016/j.ejrad.2011.01.074.
(14) Jensen, J. H.; Helpern, J. A. MRI quantification of non-Gaussian water diffusion by kurtosis analysis. *Nmr in Biomedicine* **2010**, *23* (7), 698-710. DOI: 10.1002/nbm.1518.
(15) Chauvet, D.; Imbault, M.; Capelle, L.; Demene, C.; Mossad, M.; Karachi, C.; Boch, A. L.; Gennisson, J. L.; Tanter, M. In Vivo Measurement of Brain Tumor Elasticity Using Intraoperative Shear Wave Elastography. *Ultraschall in Der Medizin* **2016**, *37* (6), 584-590. DOI: 10.1055/s-0034-1399152.
(16) Zaccagna, F.; Riemer, F.; Priest, A. N.; McLean, M. A.; Allinson, K.; Grist, J. T.; Dragos, C.; Matys, T.; Gillard, J. H.; Watts, C.; et al. Non-invasive assessment of glioma microstructure using VERDICT MRI: correlation with histology. *European Radiology* **2019**, *29* (10), 5559-5566. DOI: 10.1007/s00330-019-6011-8.
(17) Choi, S. Y.; Chang, Y. W.; Park, H. J.; Kim, H. J.; Hong, S. S.; Seo, D. Y. Correlation of the apparent diffusion coefficiency values on diffusion-weighted imaging with prognostic factors for breast cancer. *British Journal of Radiology* **2012**, *85* (1016), E474-E479. DOI: 10.1259/bjr/79381464.

(18) Samani, A.; Zubovits, J.; Plewes, D. Elastic moduli of normal and pathological human breast tissues: an inversion-technique-based investigation of 169 samples. *Physics in Medicine and Biology* **2007**, *52* (6), 1565-1576. DOI: 10.1088/0031-9155/52/6/002.
(19) Jahn, A.; Vreeland, W. N.; Gaitan, M.; Locascio, L. E. Controlled vesicle self-assembly in microfluidic channels with hydrodynamic focusing. *Journal of the American Chemical Society* **2004**, *126* (9), 2674-2675. DOI: 10.1021/ja0318030.
(20) Dammes, N.; Peer, D. Paving the Road for RNA Therapeutics. *Trends in Pharmacological Sciences* **2020**, *41* (10), 755-775. DOI: 10.1016/j.tips.2020.08.004.
(21) Lee, S. W. L.; Paoletti, C.; Campisi, M.; Osaki, T.; Adriani, G.; Kamm, R. D.; Mattu, C.; Chiono, V. MicroRNA delivery through nanoparticles. *Journal of Controlled Release* **2019**, *313*, 80-95. DOI: 10.1016/j.jconrel.2019.10.007.
(22) Kauffman, K. J.; Dorkin, J. R.; Yang, J. H.; Heartlein, M. W.; DeRosa, F.; Mir, F. F.; Fenton, O. S.; Anderson, D. G. Optimization of Lipid Nanoparticle Formulations for mRNA Delivery in Vivo with Fractional Factorial and Definitive Screening Designs. *Nano Letters* **2015**, *15* (11), 7300-7306. DOI: 10.1021/acs.nanolett.5b02497.
(23) Kotoucek, J.; Hubatka, F.; Masek, J.; Kulich, P.; Velinska, K.; Bezdekova, J.; Fojtikova, M.; Bartheldyova, E.; Tomeckova, A.; Straska, J.; et al. Preparation of nanoliposomes by microfluidic mixing in herring-bone channel and the role of membrane fluidity in liposomes formation. *Scientific Reports* **2020**, *10* (1). DOI: 10.1038/s41598-020-62500-2.
(24) Weaver, E.; O'Connor, E.; Cole, D. K.; Hooker, A.; Uddin, S.; Lamprou, D. A. Microfluidic-mediated self-assembly of phospholipids for the delivery of biologic molecules. *International Journal of Pharmaceutics* **2022**, *611*. DOI: 10.1016/j.ijpharm.2021.121347.
(25) Muller, R. H.; Keck, C. M. Challenges and solutions for the delivery of biotech drugs - a review of drug nanocrystal technology and lipid nanoparticles. *Journal of Biotechnology* **2004**, *113* (1-3), 151-170. DOI: 10.1016/j.jbiotec.2004.06.007.
(26) Ran, R.; Middelberg, A. P. J.; Zhao, C. X. Microfluidic synthesis of multifunctional liposomes for tumour targeting. *Colloids and Surfaces B-Biointerfaces* **2016**, *148*, 402-410. DOI: 10.1016/j.colsurfb.2016.09.016.
(27) Karnik, R.; Gu, F.; Basto, P.; Cannizzaro, C.; Dean, L.; Kyei-Manu, W.; Langer, R.; Farokhzad, O. C. Microfluidic platform for controlled synthesis of polymeric nanoparticles. *Nano Letters* **2008**, *8* (9), 2906-2912. DOI: 10.1021/nl801736q.
(28) Ali, H. S. M.; York, P.; Blagden, N. Preparation of hydrocortisone nanosuspension through a bottom-up nanoprecipitation technique using microfluidic reactors. *International Journal of Pharmaceutics* **2009**, *375* (1-2), 107-113. DOI: 10.1016/j.ijpharm.2009.03.029.
(29) Ali, H. S. M.; Blagden, N.; York, P.; Amani, A.; Brook, T. Artificial neural networks modelling the prednisolone nanoprecipitation in microfluidic reactors. *European Journal of Pharmaceutical Sciences* **2009**, *37* (3-4), 514-522. DOI: 10.1016/j.ejps.2009.04.007.
(30) Wang, J. X.; Zhang, Q. X.; Zhou, Y.; Shao, L.; Chen, J. F. Microfluidic synthesis of amorphous cefuroxime axetil nanoparticles with size-dependent and enhanced dissolution rate. *Chemical Engineering Journal* **2010**, *162* (2), 844-851. DOI: 10.1016/j.cej.2010.06.022.
(31) Capretto, L.; Cheng, W.; Carugo, D.; Katsamenis, O. L.; Hill, M.; Zhang, X. L. Mechanism of co-nanoprecipitation of organic actives and block copolymers in a microfluidic environment. *Nanotechnology* **2012**, *23* (37). DOI: 10.1088/0957-4484/23/37/375602.
(32) de Solorzano, I. O.; Uson, L.; Larrea, A.; Miana, M.; Sebastian, V.; Arruebo, M. Continuous synthesis of drug-loaded nanoparticles using microchannel emulsification and numerical modeling: effect of passive mixing. *International Journal of Nanomedicine* **2016**, *11*, 3397-3416. DOI: 10.2147/ijn.s108812.
(33) Morikawa, Y.; Tagami, T.; Hoshikawa, A.; Ozeki, T. The Use of an Efficient Microfluidic Mixing System for Generating Stabilized Polymeric Nanoparticles for Controlled Drug Release. *Biological & Pharmaceutical Bulletin* **2018**, *41* (6), 899-907. DOI: 10.1248/bpb.b17-01036.
(34) Roces, C. B.; Christensen, D.; Perrie, Y. Translating the fabrication of protein-loaded poly(lactic-co-glycolic acid) nanoparticles from bench to scale-independent production using microfluidics. *Drug Delivery and Translational Research* **2020**, *10* (3), 582-593. DOI: 10.1007/s13346-019-00699-y.
(35) Abstiens, K.; Goepferich, A. M. Microfluidic manufacturing improves polydispersity of multicomponent polymeric nanoparticles. *Journal of Drug Delivery Science and Technology* **2019**, *49*, 433-439. DOI: 10.1016/j.jddst.2018.12.009.

(36) Valencia, P. M.; Pridgen, E. M.; Rhee, M.; Langer, R.; Farokhzad, O. C.; Karnik, R. Microfluidic Platform for Combinatorial Synthesis and Optimization of Targeted Nanoparticles for Cancer Therapy. *Acs Nano* **2013**, *7* (12), 10671-10680. DOI: 10.1021/nn403370e.
(37) Chifiriuc, M. C.; Grumezescu, A. M.; Grumezescu, V.; Bezirtzoglou, E.; Lazar, V.; Bolocan, A. Biomedical Applications of Natural Polymers for Drug Delivery. *Current Organic Chemistry* **2014**, *18* (2), 152-164. DOI: 10.2174/13852728180214012910452 5.
(38) George, A.; Shah, P. A.; Shrivastav, P. S. Natural biodegradable polymers based nano-formulations for drug delivery: A review. *International Journal of Pharmaceutics* **2019**, *561*, 244-264. DOI: 10.1016/j.ijpharm.2019.03.011.
(39) Russo, M.; Bevilacqua, P.; Netti, P. A.; Torino, E. A Microfluidic Platform to design crosslinked Hyaluronic Acid Nanoparticles (cHANPs) for enhanced MRI. *Scientific Reports* **2016**, *6*. DOI: 10.1038/srep37906.
(40) Smeraldo, A.; Ponsiglione, A. M.; Netti, P. A.; Torino, E. Tuning of Hydrogel Architectures by Ionotropic Gelation in Microfluidics: Beyond Batch Processing to Multimodal Diagnostics. *Biomedicines* **2021**, *9* (11). DOI: 10.3390/biomedicines9111551.
(41) Dashtimoghadam, E.; Mirzadeh, H.; Taromi, F. A.; Nystrom, B. Microfluidic self-assembly of polymeric nanoparticles with tunable compactness for controlled drug delivery. *Polymer* **2013**, *54* (18), 4972-4979. DOI: 10.1016/j.polymer.2013.07.022.
(42) Rhee, M.; Valencia, P. M.; Rodriguez, M. I.; Langer, R.; Farokhzad, O. C.; Karnik, R. Synthesis of Size-Tunable Polymeric Nanoparticles Enabled by 3D Hydrodynamic Flow Focusing in Single-Layer Microchannels. *Advanced Materials* **2011**, *23* (12), H79-H83. DOI: 10.1002/adma.201004333.
(43) Lim, J. M.; Swami, A.; Gilson, L. M.; Chopra, S.; Choi, S.; Wu, J.; Langer, R.; Karnik, R.; Farokhzad, O. C. Ultra-High Throughput Synthesis of Nanoparticles with Homogeneous Size Distribution Using a Coaxial Turbulent Jet Mixer. *Acs Nano* **2014**, *8* (6), 6056-6065. DOI: 10.1021/nn501371n.
(44) Hood, R. R.; DeVoe, D. L.; Atencia, J.; Vreeland, W. N.; Omiatek, D. M. A facile route to the synthesis of monodisperse nanoscale liposomes using 3D microfluidic hydrodynamic focusing in a concentric capillary array. *Lab on a Chip* **2014**, *14* (14), 2403-2409. DOI: 10.1039/c4lc00334a.
(45) Capretto, L.; Cheng, W.; Hill, M.; Zhang, X. L. Micromixing Within Microfluidic Devices. *Microfluidics: Technologies and Applications* **2011**, *304*, 27-68. DOI: 10.1007/128_2011_150.
(46) Belliveau, N. M.; Huft, J.; Lin, P. J. C.; Chen, S.; Leung, A. K. K.; Leaver, T. J.; Wild, A. W.; Lee, J. B.; Taylor, R. J.; Tam, Y. K.; et al. Microfluidic Synthesis of Highly Potent Limit-size Lipid Nanoparticles for In Vivo Delivery of siRNA. *Molecular Therapy-Nucleic Acids* **2012**, *1*. DOI: 10.1038/mtna.2012.28.
(47) Zhigaltsev, I. V.; Belliveau, N.; Hafez, I.; Leung, A. K. K.; Huft, J.; Hansen, C.; Cullis, P. R. Bottom-Up Design and Synthesis of Limit Size Lipid Nanoparticle Systems with Aqueous and Triglyceride Cores Using Millisecond Microfluidic Mixing. *Langmuir* **2012**, *28* (7), 3633-3640. DOI: 10.1021/la204833h.
(48) Quagliarini, E.; Renzi, S.; Digiacomo, L.; Giulimondi, F.; Sartori, B.; Amenitsch, H.; Tassinari, V.; Masuelli, L.; Bei, R.; Cui, L. S.; et al. Microfluidic Formulation of DNA-Loaded Multicomponent Lipid Nanoparticles for Gene Delivery. *Pharmaceutics* **2021**, *13* (8). DOI: 10.3390/pharmaceutics13081292.
(49) Terada, T.; Kulkarni, J. A.; Huynh, A.; Chen, S.; van der Meel, R.; Tam, Y. Y. C.; Cullis, P. R. Characterization of Lipid Nanoparticles Containing Ionizable Cationic Lipids Using Design-of-Experiments Approach. *Langmuir* **2021**, *37* (3), 1120-1128. DOI: 10.1021/acs.langmuir.0c03039.
(50) Evers, M. J. W.; Kulkarni, J. A.; van der Meel, R.; Cullis, P. R.; Vader, P.; Schiffelers, R. M. State-of-the-Art Design and Rapid-Mixing Production Techniques of Lipid Nanoparticles for Nucleic Acid Delivery. *Small Methods* **2018**, *2* (9). DOI: 10.1002/smtd.201700375.
(51) Krzyszton, R.; Salem, B.; Lee, D. J.; Schwake, G.; Wagner, E.; Radler, J. O. Microfluidic self-assembly of folate-targeted monomolecular siRNA-lipid nanoparticles. *Nanoscale* **2017**, *9* (22), 7442-7453. DOI: 10.1039/c7nr01593c.
(52) Hong, J. S.; Stavis, S. M.; Lacerda, S. H. D.; Locascio, L. E.; Raghavan, S. R.; Gaitan, M. Microfluidic Directed Self-Assembly of Liposome-Hydrogel Hybrid Nanoparticles. *Langmuir* **2010**, *26* (13), 11581-11588. DOI: 10.1021/la100879p.
(53) Valencia, P. M.; Basto, P. A.; Zhang, L. F.; Rhee, M.; Langer, R.; Farokhzad, O. C.; Karnik, R. Single-Step Assembly of Homogenous Lipid - Polymeric and Lipid - Quantum Dot Nanoparticles Enabled by Microfluidic Rapid Mixing. *Acs Nano* **2010**, *4* (3), 1671-1679. DOI: 10.1021/nn901433u.
(54) Roffo, F.; Ponsiglione, A. M.; Netti, P. A.; Torino, E. coupled Hydrodynamic Flow Focusing (cHFF) to Engineer Lipid-Polymer Nanoparticles (LiPoNs) for Multimodal Imaging and Theranostic Applications. *Biomedicines* **2022**, *10* (2). DOI: 10.3390/biomedicines10020438.

(55) Sun, J. S.; Zhang, L.; Wang, J. L.; Feng, Q.; Liu, D. B.; Yin, Q. F.; Xu, D. Y.; Wei, Y. J.; Ding, B. Q.; Shi, X. H.; et al. Tunable Rigidity of (Polymeric Core)-(Lipid Shell) Nanoparticles for Regulated Cellular Uptake. *Advanced Materials* **2015**, *27* (8), 1402-+. DOI: 10.1002/adma.201404788.
(56) Lussier, F.; Staufer, O.; Platzman, I.; Spatz, J. P. Can Bottom-Up Synthetic Biology Generate Advanced Drug-Delivery Systems? *Trends in Biotechnology* **2021**, *39* (5), 445-459. DOI: 10.1016/j.tibtech.2020.08.002.
(57) Diltemiz, S. E.; Tavafoghi, M.; de Barros, N. R.; Kanada, M.; Heinamaki, J.; Contag, C.; Seidlits, S. K.; Ashammakhi, N. Use of artificial cells as drug carriers. *Materials Chemistry Frontiers* **2021**, *5* (18), 6672-6692. DOI: 10.1039/d1qm00717c.
(58) Elani, Y.; Trantidou, T.; Wylie, D.; Dekker, L.; Polizzi, K.; Law, R. V.; Ces, O. Constructing vesicle-based artificial cells with embedded living cells as organelle-like modules. *Scientific Reports* **2018**, *8*. DOI: 10.1038/s41598-018-22263-3.
(59) Yandrapalli, N.; Petit, J.; Baumchen, O.; Robinson, T. Surfactant-free production of biomimetic giant unilamellar vesicles using PDMS-based microfluidics. *Communications Chemistry* **2021**, *4* (1). DOI: 10.1038/s42004-021-00530-1.
(60) Deng, N. N.; Huck, W. T. S. Microfluidic Formation of Monodisperse Coacervate Organelles in Liposomes. *Angewandte Chemie-International Edition* **2017**, *56* (33), 9736-9740. DOI: 10.1002/anie.201703145.
(61) Ugrinic, M.; Zambrano, A.; Berger, S.; Mann, S.; Tang, T. Y. D.; Demello, A. Microfluidic formation of proteinosomes. *Chemical Communications* **2018**, *54* (3), 287-290. DOI: 10.1039/c7cc08466h.
(62) Scott, R. C.; Crabbe, D.; Krynska, B.; Ansari, R.; Kiani, M. F. Aiming for the heart: targeted delivery of drugs to diseased cardiac tissue. *Expert Opinion on Drug Delivery* **2008**, *5* (4), 459-470. DOI: 10.1517/17425247.5.4.459.
(63) Kapoor, D. N.; Bhatia, A.; Kaur, R.; Sharma, R.; Kaur, G.; Dhawan, S. PLGA: a unique polymer for drug delivery. *Therapeutic Delivery* **2015**, *6* (1), 41-58. DOI: 10.4155/tde.14.91.
(64) Soppimath, K. S.; Aminabhavi, T. M. Ethyl acetate as a dispersing solvent in the production of poly(DL-lactide-co-glycolide) microspheres: effect of process parameters and polymer type. *Journal of Microencapsulation* **2002**, *19* (3), 281-292. DOI: 10.1080/02652040110105319.
(65) Lagreca, E.; Onesto, V.; Di Natale, C.; La Manna, S.; Netti, P. A.; Vecchione, R. Recent advances in the formulation of PLGA microparticles for controlled drug delivery. *Progress in Biomaterials* **2020**, *9* (4), 153-174. DOI: 10.1007/s40204-020-00139-y.
(66) Khunmanee, S.; Jeong, Y.; Park, H. Crosslinking method of hyaluronic-based hydrogel for biomedical applications. *Journal of Tissue Engineering* **2017**, *8*. DOI: 10.1177/2041731417726464.
(67) Morneau, D. Droplet-based microfluidics. *Nature Reviews Methods Primers* **2023**, *3* (1). DOI: 10.1038/s43586-023-00224-z.
(68) Zhu, P. A.; Wang, L. Q. Passive and active droplet generation with microfluidics: a review. *Lab on a Chip* **2017**, *17* (1), 34-75. DOI: 10.1039/c6lc01018k.
(69) Russo, M.; Ponsiglione, A. M.; Forte, E.; Netti, P. A.; Torino, E. Hydrodenticity to enhance relaxivity of gadolinium-DTPA within crosslinked hyaluronic acid nanoparticles. *Nanomedicine* **2017**, *12* (18), 2199-2210. DOI: 10.2217/nnm-2017-0098.
(70) Choi, Y.; Hong, S. Qualitative and quantitative analysis of patent data in nanomedicine for bridging the gap between research activities and practical applications. *World Patent Information* **2020**, *60*. DOI: 10.1016/j.wpi.2019.101943.
(71) Bhutani, P.; Joshi, G.; Raja, N.; Bachhav, N.; Rajanna, P. K.; Bhutani, H.; Paul, A. T.; Kumar, R. US FDA Approved Drugs from 2015-June 2020: A Perspective. *Journal of Medicinal Chemistry* **2021**, *64* (5), 2339-2381. DOI: 10.1021/acs.jmedchem.0c01786.
(72) Bobo, D.; Robinson, K. J.; Islam, J.; Thurecht, K. J.; Corrie, S. R. Nanoparticle-Based Medicines: A Review of FDA-Approved Materials and Clinical Trials to Date. *Pharmaceutical Research* **2016**, *33* (10), 2373-2387. DOI: 10.1007/s11095-016-1958-5.
(73) Poon, W.; Kingston, B. R.; Ouyang, B.; Ngo, W.; Chan, W. C. W. A framework for designing delivery systems. *Nature Nanotechnology* **2020**, *15* (10), 819-829. DOI: 10.1038/s41565-020-0759-5.
(74) Yan, X. L.; Sedykh, A.; Wang, W. Y.; Yan, B.; Zhu, H. Construction of a web-based nanomaterial database by big data curation and modeling friendly nanostructure annotations. *Nature Communications* **2020**, *11* (1). DOI: 10.1038/s41467-020-16413-3.
(75) Panneerselvam, S.; Choi, S. Nanoinformatics: Emerging Databases and Available Tools. *International Journal of Molecular Sciences* **2014**, *15* (5), 7158-7182. DOI: 10.3390/ijms15057158.

(76) Puzyn, T.; Rasulev, B.; Gajewicz, A.; Hu, X. K.; Dasari, T. P.; Michalkova, A.; Hwang, H. M.; Toropov, A.; Leszczynska, D.; Leszczynski, J. Using nano-QSAR to predict the cytotoxicity of metal oxide nanoparticles. *Nature Nanotechnology* **2011**, *6* (3), 175-178. DOI: 10.1038/nnano.2011.10.
(77) Baharifar, H.; Amani, A. Cytotoxicity of chitosan/streptokinase nanoparticles as a function of size: An artificial neural networks study. *Nanomedicine-Nanotechnology Biology and Medicine* **2016**, *12* (1), 171-180. DOI: 10.1016/j.nano.2015.09.002.
(78) Cenk, N.; Budak, G.; Dayanik, S.; Sabuncuoglu, I. Artificial Neural Network Modeling and Simulation of In-Vitro Nanoparticle-Cell Interactions. *Journal of Computational and Theoretical Nanoscience* **2014**, *11* (1), 272-282. DOI: 10.1166/jctn.2014.3348.
(79) Ban, Z.; Yuan, P.; Yu, F. B.; Peng, T.; Zhou, Q. X.; Hu, X. G. Machine learning predicts the functional composition of the protein corona and the cellular recognition of nanoparticles. *Proceedings of the National Academy of Sciences of the United States of America* **2020**, *117* (19), 10492-10499. DOI: 10.1073/pnas.1919755117.
(80) Mulhopt, S.; Diabate, S.; Dilger, M.; Adelhelm, C.; Anderlohr, C.; Bergfeldt, T.; de la Torre, J. G.; Jiang, Y. H.; Valsami-Jones, E.; Langevin, D.; et al. Characterization of Nanoparticle Batch-To-Batch Variability. *Nanomaterials* **2018**, *8* (5). DOI: 10.3390/nano8050311.
(81) Soleimani, S.; Hasani-Sadrabadi, M. M.; Majedid, F. S.; Dashtimoghadam, E.; Tondar, M.; Jacob, K. I. Understanding biophysical behaviours of microfluidic-synthesized nanoparticles at nano-biointerface. *Colloids and Surfaces B-Biointerfaces* **2016**, *145*, 802-811. DOI: 10.1016/j.colsurfb.2016.06.002.
(82) Leung, M. H. M.; Shen, A. Q. Microfluidic Assisted Nanoprecipitation of PLGA Nanoparticles for Curcumin Delivery to Leukemia Jurkat Cells. *Langmuir* **2018**, *34* (13), 3961-3970. DOI: 10.1021/acs.langmuir.7b04335.
(83) Sun, J. S.; Xianyu, Y. L.; Li, M. M.; Liu, W. W.; Zhang, L.; Liu, D. B.; Liu, C.; Hu, G. Q.; Jiang, X. Y. A microfluidic origami chip for synthesis of functionalized polymeric nanoparticles. *Nanoscale* **2013**, *5* (12), 5262-5265. DOI: 10.1039/c3nr01289a.
(84) Cao, Y. M.; Silverman, L.; Lu, C. H.; Hof, R.; Wulff, J. E.; Moffitt, M. G. Microfluidic Manufacturing of SN-38-Loaded Polymer Nanoparticles with Shear Processing Control of Drug Delivery Properties. *Molecular Pharmaceutics* **2019**, *16* (1), 96-107. DOI: 10.1021/acs.molpharmaceut.8b00874.
(85) Feng, Q.; Zhang, L.; Liu, C.; Li, X. Y.; Hu, G. Q.; Sun, J. S.; Jiang, X. Y. Microfluidic based high throughput synthesis of lipid-polymer hybrid nanoparticles with tunable diameters. *Biomicrofluidics* **2015**, *9* (5). DOI: 10.1063/1.4922957.
(86) Zhu, M. Z.; Whittaker, A. K.; Jiang, X. Y.; Tang, R. P.; Li, X. Y.; Xu, W. Z.; Fu, C. K.; Smith, M. T.; Han, F. Y. Use of Microfluidics to Fabricate Bioerodable Lipid Hybrid Nanoparticles Containing Hydromorphone or Ketamine for the Relief of Intractable Pain. *Pharmaceutical Research* **2020**, *37* (10). DOI: 10.1007/s11095-020-02939-0.
(87) Martin-Banderas, L.; Saez-Fernandez, E.; Holgado, M. A.; Duran-Lobato, M. M.; Prados, J. C.; Melguizo, C.; Arias, J. L. Biocompatible gemcitabine-based nanomedicine engineered by Flow Focusing (R) for efficient antitumor activity. *International Journal of Pharmaceutics* **2013**, *443* (1-2), 103-109. DOI: 10.1016/j.ijpharm.2012.12.048.
(88) Ran, R.; Wang, H. F.; Liu, Y.; Hui, Y.; Sun, Q.; Seth, A.; Wibowo, D.; Chen, D.; Zhao, C. X. Microfluidic self-assembly of a combinatorial library of single- and dual-ligand liposomes for in vitro and in vivo tumor targeting. *European Journal of Pharmaceutics and Biopharmaceutics* **2018**, *130*, 1-10. DOI: 10.1016/j.ejpb.2018.06.017.
(89) Kimura, N.; Maeki, M.; Sato, Y.; Note, Y.; Ishida, A.; Tani, H.; Harashima, H.; Tokeshi, M. Development of the iLiNP Device: Fine Tuning the Lipid Nanoparticle Size within 10 nm for Drug Delivery. *Acs Omega* **2018**, *3* (5), 5044-5051. DOI: 10.1021/acsomega.8b00341.
(90) Feng, Q.; Liu, J. P.; Li, X. Y.; Chen, Q. H.; Sun, J. S.; Shi, X. H.; Ding, B. Q.; Yu, H. J.; Li, Y. P.; Jiang, X. Y. One-Step Microfluidic Synthesis of Nanocomplex with Tunable Rigidity and Acid-Switchable Surface Charge for Overcoming Drug Resistance. *Small* **2017**, *13* (9). DOI: 10.1002/smll.201603109.
(91) Rong, J. Y.; He, Y.; Tang, J. J.; Qiao, R. X.; Lin, S. J. "Fishing" nano-bio interactions at the key biological barriers. *Nanoscale* **2021**, *13* (12), 5954-5964. DOI: 10.1039/d1nr00328c.
(92) Lopez-Otin, C.; Kroemer, G. Hallmarks of Health. *Cell* **2021**, *184* (1), 33-63. DOI: 10.1016/j.cell.2020.11.034.
(93) Cirillo, D.; Valencia, A. Big data analytics for personalized medicine. *Current Opinion in Biotechnology* **2019**, *58*, 161-167. DOI: 10.1016/j.copbio.2019.03.004.

(94) Hood, R. R.; Vreeland, W. N.; DeVoe, D. L. Microfluidic remote loading for rapid single-step liposomal drug preparation. *Lab on a Chip* **2014**, *14* (17), 3359-3367. DOI: 10.1039/c4lc00390j.
(95) Gomez, L.; Sebastian, V.; Irusta, S.; Ibarra, A.; Arruebo, M.; Santamaria, J. Scaled-up production of plasmonic nanoparticles using microfluidics: from metal precursors to functionalized and sterilized nanoparticles. *Lab on a Chip* **2014**, *14* (2), 325-332. DOI: 10.1039/c3lc50999k.
(96) Knapp, K. A.; Nickels, M. L.; Manning, H. C. The Current Role of Microfluidics in Radiofluorination Chemistry. *Molecular Imaging and Biology* **2020**, *22* (3), 463-475. DOI: 10.1007/s11307-019-01414-6.
(97) Ovdiichuk, O.; Mallapura, H.; Pineda, F.; Hourtane, V.; Langstrom, B.; Halldin, C.; Nag, S.; Maskali, F.; Karcher, G.; Collet, C. Implementation of iMiDEV (TM), a new fully automated microfluidic platform for radiopharmaceutical production. *Lab on a Chip* **2021**, *21* (11), 2272-2282. DOI: 10.1039/d1lc00148e.
(98) Cece, E.; Meyrat, P.; Torino, E.; Verdier, O.; Colarieti-Tosti, M. Spatio-Temporal Positron Emission Tomography Reconstruction with Attenuation and Motion Correction. In *Journal of Imaging*, 2023; Vol. 9.
(99) BERNARD BENDRIEM, D. W. T. The Theory and Practice of 3D PET SPRINGER-SCIENCE+BUSINESS MEDIA, B.V.: 2003; pp 5-34.
(100) A. K. Shukla, U. K. Positron emission tomography: An overview. Journal of Medical Physics: 2006; Vol. 31.
(101) Ullah, M. N.; Pratiwi, E.; Cheon, J.; Choi, H.; Yeom, J. Y. Instrumentation for Time-of-Flight Positron Emission Tomography. *Nuclear Medicine and Molecular Imaging* **2016**, *50* (2), 112-122. DOI: 10.1007/s13139-016-0401-5.
(102) Nuyts, L.; Rezaei, A.; Defrise, M. ML-reconstruction for TOF-PET with simultaneous estimation of the attenuation factors. In *IEEE Nuclear Science Symposium / Medical Imaging Conference Record (NSS/MIC) / 19th Room-Temperature Semiconductor X-ray and Gamma-ray Detector Workshop*, Anaheim, CA, Oct 29-Nov 03, 2012; 2012; pp 2147-2149.
(103) Rezaei, A.; Nuyts, J.; Ieee. Simultaneous Reconstruction of the Activity Image and Registration of the CT Image in TOF-PET. In *60th IEEE Nuclear Science Symposium (NSS) / Medical Imaging Conference (MIC) / 20th International Workshop on Room-Temperature Semiconductor X-ray and Gamma-ray Detectors*, Seoul, SOUTH KOREA, Oct 27-Nov 02, 2013; 2013.
(104) Oktem, O.; Pouchol, C.; Verdier, O. Spatiotemporal PET Reconstruction Using ML-EM with Learned Diffeomorphic Deformation. *Machine Learning for Medical Image Reconstruction, Mlmir 2019* **2019**, *11905*, 151-162. DOI: 10.1007/978-3-030-33843-5_14.
(105) Ovtchinnikov, E.; Brown, R.; Kolbitsch, C.; Pasca, E.; da Costa-Luis, C.; Gillman, A. G.; Thomas, B. A.; Efthimiou, N.; Mayer, J.; Wadhwa, P.; et al. SIRF: Synergistic Image Reconstruction Framework. *Computer Physics Communications* **2020**, *249*. DOI: 10.1016/j.cpc.2019.107087.
(106) Cheng, L.; Ma, T. Y.; Zhang, X. Z.; Peng, Q. Y.; Liu, Y. Q.; Qi, J. Y. Maximum likelihood activity and attenuation estimation using both emission and transmission data with application to utilization of Lu-176 background radiation in TOF PET. *Medical Physics* **2020**, *47* (3), 1067-1082. DOI: 10.1002/mp.13989.
(107) Segars, W. P.; Sturgeon, G.; Mendonca, S.; Grimes, J.; Tsui, B. M. W. 4D XCAT phantom for multimodality imaging research. *Medical Physics* **2010**, *37* (9), 4902-4915. DOI: 10.1118/1.3480985.
(108) Vauclin, S.; Michel, C.; Buvat, I.; Doyeux, K.; Edet-Sanson, A.; Vera, P.; Gardin, I.; Hapdey, S. Monte-Carlo simulations of clinically realistic respiratory gated ¹⁸F-FDG PET: Application to lesion detectability and volume measurements. *Computer Methods and Programs in Biomedicine* **2015**, *118* (1), 84-93. DOI: 10.1016/j.cmpb.2014.10.003.
(109) He, X.; Park, S. Model observers in medical imaging research. *Theranostics* **2013**, *3* (10), 774-786. DOI: 10.7150/thno.5138 From NLM.
(110) Zhang, L.; Cavaro-Menard, C.; Le Callet, P. An overview of model observers. *Irbm* **2014**, *35* (4), 214-224. DOI: 10.1016/j.irbm.2014.04.002.
(111) Eckstein, M. P.; Bartroff, J. L.; Abbey, C. K.; Whiting, J. S.; Bochud, F. O. Automated computer evaluation and optimization of image compression of x-ray coronary angiograms for signal known exactly detection tasks. *Optics Express* **2003**, *11* (5), 460-475.
(112) Gonzalez, M. Channelized hotelling observer optimization for medical image quality assessment in lesion detection tasks. **2011**.
(113) Gaitanis, A.; Kontaxakis, G.; Spyrou, G.; Panayiotakis, G.; Tzanakos, G. PET image reconstruction: A stopping rule for the MLEM algorithm based on properties of the updating coefficients. *Computerized Medical Imaging and Graphics* **2010**, *34* (2), 131-141. DOI: 10.1016/j.compmedimag.2009.07.006.
(114) Lieleg, O.; Ribbeck, K. Biological hydrogels as selective diffusion barriers. *Trends in Cell Biology* **2011**, *21* (9), 543-551. DOI: 10.1016/j.tcb.2011.06.002.

(115) Tomasetti, L.; Breunig, M. Preventing Obstructions of Nanosized Drug Delivery Systems by the Extracellular Matrix. *Advanced Healthcare Materials* **2018**, *7* (3). DOI: 10.1002/adhm.201700739.
(116) Burla, F.; Sentjabrskaja, T.; Pletikapic, G.; van Beugen, J.; Koenderink, G. H. Particle diffusion in extracellular hydrogels. *Soft Matter* **2020**, *16* (5), 1366-1376. DOI: 10.1039/c9sm01837a.
(117) Hassan, S. A. Artificial neural networks for the inverse design of nanoparticles with preferential nano-bio behaviors. *Journal of Chemical Physics* **2020**, *153* (5). DOI: 10.1063/5.0013990.
(118) Li, L.; Wang, K.; Sun, X. L.; Wang, K. Z.; Sun, Y. Y.; Zhang, G. F.; Shen, B. Z. Parameters of Dynamic Contrast-Enhanced MRI as Imaging Markers for Angiogenesis and Proliferation in Human Breast Cancer. *Medical Science Monitor* **2015**, *21*, 376-382.
(119) Pedregosa, F.; Varoquaux, G.; Gramfort, A.; Michel, V.; Thirion, B.; Grisel, O.; Blondel, M.; Prettenhofer, P.; Weiss, R.; Dubourg, V.; et al. Scikit-learn: Machine Learning in Python. *Journal of Machine Learning Research* **2011**, *12*, 2825-2830.
(120) Mart\'n~Abadi and Ashish~Agarwal and Paul~Barham and Eugene~Brevdo and Zhifeng~Chen and Craig~Citro and Greg, S. C. a. A. D. a. J. D. a. M. TensorFlow : Large-Scale Machine Learning on Heterogeneous Systems. 2015.
(121) Cortes, C.; Vapnik, V. Support-vector networks. **1995**, *20* (3), 273-297.
(122) Song, Y. Y.; Lu, Y. Decision tree methods: applications for classification and prediction. *Shanghai Arch Psychiatry* **2015**, *27* (2), 130-135. DOI: 10.11919/j.issn.1002-0829.215044 From NLM.
(123) Mitchell, M. J.; Billingsley, M. M.; Haley, R. M.; Wechsler, M. E.; Peppas, N. A.; Langer, R. Engineering precision nanoparticles for drug delivery. *Nature Reviews Drug Discovery* **2021**, *20* (2), 101-124. DOI: 10.1038/s41573-020-0090-8.
(124) Li, Z.; Xiao, C.; Yong, T. Y.; Li, Z. F.; Gan, L.; Yang, X. L. Influence of nanomedicine mechanical properties on tumor targeting delivery. *Chemical Society Reviews* **2020**, *49* (8), 2273-2290. DOI: 10.1039/c9cs00575g.
(125) Hui, Y.; Yi, X.; Hou, F.; Wibowo, D.; Zhang, F.; Zhao, D. Y.; Gao, H. J.; Zhao, C. X. Role of Nanoparticle Mechanical Properties in Cancer Drug Delivery. *Acs Nano* **2019**, *13* (7), 7410-7424. DOI: 10.1021/acsnano.9b03924.
(126) Zein, R.; Sharrouf, W.; Selting, K. Physical Properties of Nanoparticles That Result in Improved Cancer Targeting. *Journal of Oncology* **2020**, *2020*. DOI: 10.1155/2020/5194780.
(127) Gerlowski, L. E.; Jain, R. K. MICROVASCULAR PERMEABILITY OF NORMAL AND NEOPLASTIC TISSUES. *Microvascular Research* **1986**, *31* (3), 288-305. DOI: 10.1016/0026-2862(86)90018-x.
(128) Meijer, E. F. J.; Baish, J. W.; Padera, T. P.; Fukumura, D. Measuring Vascular Permeability In Vivo. *Tumor Microenvironment: Methods and Protocols* **2016**, *1458*, 71-85. DOI: 10.1007/978-1-4939-3801-8_6.
(129) Dreher, M. R.; Liu, W. G.; Michelich, C. R.; Dewhirst, M. W.; Yuan, F.; Chilkoti, A. Tumor vascular permeability, accumulation, and penetration of macromolecular drug carriers. *Jnci-Journal of the National Cancer Institute* **2006**, *98* (5), 335-344. DOI: 10.1093/jnci/djj070.
(130) Dellian, M.; Yuan, F.; Trubetskoy, V. S.; Torchilin, V. P.; Jain, R. K. Vascular permeability in a human tumour xenograft: molecular charge dependence. *British Journal of Cancer* **2000**, *82* (9), 1513-1518.
(131) Nugent, L. J.; Jain, R. K. Extravascular Diffusion in Normal and Neoplastic Tissues1. *Cancer Research* **1984**, *44* (1), 238-244. (acccessed 7/24/2023).
(132) Lieleg, O.; Baumgartel, R. M.; Bausch, A. R. Selective Filtering of Particles by the Extracellular Matrix: An Electrostatic Bandpass. *Biophysical Journal* **2009**, *97* (6), 1569-1577. DOI: 10.1016/j.bpj.2009.07.009.
(133) Gonzalez-Castillo, C.; Rubio, R.; Zenteno-Savin, T. Coronary flow-induced inotropism is modulated by binding of dextrans to the endothelial luminal surface. *American Journal of Physiology-Heart and Circulatory Physiology* **2003**, *284* (4), H1348-H1357. DOI: 10.1152/ajpheart.00323.2002.